AD A040011

NBS SPECIAL PUBLICATION 400-29

U.S. DEPARTMENT OF COMMERCE / National Bureau of Standards

Semiconductor Measurement Technology

DDC
MAY 31 1977
C

Progress Report

January 1 to June 30, 1976

DDC FILE COPY

NATIONAL BUREAU OF STANDARDS

The National Bureau of Standards[1] was established by an act of Congress March 3, 1901. The Bureau's overall goal is to strengthen and advance the Nation's science and technology and facilitate their effective application for public benefit. To this end, the Bureau conducts research and provides: (1) a basis for the Nation's physical measurement system, (2) scientific and technological services for industry and government, (3) a technical basis for equity in trade, and (4) technical services to promote public safety. The Bureau consists of the Institute for Basic Standards, the Institute for Materials Research, the Institute for Applied Technology, the Institute for Computer Sciences and Technology, the Office for Information Programs, and the Office of Experimental Technology Incentives Program.

THE INSTITUTE FOR BASIC STANDARDS provides the central basis within the United States of a complete and consistent system of physical measurement; coordinates that system with measurement systems of other nations; and furnishes essential services leading to accurate and uniform physical measurements throughout the Nation's scientific community, industry, and commerce. The Institute consists of the Office of Measurement Services, and the following center and divisions:

Applied Mathematics — Electricity — Mechanics — Heat — Optical Physics — Center for Radiation Research — Laboratory Astrophysics[2] — Cryogenics[2] — Electromagnetics[2] — Time and Frequency[3].

THE INSTITUTE FOR MATERIALS RESEARCH conducts materials research leading to improved methods of measurement, standards, and data on the properties of well-characterized materials needed by industry, commerce, educational institutions, and Government; provides advisory and research services to other Government agencies; and develops, produces, and distributes standard reference materials. The Institute consists of the Office of Standard Reference Materials, the Office of Air and Water Measurement, and the following divisions:

Analytical Chemistry — Polymers — Metallurgy — Inorganic Materials — Reactor Radiation — Physical Chemistry.

THE INSTITUTE FOR APPLIED TECHNOLOGY provides technical services developing and promoting the use of available technology; cooperates with public and private organizations in developing technological standards, codes, and test methods; and provides technical advice services, and information to Government agencies and the public. The Institute consists of the following divisions and centers:

Standards Application and Analysis — Electronic Technology — Center for Consumer Product Technology: Product Systems Analysis; Product Engineering — Center for Building Technology: Structures, Materials, and Safety; Building Environment; Technical Evaluation and Application — Center for Fire Research: Fire Science; Fire Safety Engineering.

THE INSTITUTE FOR COMPUTER SCIENCES AND TECHNOLOGY conducts research and provides technical services designed to aid Government agencies in improving cost effectiveness in the conduct of their programs through the selection, acquisition, and effective utilization of automatic data processing equipment: and serves as the principal focus wthin the executive branch for the development of Federal standards for automatic data processing equipment, techniques, and computer languages. The Institute consist of the following divisions:

Computer Services — Systems and Software — Computer Systems Engineering — Information Technology.

THE OFFICE OF EXPERIMENTAL TECHNOLOGY INCENTIVES PROGRAM seeks to affect public policy and process to facilitate technological change in the private sector by examining and experimenting with Government policies and practices in order to identify and remove Government-related barriers and to correct inherent market imperfections that impede the innovation process.

THE OFFICE FOR INFORMATION PROGRAMS promotes optimum dissemination and accessibility of scientific information generated within NBS; promotes the development of the National Standard Reference Data System and a system of information analysis centers dealing with the broader aspects of the National Measurement System; provides appropriate services to ensure that the NBS staff has optimum accessibility to the scientific information of the world. The Office consists of the following organizational units:

Office of Standard Reference Data — Office of Information Activities — Office of Technical Publications — Library — Office of International Standards — Office of International Relations.

---

[1] Headquarters and Laboratories at Gaithersburg, Maryland, unless otherwise noted; mailing address Washington, D.C. 20234.
[2] Located at Boulder, Colorado 80302.

Semiconductor Measurement Technology

Progress Report, January 1 to June 30, 1976

W. Murray Bullis, Editor

Electronic Technology Division
Institute for Applied Technology
National Bureau of Standards
Washington, D.C. 20234

Jointly supported by:
The National Bureau of Standards
The Navy Strategic Systems Projects Office
The Defense Nuclear Agency
The Defense Advanced Research Projects Agency
The Space and Missile Systems Organization, and
The Energy Research and Development Administration

DDC
RECEIVED
MAY 31 1977
C

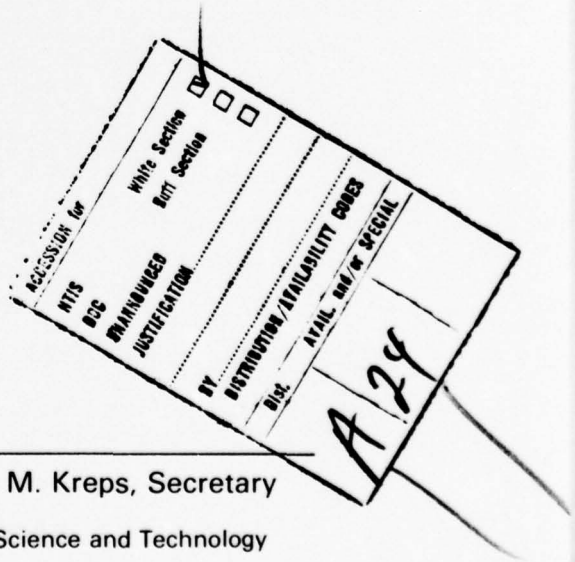

U.S. DEPARTMENT OF COMMERCE, Juanita M. Kreps, Secretary

Dr. Betsy Ancker-Johnson, Assistant Secretary for Science and Technology

NATIONAL BUREAU OF STANDARDS, Ernest Ambler, Acting Director

Issued April 1977

National Bureau of Standards Special Publication 400-29
Nat. Bur. Stand. (U.S.), Spec. Publ. 400-29, 119 pages (Apr. 1977)
CODEN: XNBSAV

U.S. GOVERNMENT PRINTING OFFICE
WASHINGTON: 1977

For sale by the Superintendent of Documents, U.S. Government Printing Office
Washington, D.C. 20402 - Price $1.85

Stock No. 003-003-01759-1

TABLE OF CONTENTS

SEMICONDUCTOR MEASUREMENT TECHNOLOGY

PAGE

List of Figures iv

List of Tables vii

Preface viii

Abstract and Key Words ix

1. Introduction 1

2. Highlights 2

3. Materials Characterization by Electrical Methods 7
3.1. Four-Probe Method 7
3.2. Spreading Resistance 9
3.3. Spreading Resistance Profiles 11
3.4. Photovoltaic Method 13
3.5. Reevaluation of Irvin's Curves 15
3.6. Electron Mobility in Phosphorus-Doped Silicon 17
3.7. Thermally Stimulated Current and Capacitance Measurements 19
3.8. Extended Range MIS C-V Method 26

4. Materials Characterization by Physical Analysis Methods 29
4.1. Optical Test for Surface Quality of Sapphire Substrates 29
4.2. Impurities in Sapphire Substrates 30
4.3. Electron Spectroscopy Techniques 31

5. Materials and Procedures for Wafer Processing 36
5.1. Sodium Contamination in Oxidation Furnaces 36
5.2. X-Ray Dose in Electron-Beam Evaporators 36
5.3. Ion Implantation Parameters 40
5.4. Passivation Integrity 42
5.5. Process Materials Characterization 47

6. Photolithography 48
6.1. Line-Width Measurement with Spatially Filtered Coherent Optical Radiation 48
6.2. Optical Imaging for Photomask Metrology 50
6.3. Calibration Standards for Photomask Metrology 53
6.4. Line-Width Measurements on Chromium-on-Glass Artifacts 53
6.5. Line-Width Measurement by Diffraction Pattern Analysis 57
6.6. Automated Photomask Inspection 58

7. Test Patterns 62
7.1. Square Array Collector Resistor 62
7.2. Sheet Resistor Test Structures 64
7.3. Test Pattern for TTL Technology 65
7.4. Test Pattern Design and Analysis for SOS/LSI 65

8. Assembly and Packaging 69
8.1. Nondestructive Test for Beam-Lead Bonds 69
8.2. In-Process Bond Monitor 72
8.3. Radioisotope Leak Test 74
8.4. Loose Particle Detection 75

9. Device Inspection and Test 77
9.1. Dual-Laser, Flying-Spot Scanner 77
9.2. Scanning Acoustic Microscopy 79

TABLE OF CONTENTS

PAGE

9.3. Scanning Electron Microscopy 84
9.4. Automated Scanning Low Energy Electron Probe 88
9.5. Thermal Properties of Transistors 88

10. References 90

Appendix A Semiconductor Technology Program Staff 96

Appendix B Semiconductor Technology Program Publications 97

Appendix C Workshop and Symposium Schedule 102

Appendix D Standards Committee Activities 103

Appendix E Solid-State Technology & Fabrication Services 105

Index 106

LIST OF FIGURES

PAGE

Frontispiece x

1. Photomicrographs of typical tungsten carbide probe tips 8

2. Ratio of spreading resistance, R_{sp}, to resistivity, ρ, as a function of resistivity as measured with a variety of probe tips on (111) *n*-type silicon surfaces mechanically polished with 0.5-μm alumina in aqueous slurry . . . 10

3. Ratio of spreading resistance, R_{sp}, to resistivity, ρ, as a function of resistivity as measured with relatively sharp osmium-tungsten alloy probe tips on (100) *n*-type silicon surfaces prepared in various ways 10

4. Dopant density profiles in boron-diffused *n*-type silicon as measured by the spreading resistance and incremental sheet resistance methods 12

5. Prototype automated data collection and analysis system for resistivity profiling of circular silicon slices by the scanning photovoltaic method 14

6. Conductivity mobility of electrons at 300 K as a function of total donor density for phosphorus-doped silicon 18

7. Resistivity as a function of temperature for seven phosphorus-doped silicon slices 18

8. Resistivity of phosphorus-doped silicon at 300 K as a function of total donor density 18

9. Thermally controlled chuck and automatic wafer prober 20

10. Thermally stimulated current response of gold-doped silicon MOS capacitors in wafer form 22

11. Thermally stimulated current response of gold-doped *n*-MOS capacitor with an oxide film contaminated by mobile ions 22

12. Capacitance-voltage characteristics of various oxides on *n*-type silicon with aluminum gate electrodes 24

13. Capacitance-voltage characteristics of four MOS capacitors on each of four *n*-type silicon wafers with dry thermal oxides, about 90 nm thick, and e-gun evaporated aluminum gates microalloyed at different temperatures 25

14. Temperature of peak value of thermally stimulated current response as a function of heating rate for selected defect centers in silicon 26

LIST OF FIGURES

PAGE

15. Specular reflection data for four bulk silicon substrates polished with different polishing grits and for six silicon-on-sapphire composites 29
16. Scanning electron micrographs of silicon-on-sapphire surfaces 30
17. Schematic of experimental conditions for ion sputter etching and Auger electron spectroscopy 32
18. Spatial distributions of ion beam current 32
19. Additional broadening of an interface at a depth of 100 nm due to flux inhomogeneity in rastered ion beams of normal and defective ion guns 33
20. Oxygen KLL profiles showing effects of electron-beam enhancement of sputtering rate 33
21. Geometry for crater-edge profiling using Auger electron spectroscopy 34
22. Line scans for oxygen, phosphorus, and elemental silicon across the interface between the points C and C^1 on the x-axis 35
23. Sodium density in the atmosphere of a fused silica oxidation tube as a function of water vapor content at temperatures from 1200 to 1400 K 37
24. Total ionizing dose deposited in the oxide layer as a function of electron-beam energy during the electron-gun evaporation of aluminum and chromium 38
25. Total ionizing dose deposited in the oxide layer as a function of the deposition rate of aluminum and chromium in an e-gun evaporation system 38
26. Total ionizing dose deposited in the oxide layer as a function of chromium layer thickness during the e-gun evaporation of chromium or of a 1-μm thick aluminum layer over chromium 38
27. Absorbance of x-ray energy in nylon film dosimeter as a function of the electron charge incident on aluminum in an e-gun evaporator 38
28. Typical target configuration for characterizing the ion beam before ion implantation 41
29. Scanning geometry and overscan efficiency 41
30. Target current densities as a function of scanner voltage for an 84-keV boron ion beam 41
31. Schematic representation of corona charging with positive ions 43
32. Schematic representation of the reverse decoration of defects with negative ions following corona charging with positive ions 44
33. Photomicrograph of reverse decorated device showing high contrast which renders microscopic evaluation fast and sensitive 45
34. Photomicrograph of portion of reverse decorated device aluminum-etched at 50°C for 5 min without removing carbon black 45
35. Schematic representation of microscope modified to obtain image of source field stop at the photocell to measure the integrated light reflected from defective areas 46
36. Sketch of the single-lens coherent optical system, showing the locations of various planes and coordinate systems 48
37. Calculated images of clear lines in opaque backgrounds for coherent illumination of wavelength 500 nm, and a 0.95 numerical aperture objective lens 49
38. Sketch of a possible configuration for a microscope system with spatial filtering 50
39. Diagram of optical research microscope as modified for line-width measurement . . . 51

LIST OF FIGURES

PAGE

40. Calculated and experimentally determined line-image profiles for clear lines in opaque backgrounds 52
41. Photomicrograph of chromium-on-glass artifact, viewed under bright-field transmitted light at a magnification of about 85x 53
42. Photomicrograph of four 1-μm wide clear spaces each separated by 1 μm in an iron-oxide-on-glass artifact viewed under bright-field transmitted light at a magnification of about 2000x 53
43. Schematic representation of optical system for diffraction pattern analysis 57
44. Schematic flow diagram for estimation of width of gaps 58
45. Arrangement of a square four-probe array on the diagonals of a thin, square specimen 63
46. Normalized sheet resistance error resulting from shorting contacts on the periphery of a square test structure 64
47. Normalized sheet resistance error resulting from shorting contacts at the ends of the arms of a Greek cross test structure 64
48. Junction-isolated TTL test pattern 66
49. Two-level interaction test structure 67
50. Two-level alignment structures 67
51. Distribution of *p*-channel saturation current in heavy inversion along the diameter of an SOS wafer perpendicular to the edge flat 68
52. Acoustic emission signals from single beams pulled to destruction 70
53. Beam-lead device with poor mechanical integrity 70
54. Apparatus for applying upward or downward force on beam-lead devices and for detecting any resulting acoustic emission 71
55. Acoustic emission signals from individual beams subjected to downward force on the horizontal portion of the beam 71
56. Beam-lead bonding tool modified to apply force to the beams without contacting the chip 72
57. Typical signatures of ultrasonic aluminum-aluminum wire bonds made with different power settings 74
58. Photoresponse of a typical 2N4431 UHF transistor to 0.633- and 1.15-μm radiation as a function of temperature 77
59. Temperature profile of hot spots in typical 2N4431 UHF transistors as measured with a laser scanner and an infrared microradiometer 78
60. Photograph of the reflected light plus photoresponse image obtained when the 0.633-μm laser beam scans the back side of a silicon-on-sapphire C-MOS 4007 inverter 78
61. Photograph of the reflected light image obtained when the 1.15-μm laser beam scans the back side of a flip-chip C-MOS 4007 inverter 78
62. Photographs of the reflected light plus photoresponse image obtained when the 1.15-μm laser beam scans the back side of a flip-chip 709 operational amplifier . . 78
63. Comparison of operating modes of the scanning acoustic microscope 80
64. Acoustic images showing differences between cw and pulsed operation 80
65. Comparison between 940-MHz acoustic images of a bipolar microwave transistor with 2-μm wide metal fingers and a photomicrograph taken with interference contrast 81

PAGE

66. Frequency dependence of attenuation of acoustic waves in water at various temperatures 82
67. Acoustic images, reflection mode at 940 MHz, of an integrated circuit showing the effect of non-normal incidence 82
68. Spherical tool grinder for making acoustic lenses 82
69. Photograph of the tool grinder 82
70. Frequency response of return and transmission loss of two sputtered glass acoustic anti-reflection coatings (AARC) 83
71. Change in threshold voltage, ΔV_{Th}, of a p-channel MOS transistor as the result of exposure to an electron flux of 5.2×10^{10} $cm^{-2} \cdot s^{-1}$ at energies of 17.5 and 30 keV in a scanning electron microscope 84
72. Electron-beam-induced-current response of a copper-doped silicon p-n diode 85
73. Electron-beam-induced-current response of a silicon npn transistor 86
74. Portion of a quad 2-input NAND gate including a functional gate on the left and a nonfunctional gate on the right 87
75. Portions of a low-power, four-bit shift register 87

LIST OF TABLES

PAGE

1. Results of Four-Probe Pilot Study on Thin Layers 7
2. Test Specimens for Four-Probe Matrix Experiment 8
3. Characteristics of Probes Used in Matrix Experiment 8
4. Preliminary Electron Mobility Data for Phosphorus-Doped Silicon at 300 K 16
5. Preliminary Hole Mobility Data for Boron-Doped Silicon at 300 K 16
6. Emission Coefficients and Activation Energies of Selected Defects in Silicon . . . 27
7. Elemental Content of Sapphire Substrates 31
8. Equilibrium Partial Pressures and Sodium Densities in Fused Silica Oxidation Tubes at 1300 K as a Function of Water Content in Flowing Oxygen 37
9. Equilibrium Partial Pressures and Sodium Densities in Tubes at 1300 K With an Atmosphere of 10% Hydrogen Chloride or Chlorine in an Inert Carrier Gas 37
10. Zinc Content in Glass Transferred from Doped Borosilicate Glass to Silicon at 1000°C 47
11. Apparent Widths of Lines and Spaces Measured in Bright-Field Transmitted Illumination 54
12. Effect of Focal Position on the Apparent Width of a Clear Space Measured with an Image-Shearing Eyepiece in Bright-Field Transmitted Illumination 54
13. Apparent Widths of Clear Lines in an Opaque Field 56
14. Representative Data for Line-Width Measurements Repeated on the Same Line 56
15. Characteristics of Automated Photomask Inspection Techniques 59
16. Correction Factors for a Square Four-Probe Array on a Thin Square Specimen 63
17. Pull Test Results for Monitored Ultrasonic Wire Bonds 73
18. Representative Response Frequencies of Metal Spheres Impacting a Steel Surface 76

PREFACE

The Semiconductor Technology Program serves to focus NBS efforts to enhance the performance, interchangeability, and reliability of discrete semiconductor devices and integrated circuits through improvements in measurement technology for use in specifying materials and devices in national and international commerce and for use by industry in controlling device fabrication processes. Its major thrusts are the development of carefully evaluated and well documented test procedures and associated technology and the dissemination of such information to the electronics community. Application of the output by industry will contribute to higher yields, lower cost, and higher reliability of semiconductor devices. The output provides a common basis for the purchase specifications of government agencies which will lead to greater economy in government procurement. In addition, improved measurement technology will provide a basis for controlled improvements in fabrication processes and in essential device characteristics.

The Program receives direct financial support principally from two major sponsors: the Defense Advanced Research Projects Agency (ARPA)* and the National Bureau of Standards (NBS).† In addition, the Program receives support from the Defense Nuclear Agency (DNA),§ the Air Force Space and Missiles Systems Organization,¶ the Navy Strategic Systems Project Office,# and the Energy Research and Development Administration.× The ARPA-supported portion of the Program, Advancement of Reliability, Processing, and Automation for Integrated Circuits with the National Bureau of Standards (ARPA/IC/NBS), addresses critical Defense Department problems in the yield, reliability, and availability of digital monolithic integrated circuits. Other portions of the Program emphasize aspects of the work which relate to the specific needs of the supporting agency. Measurement oriented activity appropriate to the mission of NBS is an essential aspect in all parts of the Program.

Essential assistance to the Program is also received from the semiconductor industry through cooperative experiments and technical exchanges. NBS interacts with industrial users and suppliers of semiconductor devices through participation in standardizing organizations; through direct consultations with device and material suppliers, government agencies, and other users; and through periodically scheduled symposia and workshops. In addition, progress reports, such as this one, are regularly prepared for issuance in the NBS Special Publication 400 sub-series. More detailed reports such as state-of-the-art reviews, literature compilations, and summaries of technical efforts conducted within the Program are issued as these activities are completed. Reports of this type which are published by NBS also appear in the Special Publication 400- sub-series. Announcements of availability of all publications in this subseries are sent by the Government Printing Office to those who have requested this service. A request form for this purpose may be found at the end of this report.

Another means of interaction with the electronics community is by direct contact. In particular, comments from readers regarding the usefulness of the results reported herein or relating to directions of future activity in the Program are always welcome.

Disclaimer

Certain commercially available materials or instruments are identified in this publication for the purpose of providing a complete description of the work performed. The experiments reported do not constitute a complete evaluation of the performance characteristics of the products so identified. In no case does such identification imply recommendation or endorsement by the National Bureau of Standards nor does it imply that the items identified are necessarily the best available for the purpose.

---

* Through ARPA Order 2397, Program Code 6D10 (NBS Cost Center 4257555). All contract work was funded from this source.

† Principally through the Electronic Technology Program (Cost Center 4257100). Additional funding through the Dimensional Metrology Program (Cost Center 2131119) and the Nondestructive Evaluation Program (Cost Center 4253130).

§ Through Inter-Agency Cost Reimbursement Order 76-806 (NBS Cost Center 4259522).

¶ Through MIPR FY76 167600366 (NBS Cost Center 4259560).

Code SP-23, through project order N0016475P070030 administered by Naval Weapons Support Center, Crane, Indiana (NBS Cost Center 4251533).

× Division of Electric Energy Systems, through ERDA Contract No. E(49-1)-3300, Modification 3 (NBS Cost Center 4259561).

ABSTRACT

This progress report describes NBS activities directed toward the development of methods of measurement for semiconductor materials, process control, and devices. Both in-house and contract efforts are included. The emphasis is on silicon device technologies. Principal accomplishments during this reporting period included (1) development of theoretical expressions for electron mobility in silicon based on combinations of scattering mechanisms; (2) successful low-temperature processing of MOS capacitors to permit measurement of thermally stimulated current and capacitance without subjecting the specimens to potentially degrading heat treatments; (3) completion of a study of the thermodynamics of reactions in an oxidation furnace tube which provides a basis for models of the effect of water vapor, chlorine, and tube wall conditions on sodium contamination levels; (4) development of a rapid, nondestructive method for reverse decoration of defects in passivation overcoats; (5) development of the theoretical basis for accurate measurement of small line widths by analysis of a spatially filtered image of the line; (6) extension of the acoustic emission technique to the nondestructive testing of tape-bonded chips and hybrid components; and (7) analysis of the results of a first exploratory interlaboratory evaluation of the radioisotope method for testing hermeticity of semiconductor devices. New tasks were undertaken to develop techniques for measuring resistivity uniformity of and non-dopant impurities and defects in power-device grade silicon and to investigate the particle impact noise detection method for screening devices for the presence of loose particles in the package; initial results were obtained in the study of scanning acoustic microscopy which was begun during the previous reporting period. Because of technical limitations in the methods, efforts to develop both the automated scanning low energy electron probe and in-process ultrasonic bond monitor were terminated. Also reported is other ongoing work on materials characterization by electrical and physical analysis methods, materials and procedures for wafer processing, photolithography, test patterns, and device inspection and test procedures. Supplementary data concerning staff, publications, workshops and symposia, standards committee activities, and technical services are also included as appendices.

KEY WORDS

Acoustic emission; Auger electron spectroscopy; beam-lead bonds; capacitance-voltage methods; carrier mobility; C-MOS circuits; dopant profiles; electrical properties; electronics; four-probe method; hermeticity; ion implantation; Irvin's curves; leak tests; line-width measurement; measurement methods; microelectronics; optical flying-spot scanner; oxidation particle impact noise detection test; passivation overcoats; photovoltaic method; power-device grade silicon; radioisotope method; resistivity; resistivity variations; safe operating area, transistor; scanning acoustic microscope; scanning electron microscope; scanning low energy electron probe; semiconductor devices; semiconductor materials; semiconductor process control; silicon; silicon dioxide; silicon on sapphire; sodium contamination; spreading resistance; surface roughness; test patterns; thermally stimulated current; transistors, power; TTL circuits; ultrasonic wire bonding; ultraviolet reflectance; x-ray damage.

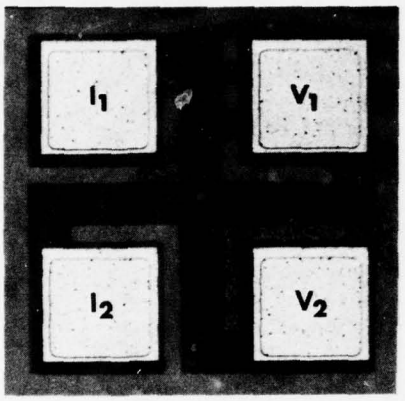

a. Greek cross.

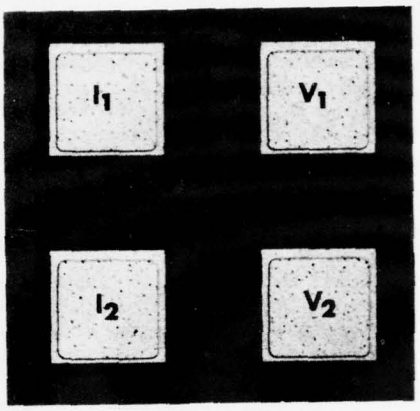

b. Greek cross with minimum line width.

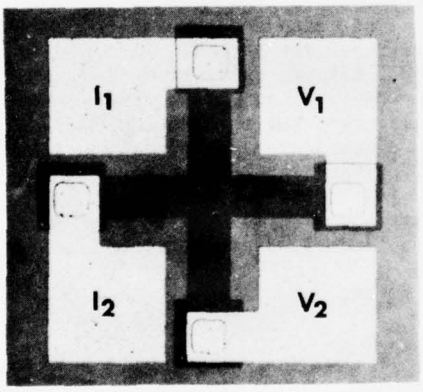

c. Greek cross with small contact windows.

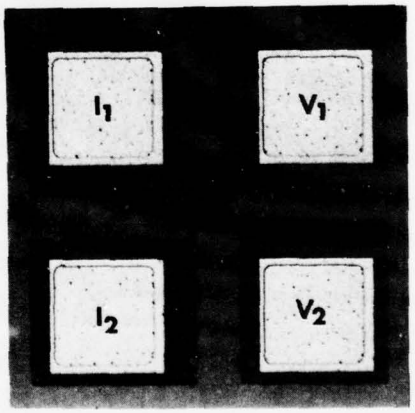

d. Offset quadrate cross.

Frontispiece — Cross-type base sheet resistor test structures (see sec. 7.2.).

SEMICONDUCTOR MEASUREMENT TECHNOLOGY

PROGRESS REPORT
January 1 to June 30, 1976

1. INTRODUCTION

This is a report to the sponsors of the Semiconductor Technology Program on work during the thirty-first and thirty-second quarters of the Program. It summarizes work on a wide variety of measurement methods for semiconductor materials, process control, and devices that are being studied at the National Bureau of Standards. The Program, which emphasizes silicon-based device technologies, is a continuing one, and the results and conclusions reported here are subject to modification and refinement.

The work of the Program is divided into a number of tasks, each directed toward the study of a particular material or device property or measurement technique. This report is subdivided according to these tasks. Highlights of activity during the reporting period are given in section 2. This section provides a management-level overview of the entire effort. Subsequent sections deal with each specific task area. References cited are listed in the final section of the report.

The report of each task includes a narrative description of progress made during this reporting period. Additional information concerning the material reported may be obtained directly from individual staff members identified with the task in the report. Organizational locations and telephone numbers for Program staff members are given in Appendix A.

Background material on the Program and individual tasks may be found in earlier progress reports as listed in Appendix B. From time to time, publications are prepared that describe some aspect of the program in greater detail. Current publications of this type are also listed in Appendix B. Reprints or copies of such publications are usually available on request to the author. In addition tutorial videotapes are being prepared on selected measurement topics for dissemination to the electronics community. Currently available videotapes and procedures for obtaining them on loan are also listed in Appendix B.

Communication with the electronics community is a critical aspect both as input for guidance in planning future program activities and in disseminating the results of the work to potential users. Formal channels for such communication occur in the form of workshops and symposia sponsored or co-sponsored by NBS. At the present time, no such seminars and workshops are scheduled. However, the availability of proceedings from past workshops and seminars is indicated in Appendix C.

An important part of the work that frequently goes beyond the task structure is participation in the activities of various technical standardizing committees. The list of personnel involved with this work given in Appendix D suggests the extent of this participation. In most cases, details of standardization efforts are reported in connection with the work of a particular task.

Technical services in areas of competence are provided to other NBS activities and other government agencies as they are requested. Usually these are short-term, specialized services that cannot be obtained through normal commercial channels. To indicate the kinds of technology available to the Program, such services provided during the current reporting period are listed in Appendix E.

2. HIGHLIGHTS

Highlights of progress in the various technical task areas of the Program are listed in this section. Particularly significant accomplishments during this reporting period included:

(1) development of theoretical expressions for electron mobility in silicon based on combinations of scattering mechanisms;

(2) successful low-temperature processing of MOS capacitors to permit measurement of thermally stimulated current and capacitance without subjecting the specimens to potentially degrading heat treatments;

(3) completion of a study of the thermodynamics of reactions in an oxidation furnace tube which provides a basis for models of the effect of water vapor, chlorine, and tube wall conditions on sodium contamination levels;

(4) development of a rapid, nondestructive method for reverse decoration of defects in passivation overcoats;

(5) development of the theoretical basis for accurate measurement of small line widths by analysis of a spatially filtered image of the line;

(6) extension of the acoustic emission technique to the nondestructive testing of tape-bonded chips and hybrid components; and

(7) analysis of the results of a first exploratory interlaboratory evaluation of the radioisotope method for testing hermeticity of semiconductor devices.

New tasks were undertaken to develop techniques for measuring resistivity uniformity of and non-dopant impurities and defects in power-device grade silicon and to investigate the particle impact noise detection method for screening devices for the presence of loose particles in the package; initial results were obtained in the study of scanning acoustic microscopy which was begun during the previous reporting period. Because of technical limitations in the methods, efforts to develop both the automated scanning low energy electron probe and in-process ultrasonic bond monitor were terminated.

Unless another organization is identified, the work described in the following paragraphs was performed at the National Bureau of Standards.

Materials Characterization by Electrical Methods — An extensive matrix experiment was carried out to examine the conditions under which the sheet resistance of very thin junction-isolated silicon layers could be measured reliably by the four-probe method. In contrast to the less promising results of an interlaboratory pilot study, conducted in cooperation with ASTM Committee F-1 on Electronics, the results of these experiments showed that better than 1 percent repeatability is feasible if measurement conditions are properly controlled. An interlaboratory test to verify this conclusion is now being conducted in cooperation with Committee F-1.

Experiments to determine the effects of specimen surface preparation and probe material on the empirical relation between silicon resistivity and spreading resistance were continued with the study of surfaces mechanically polished with 0.3-μm alumina in an aqueous slurry. Anomalous results were obtained on (111) *n*-type surfaces; satisfactory results were obtained on (111) *p*-type and (100) *n*-type surfaces.

As a preliminary test of the application of a simplified calculational procedure being developed at Solecon Laboratories for correcting spreading resistance data on layers with nonuniform resistivity, the dopant profiles of two boron-diffused layers were measured by the spreading resistance method and by the incremental sheet resistance method and compared. The relatively close agreement obtained suggests that the parallel superposition approach is quite accurate for diffused structures with junction depths less than 2 μm. Discrepancies near the surface could be accounted for on the basis of bevel-rounding effects.

Work on the bulk photovoltaic effect was resumed with emphasis on the application of this method to evaluation of resistivity variations along the diameter of circular slices suitable for fabrication of high-power thyristors and rectifier diodes. An automated data collection and analysis system for making photovoltaic measurements has been designed and assembled. Subsequently, the resolution of this technique is to be compared with that of the spreading resistance method.

As part of the continuing experimental redetermination of the resistivity-dopant density relation (Irvin's curves), additional measurements of room-temperature resistivity and dopant density were made on silicon wafers doped with phosphorus. In addition, initial measurements were made on silicon wafers

doped with boron. In general the electron mobilities lie above those based on Irvin's data and the hole mobilities lie below those reported by Wagner.

Theoretical expressions have been developed for the electron mobility in silicon as a function of temperature and dopant density. By incorporating the effects of electron-electron scattering and scattering anisotropies in the mobility calculation, good agreement between theory and experiment for both electron mobility and resistivity was obtained for phosphorus-doped silicon slices with dopant density of 10^{14} to 3×10^{18} cm^{-3} over the temperature range 100 to 500 K.

A new task has been undertaken to examine the range of validity of the Schottky equations (based on the depletion approximation) which are commonly used to extract dopant density from capacitance-voltage data. Numerical solutions to boundary value problems based on the carrier transport equations or Poisson's equation are being developed to provide a basis for comparison. Among the questions to be studied explicitly are: (1) what is the correct definition of junction capacitance in terms of field quantities such as electric field and electron and hole densities? and (2) is the quantity derived from capacitance-voltage data by the Schottky equation the equilibrium free-carrier density or the impurity (dopant) density in the depletion region?

A new task has been initiated to study the thermally stimulated current and capacitance response of silicon suitable for fabrication of high-power thyristors and rectifier diodes. Initial work has concentrated on the development of apparatus for making the measurements at the wafer level and evaluation of low-temperature procedures for fabrication of MOS capacitors. Early results suggest that capacitors fabricated with a silicon dioxide layer chemically vapor deposited at 400°C and an electron-beam (e-gun) evaporated aluminum gate, microalloyed in dry nitrogen at 400°C, are suitable for thermally stimulated current and capacitance measurements. It was also demonstrated that such measurements can be made at the wafer level in a dry nitrogen atmosphere; an improved apparatus for this purpose was designed and assembled. The results of preliminary experiments suggest that it may be possible to make thermally stimulated current and capacitance measurements even in capacitors with oxides contaminated by relatively large densities of mobile ions provided that the mobile ions are driven to the metal-oxide interface. In related work, the emission temperatures of a number of impurity and defect centers in silicon were calculated as a function of heating rate with the use of data compiled from literature.

Design and evaluation work on the modified instrument for measuring capacitance at applied voltages of up to 10 kV has been completed at RCA Laboratories. In an application of this instrument, it was shown that a large positive charge develops at the silicon-sapphire interface during e-gun metallization and that annealing at 400°C in forming gas does not entirely remove this charge. The extended-range measurement technique was refined to permit measurement of conductance as a function of voltage in addition to capacitance.

Materials Characterization by Physical Analysis Methods — Development of calibration standards for ion microprobe mass analysis continued at Texas Instruments with emphasis on improved masking techniques for fabricating the microvolume structures, preparation of implanted specimens, and collection of data. Preliminary results suggest that the smaller microvolume structures may be inappropriate for calibration artifacts. Consequently, future activities in this task are being directed toward collection of reproducibility data and refinement of procedures for calibrating standard specimens.

The rapid, nondestructive reflectance technique being developed at RCA Laboratories to determine the surface quality of sapphire substrates was extended to ultraviolet wavelengths. The reflectance characteristics of silicon-on-sapphire composites could be correlated with the surface roughness of the silicon film.

The impurity content of three sapphire substrates was determined by neutron activation analysis. These measurements were made to assist an Air Force contractor in studying the influence of impurities transferred from the sapphire substrate to the silicon film on the properties of silicon-on-sapphire devices.

A study was made of the effect of ion flux distribution in Auger/ion beam profiling of oxide-silicon structures at Stanford University. It was shown that ion flux inhomogeneities can be a limiting factor in depth resolution. Apparent interface broadening was also shown to occur in the presence of enhanced sputtering as a result of electron-stimulated desorption of oxygen from the oxide. In related work at Varian Associates, the crater edge formed by ion beam etching

was shown to provide a bevelled surface which allows depth profiling by Auger electron spectroscopy with a spatial resolution significantly greater than that obtainable on a mechanically lapped bevelled surface.

Materials and Procedures for Wafer Processing — A thermodynamic study of the reactions in a fused silica oxidation furnace tube was completed. Equilibrium sodium concentrations in the furnace atmosphere were determined at several temperatures for varying amounts of water vapor and chlorine; it was assumed that the sodium was transferred from the tube wall in which it occurs at a level of about 10 parts per million by weight. The presence of water vapor was shown to increase the sodium density significantly because of the formation of sodium hydroxide. The results of the calculations also provide insight into the mechanisms which occur when cleaning furnace tube walls with hydrogen chloride or chlorine.

Additional calculations were made to estimate the x-ray dose received by oxide films in MOS structures from the deposition of aluminum or chlorine gate electrodes by electron-beam evaporation. It was found that the dose received is essentially independent of the electron beam energy. A significant reduction in dose absorbed in the oxide occurs if a chromium film is used as the gate electrode rather than an aluminum film, primarily because the power necessary to deposit a chromium layer is significantly less than that required to deposit the same thickness of aluminum.

Dose measurement studies were completed as part of the development of measurement technology for critical ion implantation parameters at Hughes Research Laboratories. Evaluation of a group of typical current integrators revealed inaccuracies at high implantation currents, a situation which may cause problems as the industry moves to higher currents for production use. Procedures for measuring the ion beam current density distribution were also developed. In addition several metallization systems were evaluated for use as Schottky barrier contacts on n-type silicon; gold yielded the best results in this study.

A new, simple, nondestructive reverse decoration technique was developed at RCA Laboratories to detect defects in insulating films over metal portions of semiconductor devices. The defects are clearly visible for microscopic examination because the decorating medium, carbon black, covers only portions of the surface on which defects are absent. The decorating medium can be completely removed following examination.

Studies of the transfer of zinc from simulated boron nitride diffusion sources to the glass which forms on the surface of a silicon wafer during a typical diffusion process were carried out at the Pennsylvania State University. The results of these experiments were inconclusive because available measurement techniques proved to be too insensitive. In addition, calculations were made of equilibrium partial pressures of the chemical species in both hydrogen chloride and trichloroethylene oxidation systems. It was found that the partial pressure of water vapor in the trichloroethylene system was about an order of magnitude lower than that in the hydrogen chloride system.

Photolithography — Application of the spatial filtering technique to line-width measurement with an optical microscope was analyzed. In this method, the observer uses an optical transformation of the line in which the image no longer resembles the original line but in which the location of the line edges is marked by two narrow, dark lines within a bright surround. Although implementation of this technique will require redesign of microscope objectives with large numerical apertures so that the plane of the object spectrum occurs outside the physical dimensions of the lens system, this technique appears in principle to alleviate many of the problems associated with the use of filar and image-shearing eyepieces.

A research microscope was modified to make photometric scans of line-image profiles for comparison with theoretically computed profiles. The agreement obtained between measured and calculated profiles for transparent lines as narrow as 1 μm in an opaque background was quite satisfactory; the results to date suggest that the system can be used to measure the width of transparent lines nearly as narrow as the impulse response of the objective lens, and thus that it may be possible to calibrate line-width artifacts as narrow as 0.5 μm without resorting to scanning electron microscopy. Work is underway to investigate causes for the remaining discrepancies between theory and experiment.

Chromium-on-glass artifacts with opaque and transparent lines as small as 1 μm wide have been fabricated successfully. Additional measurements of line widths on such artifacts confirmed the previously predicted discrepan-

cies between measurements made with filar and image-shearing eyepieces.

A study was undertaken at Recognition Systems to delineate the tolerances, design criteria, and limitations associated with the measurement of line widths by analysis of the diffraction pattern. It was shown that the system response depends on the uniformity and phase of the aperture illumination and on the numerical aperture and quality of the objective lens as well as on the characteristics of the line or gap being measured. The results suggest that additional analysis and instrumental improvements will be necessary to interpret accurately widths of lines less than 2.5 μm wide; such modifications are being considered.

Detailed analyses were completed of a variety of automated technologies applicable to the inspection of photomasks for defects. It was concluded from this work, conducted at Lawrence Livermore Laboratory, that the search for dimensional errors and the search for defects differs significantly, and that these functions should be performed independently. Speed is the most important consideration in the automated search for visible defects; the analyses showed that few systems as presently envisioned have economically attractive inspection times. To provide a means for future evaluation of various automated mask inspection systems, work was initiated on the design and fabrication of a test mask with intentionally added defects.

Test Patterns — The square array four-probe collector resistor structure was further analyzed for the case in which the probe spacing is comparable with the lateral dimensions of a square specimen. It was found that simple, limiting expressions for the specimen resistivity provide 1 percent or better accuracy except for ratios of the length of the specimen side to the probe spacing between 1.35 and 23.

Additional analysis of cross-type sheet resistor test structures was completed. The Greek cross structure, which can be treated as a simple van der Pauw resistor, is particularly interesting because it affords the possibility of measuring sheet resistance in a region whose dimensions are limited only by the minimum line width achievable by the photolithographic technology utilized in device fabrication.

A test pattern for TTL technology is being developed as an illustration of a microelectronic test pattern for use in implementing the process validation wafer concept. The pattern consists of a variety of modularized test structures which are intended to be tested electrically with a high-speed dc wafer tester. Included are test structures which can identify variations in process and circuit parameters and the presence of random faults.

The mask set for the SOS/LSI test pattern being developed at RCA Laboratories was completed and two lots of wafers were processed. Preliminary results were obtained on several test structures designed for visual examination and on the distribution of the characteristics of the *p*-channel transistor across a wafer.

Assembly and Packaging — Detailed experiments were carried out to evaluate the acoustic emission test as a nondestructive means for evaluating the quality of beam-lead bonds. Distinct differences were obtained in the emission signals for various types of bond weaknesses. In addition it was shown that this technique could also be applied to evaluation of other types of gang-bonded devices.

An extensive series of experiments was carried out to complete the evaluation of the in-process ultrasonic bond monitor. These experiments showed that the characteristic signal observed at the node of the bonding tool did not correlate with bond quality but occurred as a result of transients in the power supply-transducer-tool system. Because of the negative results of these experiments, further development of this technique has been abandoned.

The first exploratory interlaboratory evaluation of the radioisotope method for testing hermeticity of semiconductor devices has been completed and the results analyzed. This experiment demonstrated conclusively that an interlaboratory comparison of hermetic packages can be accomplished under appropriate metrological guidelines. The ten measurements on each of 100 test packages yielded leak rates which agreed to within a fraction of the decade in which the mean value occurred, in contrast to order of magnitude differences observed in earlier, less formal industrial comparisons. In addition the experiment provided information necessary to develop an improved measurement procedure.

Detailed evaluation of the particle impact noise detection test has been initiated as a first phase of a study of loose particle de-

tection methods. Initial results showed the feasibility of using seeded cans as reference standards for evaluation of equipment for this test and demonstrated the equivalence of three commonly used couplants used to attach the device to the test apparatus.

Device Inspection and Test — Procedures were developed to obtain a quantitative measure of localized temperatures within operating bipolar silicon devices using the dual-laser, flying-spot scanner. The feasibility of using the laser scanner to observe a device through the back side was demonstrated; this has implications for examining face-mounted chips which cannot be inspected in the usual fashion. A color display was added to the scanner in order to assist in separating various responses and, with suitable mixing, to display contours of equal photoresponse.

Detailed studies of scanning acoustic microscopy as a technique for the inspection of semiconductor devices and integrated circuits continued at Stanford University and Hughes Research Laboratories. At Stanford, a 940-MHz microscope has been constructed which appears to have a resolution of about 0.5 μm. The feasibility of observing temperature differences with the microscope was demonstrated by means of a brief investigation, and initial work was undertaken to evaluate the use of an acoustic beam with non-normal incidence in reflection-type imaging. Hughes has constructed a second-generation microscope which operates at 400 MHz. This microscope has demonstrated good day-to-day mechanical and electrical stability, and appears to have a resolution of better than 2.5 μm. In addition an acoustic anti-reflection coating was developed to reduce signal losses at the lens-water interface by up to 18 dB.

Experiments and analyses were conducted to demonstrate the relevance of total dose as the key parameter in device degradation as a result of inspection with a scanning electron microscope. It was shown that if the device is expected to function electrically after such examination, it is essential to develop a careful analysis strategy before the device is placed in the specimen chamber of the scanning electron microscope. Some of the limitations of a simple method of calculation for estimating the magnitude of electron-beam-induced currents in device structures were demonstrated by measurements on a diode doped with copper and on an *npn* transistor. In addition the usefulness of electron-beam-induced-current images in the comparative mode was demonstrated.

The automated scanning low energy electron probe being developed at the Naval Research Laboratory was used to view a typical integrated circuit structure. These observations were impaired by surface charging effects which degraded resolution below acceptable levels. Significant instrument alterations will have to be made to remove this obstacle to routine examination of integrated circuit chips. No further work is planned.

A model for the formation of stable hot spots in transistors was developed in cooperation with Westinghouse Research Laboratories. The model explains the thermal hysteresis effects of transistor current gain as a function of collector voltage which had been observed previously and provides a sounder basis for the determination of safe operating conditions for power transistors.

3. MATERIALS CHARACTERIZATION BY ELECTRICAL METHODS

3.1. Four-Probe Method

An extensive matrix experiment was carried out to examine the conditions under which the sheet resistance of very thin junction-isolated silicon layers (0.2 to 1.5 μm thick) could be measured reliably by the four-probe method. The experiment was undertaken because of the wide variations in sheet resistance values reported in a pilot study conducted under the auspices of ASTM Committee F-1 on Electronics.

In the pilot study, sets of four wafers were measured by NBS and by another of the six other participating laboratories. Each set contained one diffused, one polysilicon, and two implanted specimens selected from those listed in table 1. All layers were prepared on opposite type substrates and had sheet resistance, R_s, in the range 4 to 1100 Ω/□ and thickness in the range 0.2 to 2 μm. Each laboratory used, and reported, the test conditions it considered to be best suited for the measurements. Current levels chosen were generally based on those specified for measurements on thicker epitaxial layers [1], and a wide variety of probe tip radii and loads were utilized. These ranged from 4-mil (0.1-mm) radius tips loaded with 50 to 175 g to 1.6-mil (0.04-mm) radius tips loaded with 50 gf (0.49N). The degree of reproducibility can be estimated roughly from the pooled relative sample standard deviations listed in the last two columns of table 1. Each specimen was measured twice, once by NBS and once by another laboratory. In some cases the several specimens of a given type were similar enough that they could be characterized by a single mean and standard deviation; in these cases the relative sample standard deviation, s, listed in column A, was found from the usual formula

$$s = \frac{100}{\bar{x}} \left\{ \frac{1}{(2n-1)} \sum_{i=1}^{2n} (x_i - \bar{x})^2 \right\}^{1/2},$$

where 2n is the number of measurements, x_i is the ith measured value of sheet resistance, and $\bar{x}$ is the average sheet resistance. In other cases the specimens could not be characterized by a single mean and standard deviation; in these cases s, listed in column B, was found from

$$s = \left\{ \frac{1}{n} \sum_{j=1}^{n} s_j^2 \right\}^{1/2},$$

where n is the number of specimens and s_j is the relative sample standard deviation associated with a pair of measurements on the jth specimen. Since the various specimens were

Table 1 — Results of Four-Probe Pilot Study on Thin Layers

Specimen Type	Nominal Layer Thickness, μm	Nominal Sheet Resistance, Ω/□	Number of Specimens	Pooled Relative Sample Standard Deviation, %	
				A	B
n-type polysilicon	0.3	1000	3	—	1.4
p-type polysilicon	0.3	250	3	—	0.9
n-type diffusion	2.0	4	3	2.5	1.9
p-type diffusion	1.0	300	3	3.6	3.6
p-type implant	0.2	250	2	2.0	2.0
p-type implant	1.5	750	2	32	39
p-type implant	0.2	1000	2	11	11.5
n-type implant	0.2	350	2	53	73
n-type implant	1.5	600	2	—	2.0
n-type implant	0.2	1100	2	—	7.3

Table 2 — Test Specimens for Four-Probe Matrix Experiment

Specimen	Layer Type	Dopant	Nominal Thickness, μm	Nominal Sheet Resistance, Ω/□
1	Diffusion	Boron	1	270
2	Epitaxy	Arsenic	1.5	3600
3	Epitaxy	Boron	1.5	3100
4	Implant	Boron	1.5	850
5	Implant	Boron	0.2	1150
6	Implant	Phosphorus	0.2	350
7	Implant	Phosphorus	0.2	1250

Table 3 — Characteristics of Probes Used in Matrix Experiment

Probe	Probe Material	Probe Tip Shape	Probe Radius, in. (mm)	Probe Loads Used, gf (N)
A	Tungsten Carbide	Round	0.002 (0.05)	15,30,45 (0.15,0.29,0.44)
B	Tungsten Carbide	Round	0.004 (0.10)	30,60,90,150 (0.29,0.59, 0.88,1.47)
C	Tungsten Carbide	Flat	0.001 (0.02)	30 (0.29)
D	Tungsten Carbide	Flat	0.002 (0.05)	30 (0.29)
E	Tungsten Carbide	Flat	0.0035 (0.09)	30 (0.29)
F	Tungsten Carbide	Flat	0.05 (1.3)	30 (0.29)
G	Osmium	Round	0.002 (0.05)	18,30,45 (0.18,0.29,0.44)
H	Osmium (current) Tungsten Carbide (voltage)	Round Round	0.004 (0.10) 0.004 (0.10)	30,60,90 (0.29,0.59,0.88)
I	Osmium (current) Tungsten Carbide (Voltage)	Round Round	0.002 (0.05) 0.004 (0.10)	30,90 (0.29,0.88)
J	Osmium (voltage) Tungsten Carbide (current)	Round Round	0.002 (0.05) 0.004 (0.10)	30,90 (0.29,0.88)

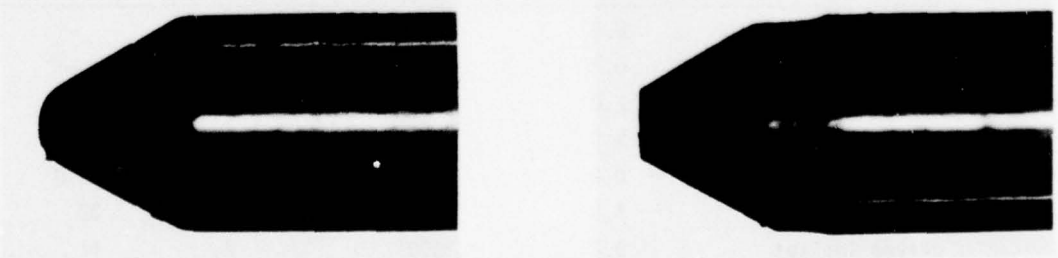

a. As supplied, 4-mil (100-μm) radius of sphere; magnification: ∿75x.

b. Lapped flat, 2.6-mil (65-μm) radius of circle; magnification: ∿75x.

Figure 1. Photomicrographs of typical tungsten carbide probe tips.

not exposed to the same set of probe conditions, it is not possible to draw firm conclusions regarding the relative sensitivity of wafer types to various measurement conditions.

For the matrix experiment, a set of specimens representative of various layer characteristics — method of fabrication, thickness, and sheet resistance — was selected from available stock; the properties of the specimens used are listed in table 2. In each case the substrates were of opposite type with room-temperature resistivity in the range 0.5 to 5 Ω·cm. Because the initial screening showed that the several available wafers of any one layer type, thickness, and sheet resistance combination were not in general good enough replicates (2 percent or less variation in sheet resistance), it was decided to use only one wafer of each type to generate the comparison of the various measurement conditions.

The principal intent of the study was to identify as wide a range of measurement conditions as possible for which valid results could be obtained in order to make any resulting recommended procedures applicable to as wide a variety of commercial resistivity test sets as possible, as well as to identify a safe guard band to allow for degradation of equipment as commonly experienced in a production environment. A secondary purpose was to provide a basis for unifying, where possible, the several differing sets of conditions recommended for use in making sheet resistance and resistivity measurements by the four-probe method [1,2].

Table 3 lists the characteristics of the probes used in the study. Some probes were used exactly as bought, with a hemispherical tip at the end of the stylus as shown on the left in figure 1. For this case, the size given is the radius of the tip. Other probes started with a hemispherical tip, but were lapped flat prior to use as shown on the right in figure 1. For these probes the size given is the radius of the flatted probe tip. Blunted probes were included in the study because they were expected to minimize stress concentration in the silicon under the probe. Such stresses appear to be responsible for junction leakage to the substrate, particularly in thin epitaxial wafers. The risk entailed with blunted probes is that the contact resistance to the specimen may become undesirably large, due, for example, to stray dirt accumulating under a probe tip or to a surface oxide film. Such contamination appears, in general, to be less easily penetrated with a flatted than with a rounded probe tip. Except for the bottom three sets in the table, all four probes in a given set were identical. Probe loads used in the study are also listed in the table.

To establish a baseline, measurements were made for each measurement condition using a value of current which provided a voltage of 10 to 15 mV between the inner probes of the four-probe array; this is a somewhat more restrictive condition than that recommended in the standard method [1]. In general, measurements made at currents one-tenth of this nominal value yielded sheet resistance values which were the same as those made with the baseline current within the estimated measurement error of 1 percent. Except in a few cases, measurements made at currents five times this nominal value also yielded the same sheet resistance value.

To compare measurements made under various conditions, six measurements were made for each case using the nominal value of current. For each specimen, the correct sheet resistance value was taken as the highest stable reading. Excessive leakage to the substrate, which occurred when sharp points or large loads were used, caused the measured sheet resistance to be smaller than the correct value. Use of lightly loaded, blunt tips frequently resulted in erratic contacts which caused an increase in the variability of a six-measurement data set. Typically a good set of data had a relative sample standard deviation less than 1 percent.

The results of these experiments suggest that one should use hemispherical or flatted probes with a radius of at least 0.004 in. (0.1 mm) with a load in the range 30 to 80 gf (0.29 to 0.78 N). Although current levels to provide a voltage of 10 to 20 mV between the inner probes are preferred, the current levels specified in the standard method [1] are also satisfactory. An interlaboratory test to verify these conclusions is now being conducted in cooperation with Committee F-1.

(J. R. Ehrstein and D. R. Ricks)

3.2. Spreading Resistance

Experiments to determine the effect of specimen surface preparation and probe material on the empirical relation between silicon resistivity, ρ, and spreading resistance, R_{sp}, (NBS Spec. Publ. 400-25, pp. 8-12) were continued with the study of surfaces mechani-

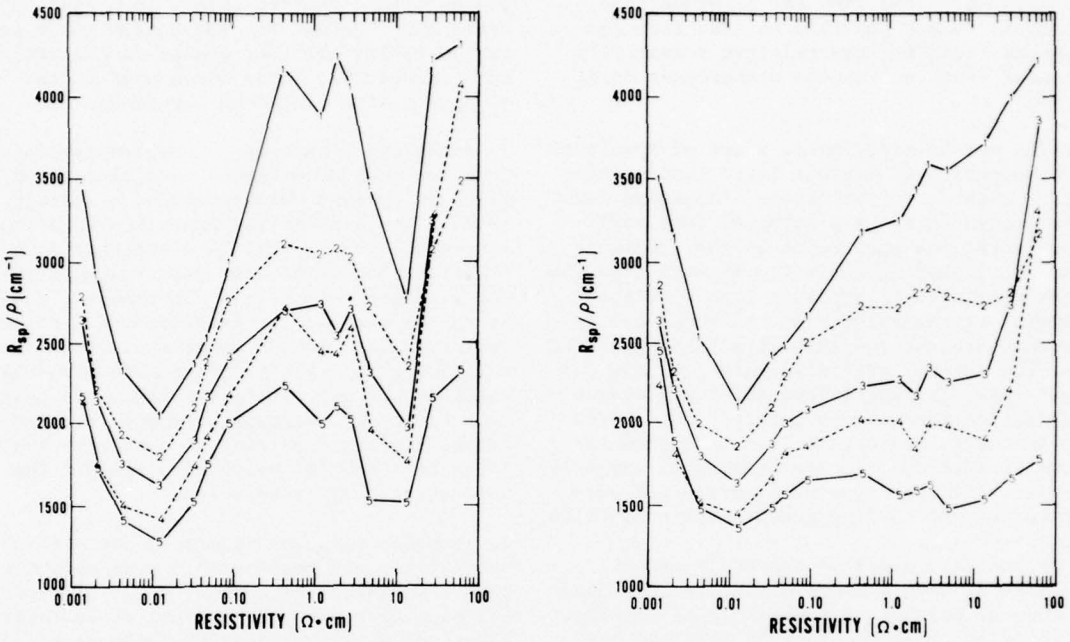

a. Not baked out.

b. Baked out.

Figure 2. Ratio of spreading resistance, R_{sp}, to resistivity, ρ, as a function of resistivity as measured with a variety of probe tips on (111) *n*-type silicon surfaces mechanically polished with 0.5-μm alumina in aqueous slurry. (1: tungsten-ruthenium alloy; 2: tungsten carbide; 3: osmium; 4: relatively sharp osmium-tungsten alloy; 5: relatively blunt osmium-tungsten alloy.)

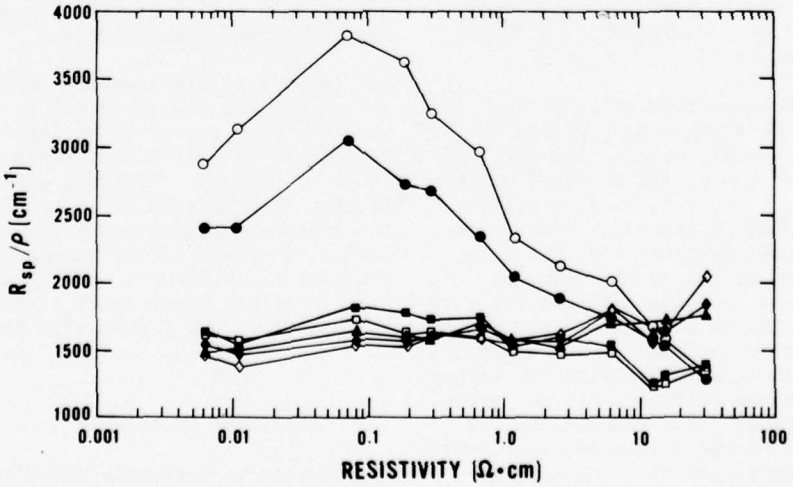

Figure 3. Ratio of spreading resistance, R_{sp}, to resistivity, ρ, as a function of resistivity as measured with relatively sharp osmium-tungsten alloy probe tips on (100) *n*-type silicon surfaces prepared in various ways. (Circles: lapped with 5-μm alumina; squares: chem-mechanically polished with silica sol; triangles: mechanically polished with 0.3-μm alumina in nonaqueous slurry; diamonds: mechanically polished with 0.3-μm alumina in aqueous slurry; solid points: not baked out; open points: baked out.)

cally polished with 0.3-μm alumina in an aqueous slurry. Measurements were made both immediately after polishing and after a subsequent bakeout in room air at 160°C for 20 min.

Results obtained on the specimen block with (111) *p*-type surfaces were very similar to those obtained previously on either of the types of chem-mechanically polished surfaces [3], silica sol [4] or zirconium silicate [5]. The spreading resistance response was very erratic for freshly prepared surfaces of specimens with resistivity greater than 0.2 Ω·cm, but a very stable, nearly linear relationship between resistivity and spreading resistance was obtained after bakeout.

On the specimen block with (111) *n*-type surfaces, the data obtained on the mechanically polished surfaces were unlike those obtained on either lapped or chem-mechanically polished surfaces. Prior to bakeout, data taken with all five probes exhibited very nonlinear ρ-R_{sp} relationships as shown in figure 2a. After bakeout, both sets of osmium-tungsten tips, one relatively sharp, one relatively blunted with use, showed a noticeably more constant ratio between spreading resistance and resistivity than did the other three probes shown in figure 2b. This probe material dependence was not seen for any other surface orientation or finish.

On the specimen block with (100) *n*-type surfaces the response obtained on the mechanically polished surfaces was similar to that on chem-mechanically polished surfaces. This is illustrated in figure 3 for the case of the relatively sharp osmium-tungsten probes. Note that there is no significant difference between data taken before and after bakeout. Generally, similar results were obtained with the other probes; a somewhat more linear relationship between R_{sp} and ρ was obtained with the relatively blunt osmium-tungsten probes. (J. R. Ehrstein and D. R. Ricks)

3.3. Spreading Resistance Profiles

As a preliminary test of the application of a simplified calculational procedure for correcting spreading resistance data on layers with nonuniform resistivity (NBS Spec. Publ. 400-19, p. 10), the dopant profiles of two boron-diffused layers were measured both by the spreading resistance method [6,7] and by the incremental sheet resistance method [8] and compared.

As previously described (NBS Spec. Publ. 400-19, p. 10), the diffused layers had a boron surface density slightly less than 10^{19} cm^{-3} and nominal junction depths of 1 and 2 μm. The incremental sheet resistance measurements were made by repetitively anodically oxidizing the specimen surface, stripping the oxide, and measuring the sheet resistance by the four-probe method [1]. The specimens measured were 1-in. (25-mm) diameter disks, ultrasonically machined from the center of each wafer. Prior to anodization, the disks were cleaned first in a mixture of approximately 5 parts (by volume) deionized water, 1 part hydrogen peroxide, and 1 part ammonium hydroxide; then in a mixture of approximately 6 parts deionized water, 1 part hydrogen peroxide, and 1 part concentrated hydrochloric acid; rinsed in deionized water; and dried in air [9].

The anodizing solution was made up by dissolving 3.86 g of potassium nitrate in 19.5 ml of deionized water and adding 946 ml of reagent-grade ethylene glycol which yields a 0.04 molal solution of potassium nitrate with 2 percent water. During anodization the back side of the disk is held against a carbon block electrode by means of a vacuum through a tube which surrounds the electrode. The disk was lowered face down into the anodizing solution which was contained in a glass beaker; a second tube around the electrode supplied a downdraft of nitrogen to keep the dielectric solution from creeping over the lip and oxidizing the back side of the disk.

A constant current, about 10 mA/cm^2, was passed through the disk; the positive electrode was a platinum wire spiral at the bottom of the beaker. To reduce forward resistance, the junction was illuminated by a 500-W projection lamp aimed through the side of the beaker. To offset the heating effect of the projection lamp, the anodizing solution was continually pumped through tubing resting in an ice bath. Upon returning to the main beaker, the solution was directed at the center of the wafer front surface through a nozzle about 1/8 in. (3.2 mm) in diameter about 1 in. (25 mm) away from the surface. The purpose of the jet was to clear the surface of bubbles and to provide refreshed solution at the wafer surface.

Current was supplied until the current supply was forced to provide about 270 V more than the turn-on voltage. The oxide thickness was determined from the measured voltage difference using a calibration curve established empirically with the use of ellip-

sometric determination of oxide thickness [10] over the range 40 to 160 nm. Typically the thickness of the oxide layer grown was about 145 nm. It was assumed that the amount of silicon removed was 0.44 times the oxide thickness [11].

Following each oxide growth step, the wafer was agitated in hydrofluoric acid for about 5 min to remove the oxide, rinsed in a flowing deionized water bath for about 10 min, and blown dry with nitrogen. Sheet resistance was measured with a collinear four-probe array with equally spaced probes, with 62-mil (1.59-mm) separation and tungsten carbide tips lapped flat (see sec. 3.1.) to give a contact radius of about 2 mils (50 μm). The probes were loaded with a force of 30 gf (0.29 N) each. Sheet resistance was measured over 20 to 25 increments, converted to sheet conductance, plotted as a function of position, and smoothed graphically. The local slope of the smoothed sheet conductance curve was calculated at 40-nm intervals to yield the bulk conductivity as a function of position. Bulk conductivity was converted to net acceptor density on the basis of Wagner's empirical relation [12].

Spreading resistance measurements were made with a commercial two-probe instrument (NBS Spec. Publ. 400-25, p. 9) on wafers diffused at the same time as the replicate wafer measured by the incremental sheet resistance method. Chips cut from the wafer were beveled at an angle of 0.50 deg with a silica sol solution [4] on a methyl methacrylate plate. Measurements were made at lateral intervals of 5 μm with well conditioned osmium-tungsten alloy probes loaded with a force of 20 gf (0.2 N) and spaced 50 μm apart.

Data were corrected by the local slope method. This is based on the assumption that, from parallel superposition (NBS Spec. Publ. 400-19, p. 10):

$$\sigma(x) = \frac{\ln(s/a)}{\pi} \frac{dG(x)}{dx} , \qquad (1)$$

where $\sigma(x)$ is the local bulk conductivity, s is the probe spacing, a is the effective radius of probe contact, and $G(x)$ is the conductance measured at a distance x from the insulating back surface of the layer. Equation (1) can be transformed into

$$\rho(x) = 2a\ R(x)/F, \qquad (2)$$

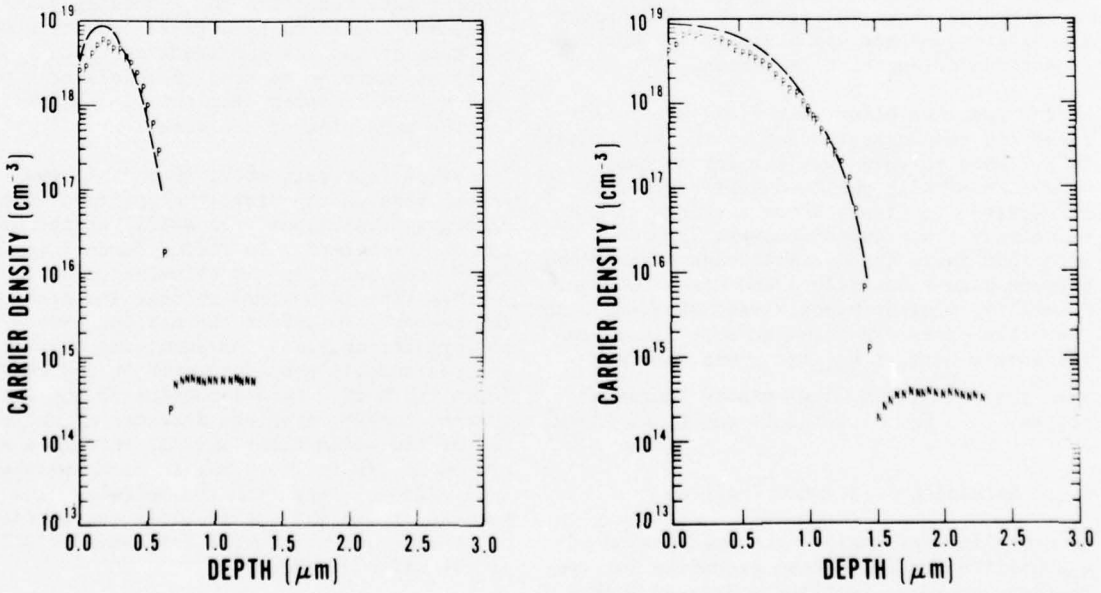

a. Specimen No. 1.

b. Specimen No. 2.

Figure 4. Dopant density profiles in boron-diffused *n*-type silicon as measured by the spreading resistance and incremental sheet resistance methods. (P and N: net boron and phosphorus density, respectively, from spreading resistance measurements, corrected by the local slope method; dashed curves: net boron density from incremental sheet resistance measurements.)

where $\rho(x) = 1/\sigma(x)$, $R(x) = 1/G(x)$ and

$$F = \frac{2a \ln(s/a)}{\pi} \frac{d[\ln R(x)]}{dx}, \quad (3)$$

where now x is the depth from the top surface of the specimen.

The effective contact radius was determined from measurements on a block of 15 homogeneous specimens (NBS Spec. Publ. 400-25, p. 9) which had been surfaced in the same way as the beveled surface of the diffused wafers. For homogeneous specimens the resistivity is given by*

$$\rho = 2aR. \quad (4)$$

Since both R and ρ are known, a may be calculated as a function of R. In the present case, a linear relation between ρ and R was found and a constant value of the effective contact radius was used.

The local slope of the $\ln R(x)$ *vs.* x curve at the ith point was found by taking the difference $(\log R_{i+1} - \log R_{i-1})$ and multiplying by the factor $[\ln 10/(x_{i+1} - x_{i-1})]$. At either end of the curve, differences were taken between adjacent readings and the interval was taken as $\Delta x = x_{i+1} - x_i$. The correction factor F was computed on a point-by-point basis using eq (3), and the resistivity was calculated at each point using eq (2). The resistivity was converted into net acceptor density on the basis of Wagner's empirical relation [12].

The results of these comparisons are shown in figure 4. The relatively close agreement suggests that the parallel superposition approach is quite accurate on this type of structure. One reason for some of the discrepancy near the surface on both specimens may be a bevel-rounding effect. It was assumed for the calculations that each successive point was a constant distance further below the original surface, but slight rounding of the bevel at its apex makes this a poor assumption for the first few points on the profile. Extensive additional comparisons will be required before conclusions can be drawn regarding the range of validity of this approach for determining correction factors. (J. R. Ehrstein, F. H. Brewer, and D. H. Dickey†)

3.4. Photovoltaic Method§

Interest in a rapid, nondestructive method for measuring resistivity uniformity of silicon slices has been rekindled because of the importance of this parameter in determining the characteristics and the performance of high-power semiconductor devices. Variations in the resistivity of a slice of starting material not only cause variations in the characteristics of devices fabricated from that slice, but can also contribute to poor yields in the manufacturing process and adversely affect the reliability of finished devices. For instance, poor junction geometry and nonuniform current distributions are frequent in devices fabricated from inhomogeneous material. Also, localized regions of low resistivity limit the ultimate device operating voltage to a value below that possible from the remainder of the device.

The feasibility of utilizing the bulk photovoltaic effect [13] for measuring resistivity variations along the diameter of a circular silicon slice has been demonstrated [14]. The technique was shown to be nondestructive in that no contact is required with the surface area on which devices are to be fabricated and to have better spatial resolution than the widely used four-probe method [15, 16]. However, to take advantage of the potential speed of this scanning technique it is necessary to automate the data collection and analysis procedures. Further, improvements in slice mounting and contacting are necessary to facilitate rapid exchange of specimens, and comparison of the spatial resolution with that of the spreading resistance method [6,7] is desirable.

The present task was undertaken to refine and automate the method and to compare its resolution with that of the spreading resistance method. A new specimen holder, illustrated in figures 5a and 5b, was designed to accommodate 2-in. (51-mm) diameter slices. This

*Note that in the limit of uniform, thick specimens eq (2) does not yield eq (4); this is because eq (2) is appropriate only for very thin layers with insulated back surfaces.

†Work performed at Solecon Laboratories under NBS Contract No. 5-35881.

§Principally funded by the Energy Research and Development Administration, Division of Electric Energy Systems.

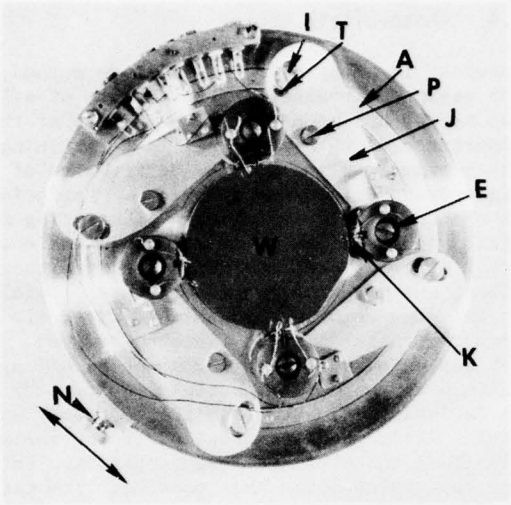

a. Specimen holder - top view.

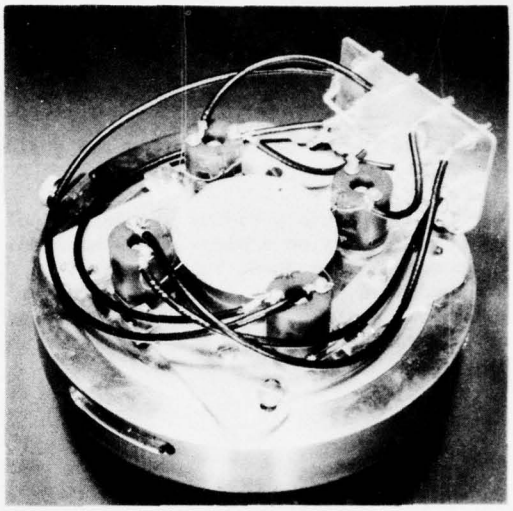

b. Specimen holder - side view

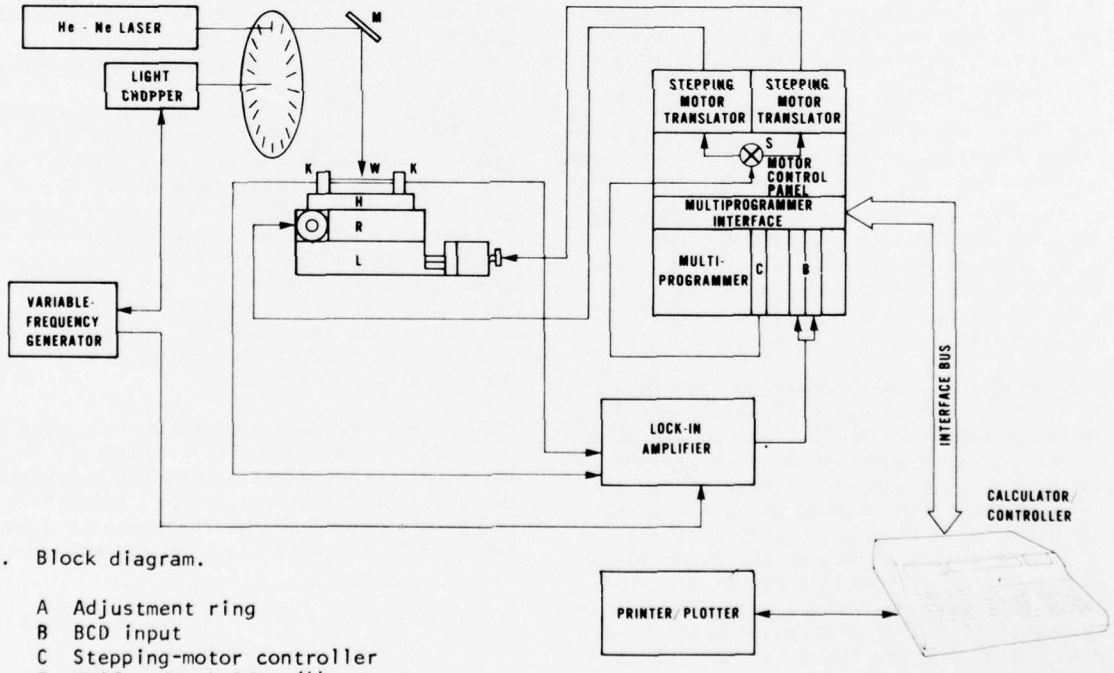

c. Block diagram.

A Adjustment ring
B BCD input
C Stepping-motor controller
E Knife-edge holder (4)
H Specimen holder base
I Pin (4)
J Lever (4)
K Knife edges (2 in each holder)
L Motor-driven linear stage
M Mirror
N Locking adjustment knob
P Pivot (4)
R Motor-driven rotary stage
S Double-pole, double-throw switch
T Guide notch (4)
W Slice under test

Figure 5. Prototype automated data collection and analysis system for resistivity profiling of circular silicon slices by the scanning photovoltaic method.

holder centers the slice with sufficient accuracy for the measurement. Each knife edge, K, has a single leaf spring behind it which permits enough freedom of movement to allow each to make contact with the circumference of the slice, W, at the same time. The four knife-edge holders, E, each holding two knife edges, move in concert at the ends of the levers, J. The levers are each pivoted at points, P, at 90-deg intervals from one another on the circumference of a common circle. As the adjustment ring, A, is moved by means of the locking knob, N, the pin, I, rides in a notch, T, of each lever which forces the four holders in or out together. Note that the knife-edge holders do not rotate at the ends of the levers. Thus, the four knife edges do not strike the wafer exactly at the ends of perpendicular diameters for slices of all diameters; however, the variation about the design slice diameter permitted by the SEMI specifications [17] is small enough that the locations at which the knife edges make contact do not change enough to affect the measurements significantly.

An automated data collection and analysis system was designed and assembled. A block diagram of this system is shown in figure 5c. The slice under test, W, is mounted in the holder, H, described above. For clarity, only two of the knife edges, K, are shown at opposite ends of a diameter. The holder is oriented on two stages so that the slice is concentric with the platform of the rotary stage, R, and so that the movement of the linear stage, L, is parallel to one of the diameters determined by the knife edges. The rotary stage has a rotational resolution of 2 min of arc and bidirectional rotational repeatability of 0.2 min of arc. The linear stage has a total travel of 85 mm, a linear resolution of 10 μm, and bidirectional linear repeatability of 5 μm.

Photo-excitation at a wavelength of 1.15 μm is furnished by a 2-mW helium-neon laser, which is mounted horizontally. The laser beam is directed to the center of the rotary stage by a mirror, M. The slice is scanned by moving the stage along a slice diameter under the stationary laser beam. The control card, C, for the stepping-motor in the multiprogrammer, operating under the direction of the calculator/controller, generates a pulse train of the appropriate length to move the stage the desired number of 10-μm steps in either direction; the pulse train is supplied to the motor windings through the selector switch, S, and the translator. End-point protection is provided by microswitches and appropriate relays at both ends of the stage travel.

During the first scan, the photovoltage is measured at predetermined points along the diameter. To improve the signal-to-noise ratio, the beam is chopped and the photovoltage is measured by a lock-in amplifier which is synchronized to the frequency of the chopped light beam. The chopping frequency is adjusted so that the on time of the laser beam is long enough to achieve a steady-state excess-carrier distribution. Following the first scan, a second scan along the same diameter is made; during this scan the photoconductivity is measured at the same points along the diameter as before. This measurement requires that a small current be passed along the diameter of the slice (using one pair of knife edges) while the potential drop across the diameter is measured as a function of light position (using the other pair of knife edges). The calculator/controller, which together with its associated multipro grammer and printer/plotter is compatible with standard interface requirements [18], records the data, performs the calculations required to obtain the resistivity, and plots the results. After measurements along the first diameter are completed, the wafer can be rotated 90 deg and the measurements repeated. (G. J. Rogers and D. L. Blackburn)

3.5. Reevaluation of Irvin's Curves

Additional room-temperature resistivity and dopant density measurements were made on silicon wafers doped with phosphorus as part of the continuing experimental redetermination of the resistivity-dopant density relation first reported by Irvin [19]. In addition, initial measurements were made on silicon wafers doped with boron.

The measurements were made on test structures included in test pattern NBS-3 [20]. Dopant density values were obtained from measurements on structure 3.10, base-collector diode (NBS Spec. Publ. 400-17, pp. 27-28), by the junction capacitance-voltage (C-V) method. The gate on the structure was biased at the flat-band voltage as determined from measurements on structure 3.8, MOS capacitor over collector (NBS Spec. Publ. 400-17, pp. 26-27). Instead of calculating discrete dopant density values from the C-V data as has been done previously (NBS Tech Note 788, pp. 9-11), a new data reduction procedure was developed in which a Gaussian shape is assumed for the base diffusion near the junction and the sur-

Table 4 — Preliminary Electron Mobility Data for Phosphorus-Doped Silicon at 300 K

Wafer No.	No. of diodes	$\bar{\rho}$, $\Omega \cdot cm$	N, cm^{-3}	μ, $cm^2/V \cdot s$
B38Ph-1	6	31.3	1.43×10^{14}	1409 ± 69
B12Ph-1	10	13.5	3.34×10^{14}	1392 ± 70
D2.4Ph-1	8	2.46	1.93×10^{15}	1314 ± 33
A2.0Ph-2	4	2.14[a]	2.25×10^{15}	1300 ± 47
B1.4Ph-3	7	1.36	3.57×10^{15}	1295 ± 87
A1.0Ph-1	4	1.05	4.78×10^{15}	1240 ± 24
B0.77Ph-1	6	0.801	6.36×10^{15}	1227 ± 33
B0.47Ph-1	8	0.504	1.08×10^{16}	1156 ± 51
A0.27Ph-2	4	0.278	2.13×10^{16}	1052 ± 29
B0.099Ph-1	4	0.101[a]	7.59×10^{16}	815 ± 9
B0.051Ph-2	4	0.052[a]	2.17×10^{17}	556 ± 25
B0.050Ph-1	4	0.051	2.25×10^{17}	544 ± 7
A0.022Ph-2	4	0.022[a]	1.17×10^{18}	248 ± 4

[a]Resistivity as measured by mechanical four-probe array before processing.

Table 5 — Preliminary Hole Mobility Data for Boron-Doped Silicon at 300 K

Wafer No.	No. of diodes	$\bar{\rho}$, $\Omega \cdot cm$	N, cm^{-3}	μ, $cm^2/V \cdot s$
A12B-1	4	11.5	1.18×10^{15}	457 ± 7
B5.7B-3	4	5.85[a]	2.42×10^{15}	440 ± 3
B1.1B-3	4	1.16	1.29×10^{16}	415 ± 8
B0.72B-3	5	0.72	2.22×10^{16}	391 ± 14
D0.58B-2	6	0.587	2.92×10^{16}	364 ± 2
B0.090B-2	7	0.0903	3.40×10^{17}	204 ± 3

[a]Resistivity as measured by mechanical four-probe array before processing.

face concentration of the diffusion and the background dopant density are adjusted to give a best fit to all the C-V data. This procedure has made it possible to obtain results on wafers with dopant densities greater than 10^{17} cm^{-3} which could not be measured by the previous approach.

The bulk resistivity of the wafers was determined from measurements on structure 3.17, four-probe collector resistor (NBS Spec. Publ. 400-17, pp. 25-26) [21]. For a few wafers, the resistivity used for calculating mobility was that determined prior to processing by mechanical four-probe measurements [2]. These were either wafers for which the emitter diffusion was omitted in order to obtain a shallow base junction depth or wafers processed with the large-pipe base mask which introduced a significant uncertainty in the pipe spacing [21].

The carrier mobility, μ, was calculated from

$$\mu = (Nq\rho)^{-1}, \qquad (5)$$

where N is the carrier, or net dopant, density, q is the electronic charge, and ρ is the resistivity corrected to 300 K. To minimize the influence of resistivity variations over the wafer the average of the resistivities measured on the two collector resistors¶ on either side of the diode used to determine N was used for ρ in eq (5). The procedure was repeated for a number of good diodes in the same general area of the wafer, usually near the center, to arrive at an average mobility as listed in tables 4 and 5. The uncertainty in the mobility for each wafer is the sample standard deviation calculated from the individual mobility values. Table 4 contains revised electron mobility values based on repeated and additional measurements for wafers reported on previously (NBS Spec. Publ. 400-19, p. 25). In general the electron mobility values lie above those which would be predicted using the Caughey-Thomas fit [22] to Irvin's data (see sec. 3.6.), and the hole mobility values lie below those which would be predicted using Wagner's empirical relation [12]. (W. R. Thurber, R. L. Mattis, Y. M. Liu, M. L. Doggett, and M. G. Buehler)

3.6. Electron Mobility in Phosphorus-Doped Silicon

Traditional analysis of electron mobility in *n*-type silicon has neglected the effects of electron-electron scattering and scattering anisotropy in the mobility calculations. As a result, theory fails to conform with experiment when dopant density exceeds 2×10^{16} cm^{-3} (NBS Tech. Note 806, pp. 20-23). By incorporating these effects, good agreement between theory and experiment for both electron mobility and resistivity was obtained for phosphorus-doped silicon slices with dopant density from 10^{14} to 3×10^{18} cm^{-3} over the temperature range 100 to 500 K [23,24].

Initially the lattice mobility, taken from the work of Norton *et al.* [25], was combined with the ionized impurity mobility, as calculated by Long [26], according to the sine-and-cosine-integral method [27] to obtain the mixed scattering mobility. This was combined reciprocally with the neutral impurity mobility, as calculated by Sclar [28], to obtain the total electron mobility. The mobility calculated in this way for 300 K is shown as curve 1 of figure 6. For comparison, the Caughey-Thomas fit [22] to Irvin's data [19] is shown as curve 2 and more recent experimental results are shown as data points; the solid dots are taken from the mobility data of Mousty *et al.* [29] and Baccarani and Ostoja [30], corrected to 300 K, and the open circles are NBS data obtained on processed phosphorus-doped silicon wafers (see sec. 3.5.).

It can be seen that the calculated result fits the more recent experimental data for dopant density less than 2×10^{16} cm^{-3}. However, at higher dopant density, the calculated curve is higher than the experimental data.

While electron-electron scattering does not affect the current density directly since it cannot alter the total momentum, it tends to randomize the way in which this total momentum is distributed among electrons with different energy. When the scattering mechanism is such as to lead to a nonuniform distribution, electron-electron scattering gives rise to a net transfer of momentum from electrons which dissipate momentum less efficiently to those which dissipate momentum more efficiently, resulting in an overall greater rate of momentum transfer and lower mobility. The size of the effect of electron-electron scattering on the mobility is a function of the energy dependence of the relaxa-

¶When the resistivity was measured by means of a mechanical four-probe array, the resistivity value for the location was based on radial profiles along two diameters of the wafer.

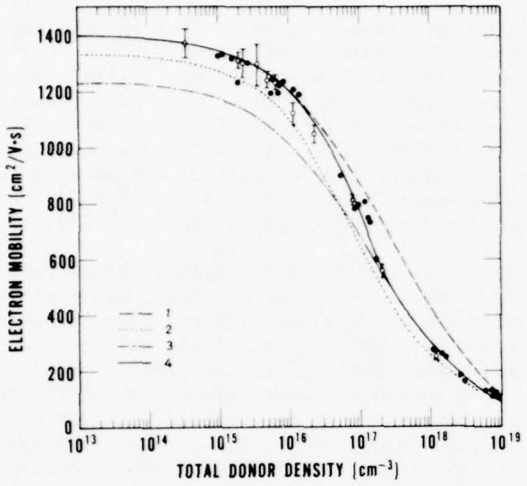

Figure 6. Conductivity mobility of electrons at 300 K as a function of total donor density for phosphorus-doped silicon. (Curve 1: Theoretical, not including electron-electron scattering; Curve 2: Caughey and Thomas representation of Irvin's curve [22]; Curve 3: Theoretical, including maximum electron-electron scattering over entire range; Curve 4: Theoretical, including electron-electron scattering in intermediate and high dopant density ranges; open data points: experimental, this work; solid data points: experimental [29,30].)

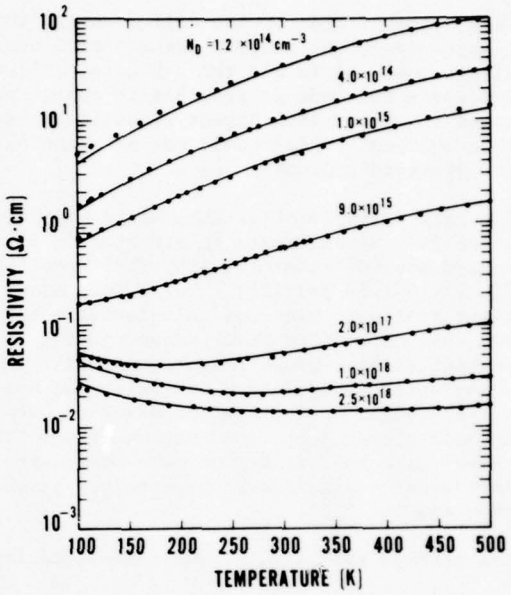

Figure 7. Resistivity as a function of temperature for seven phosphorus-doped silicon slices. (Solid points are measured values and curves are calculated assuming the phosphorus density, N_D, as indicated on the curves.)

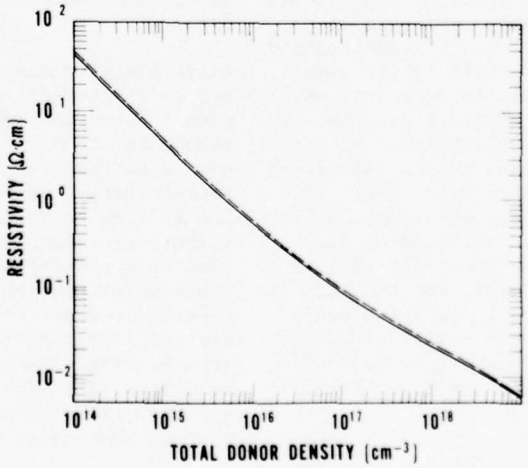

Figure 8. Resistivity of phosphorus-doped silicon at 300 K as a function of total donor density. (Solid curve: this work; dashed curve: from Irvin [19].)

tion time. Thus, for neutral impurity scattering where the relaxation time is independent of energy, the mobility is not affected by electron-electron scattering. Ionized impurity scattering would be expected to be much more affected than lattice scattering since in the former case the relaxation time is proportional to the three-halves power of the energy, while in the latter it is inversely proportional to the square root of the energy.

From the work of Luong and Shaw [31], it is found that electron-electron scattering reduces the ionized impurity mobility in uncompensated n-type silicon by a maximum of 36.8 percent while, from other published work [27, 32], it can be shown that electron-electron scattering reduces the lattice scattering mobility by a maximum of 12 percent. Using these values, the electron mobility at 300 K was calculated as above; the result is shown as curve 3 in figure 6. This agrees well with the experimental data for dopant density above about 2×10^{17} cm^{-3}. In the intermediate region, for dopant density between 2×10^{16} and 2×10^{17} cm^{-3} it was assumed that the reduction factor, F, for both ionized impurity and lattice mobility varies linearly with dopant density

$$F = F_{max} \frac{N}{1.8 \times 10^{17}} - \frac{1}{9},$$

where $F_{max} = 0.12$ for lattice mobility and 0.368 for ionized impurity mobility. With this assumption, and assuming $F = 0$ for dopant density less than 2×10^{16} cm^{-3} and $F = F_{max}$ for dopant density greater than 2×10^{17} cm^{-3}, one obtains curve 4 in figure 6 for the electron mobility at 300 K. This curve agrees with the experimental data to within about ±5 percent over the entire dopant density range shown. Note that the electron mobility in lightly doped n-type silicon appears to be significantly higher than that based on Irvin's data [19,22].

At other temperatures, it is not convenient to measure the carrier density directly. The resistivity, ρ, is given by

$$\rho = (nq\mu_n)^{-1},$$

where n is the electron density. Therefore, if μ_n is obtained as a function of dopant density and temperature as described above and n is obtained as a function of dopant density and temperature by solving the charge-balance equation [23,24], it is possible to obtain calculated resistivity-temperature curves for various values of dopant density which can be compared with experimentally determined curves.

To make this comparison, resistivity measurements were made between 100 and 500 K on seven phosphorus-doped silicon wafers, using the four-probe collector resistor (NBS Spec. Publ. 400-17, pp. 25-26) [21]. The test cells used for the resistivity measurements were taken from the same silicon wafers used for the mobility measurements at 300 K. For the temperature dependent measurements, a test cell containing the four-probe structure was mounted on a TO-5 header; a temperature-sensing diode was also mounted next to the cell for measuring the temperature. The TO-5 header was then mounted inside a specially-designed cryostat where temperatures can be varied from 82 to 673 K with a maximum heating rate of 7 K/s (NBS Tech. Note 788, pp. 12-14) [33]. The results are illustrated in figure 7; the solid dots are measured values and the curves are values calculated with the assumption of the phosphorus density, N_D, indicated on the curve. Over the entire range shown, the theoretically predicted resistivity values are within ±7 percent of the experimental data. The values of N_D were found from the measured resistivity at 300 K using the calculated resistivity-dopant density curve shown as the solid line in figure 8.

(S. S. Li and W. R. Thurber)

3.7. Thermally Stimulated Current and Capacitance Measurements

Application to Power-Grade Silicon[#] — Many critical properties of high-power silicon thyristors and rectifier diodes are significantly affected by the presence of impurity and defect centers which cannot be counted or identified by ordinarily used electrical measurements such as resistivity and lifetime. Many such centers, such as heavy metal contamination, irradiation-induced defects, and process-induced defects have been identified by means of their thermally stimulated current or capacitance response, and each defect is noted to have a particular signature. Although the measurement of thermally stimulated current and capacitance is reasonably well established [34-38], several aspects need further development before the tech-

[#]Principally funded by the Energy Research and Development Administration, Division of Electric Energy Systems.

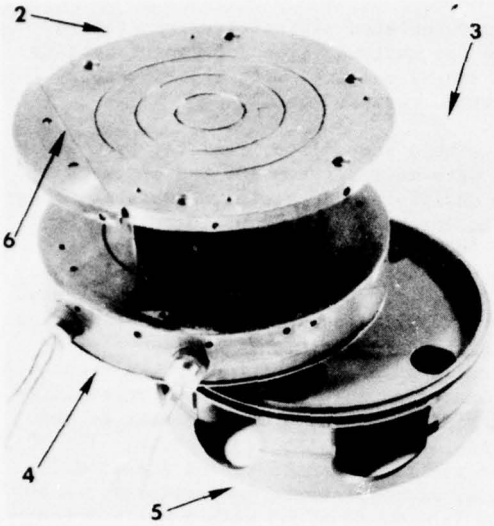

a. Chuck assembly - exploded view.

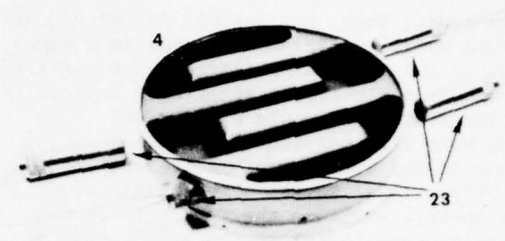

b. Heating module - inverted view.

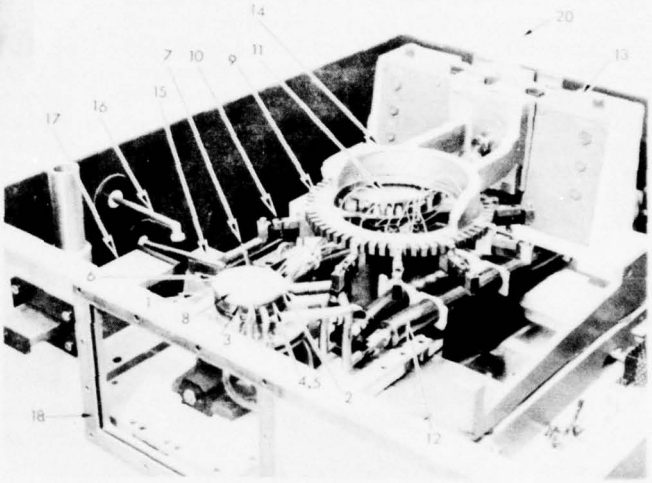

c. Automatic wafer prober - interior view.

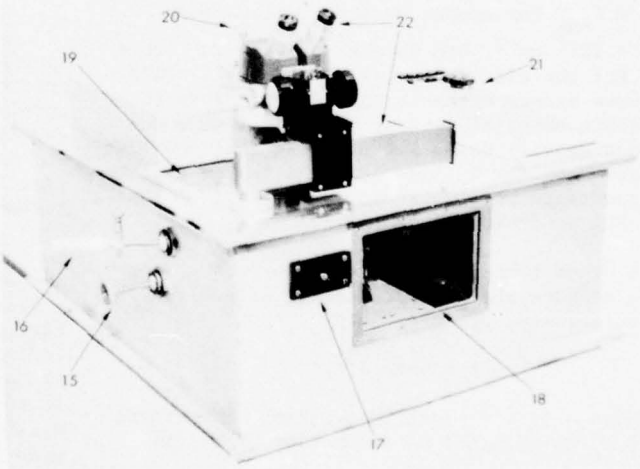

d. Prober assembly - exterior view.

1 Chuck assembly
2 Copper top plate
3 Insulator plate
4 Heating module
5 Cooling module
6 Wafer index stop
7 Thermocouples
8 Wafer
9 Probe ring
10 Probe manipulator
11 Multiprobe assembly
12 Bellows
13 Prober bridge
14 Probe ring support
15 Wafer alignment manipulator
16 Vacuum pick-up probe
17 Transfer slide
18 Front viewport
19 Top viewport
20 Probe ring height manipulator
21 Prober control panel
22 Microscope and mount
23 Heaters

Figure 9. Thermally controlled chuck and automatic wafer prober.

nique can be widely applied to the characterization of power-grade silicon; a new task area has been initiated to carry out this work.

To date, all measurements reported in the literature have been made in cryostats on small, individual devices scribed from processed wafers bonded onto headers. One objective of the task is the development of apparatus suitable for performing thermally stimulated current and capacitance measurements on whole large diameter silicon wafers. Use of such an apparatus would eliminate the need for further processing of test specimens after wafer fabrication and allow relatively fast feedback of information to the process line.

Since it is desired to characterize starting material as well as material at various stages in the device fabrication process, it is necessary to develop procedures for fabricating test structures which preserve the characteristics of the starting material. The possibility of examining starting material was made feasible by the observation that MOS capacitors were just as suitable for the measurement as p-n junctions (NBS Spec. Publ. 400-1, pp. 16-19) and that both structures yielded the same information (NBS Spec. Publ. 400-4, pp. 27-33). However, to exploit this possibility, low-temperature processes for forming the capacitor oxide and gate electrode must be refined; this is a second objective of the task.

Application of the measurement technique at various stages in thyristor fabrication is complicated by the fact that not all regions of the device are accessible externally; a third objective of the task is to determine the feasibility of using monitor wafers and special process steps to enable the measurement after all key thyristor fabrication steps.

Initial work has concentrated on the first two objectives:

A. Whole-Wafer Apparatus. One major component of the whole-wafer apparatus is a large-area, thermally-controlled chuck, optimized for its thermal response and capable of operation over a temperature range from about 80 to over 600 K. The chuck consists of several components as shown in the exploded view in figure 9a. The copper top plate (2) has vacuum grooves for specimen holddown and a hole for attachment of a thermocouple. A thin insulator plate (3) separates the top plate from the heating-cooling module (4,5). The copper upper section (4) of this module consists of an integral cooling cavity and heater elements. An inverted view of this module with the four 150-W heater elements exposed is shown in figure 9b. The stainless steel lower section (5) encloses the cooling cavity and forms the manifold for the liquid nitrogen coolant; this section is heli-arc welded to the copper section. The lower section has been designed with a thin rib on the circumference to minimize heat transfer to the supporting hardware. The top surface of the heating module (4) is identical (including vacuum grooves and thermocouple hole) to the top plate; for measurements which do not require electrical isolation, the top plate and insulator can be removed to permit faster thermal response. The wafer index-stop (6) may be attached either to the top plate or the heating module.

Parallel to the development of the chuck is the modification of an automatic wafer prober to accommodate the chuck and to allow the capability to screen individual devices on a wafer for mobile ion contamination and for oxide integrity before making the thermally stimulated current or capacitance measurements. The prober and associated parts are illustrated in figure 9c together with the mounted chuck assembly (1); the bridge structure (13) to which the probe ring support (14) is mounted has been moved back to separate the probe ring (9) from the chuck assembly (1) for greater clarity of presentation in the photograph. The probe ring, which normally accommodates up to 60 probe manipulators (10) has been modified to allow mounting of an optional multiprobe assembly (11), which can be used in place of separate manipulators to apply bias and temperature stresses to 36 devices on a wafer simultaneously as a convenient method for detection of mobile ion contamination. The separate manipulators are commercial units modified to allow the use of miniature 50-Ω shielded coaxial cables which is necessary to minimize the stray capacitance in the input leads to the 1-MHz capacitance bridge. The bellows (12) are used to transport liquid nitrogen to and from the cooling module. In operation, the wafer is placed on the transfer slide (17) and pushed into the enclosure; by means of the vacuum pick-up probe (16), the wafer is transferred from the slide to the top plate of the chuck (2) and aligned to the raised stop (6). Fine adjustment of the wafer alignment with the prober axes can be made by rotating the chuck about a vertical axis through its center by means of the alignment manipulator (15).

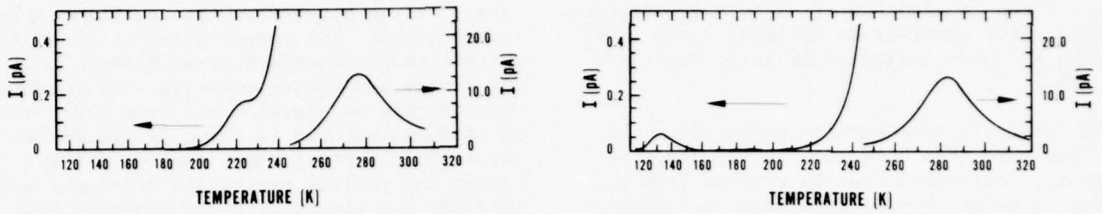

a. Gold acceptor in n-type silicon. Specimen 59B H4-3; -7 V cooling; -15 V heating; heating rate, ∿2 K/s.

b. Gold donor in p-type silicon. Specimen 60 B A1-8; +10 V cooling; +20 V heating; heating rate, ∿2 K/s.

Figure 10. Thermally stimulated current response of gold-doped silicon MOS capacitors in wafer form.

The prober assembly is surrounded by a hermetic enclosure, shown in the exterior view in figure 9d. All components are sealed to the wall of the enclosure with rubber O-rings or gaskets. The top (19) and front (18) viewports have light-tight covers (not shown) to provide a dark measurement environment. The enclosure is constantly flushed and slightly pressurized (6 psig or 40 kPa) with dry nitrogen to minimize room air penetration; the exhaust gases can be monitored for moisture. A microscope (22) is provided to check wafer alignment through the top viewport (19); the microscope support assembly was modified to allow clearance for the viewport between the microscope objective and the wafer (8). The relative spacings and orientation of the probes must be preset, but the vertical adjustment is accessible by means of the probe ring manipulator (20). All the utility ports are located in the back of the enclosure; these include vacuum, heater power, liquid nitrogen, thermocouple signals, prober control interfacing, and dry nitrogen pressurization.

Prior to completion of this apparatus, an earlier version (NBS Spec. Publ. 400-4, pp. 39-40) was modified to increase its maximum heating rate to 2 K/s in order to conduct preliminary feasibility studies of measuring thermally stimulated current and capacitance at the wafer level as described below.

(R. Y. Koyama and L. M. Smith)

MOS capacitors were made with aluminum gates and thermal oxides on n- and p-type silicon doped with gold. The thermal responses of the gold acceptor in n-type silicon and the gold donor in p-type silicon were measured on the unscribed wafers and, as illustrated in figure 10, were found to be the same as those reported in the literature for measurements on packaged diodes and capacitors [38, 34] except in the case of one n-type wafer where the oxide was inadvertently contaminated, probably with sodium. These results demonstrated that measurements at the wafer level were feasible. However, because mobile ion contamination may be encountered in the low-temperature oxides, it was decided to investigate the contaminated wafer more fully.

In the as-processed condition, the response, shown as curve a in figure 11, includes a current peak near the expected temperature of the phase I emission (vertical arrow) but the

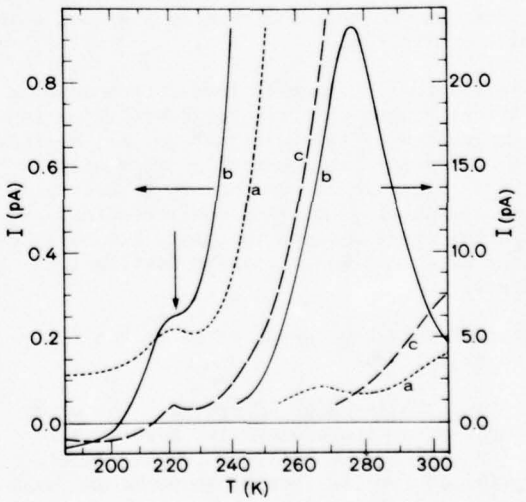

Figure 11. Thermally stimulated current response of gold-doped n-MOS capacitor with an oxide film contaminated by mobile ions. (a: as processed; b: ions moved to metal gate; c: ions moved to $Si-SiO_2$ interface; heating, both cases: ∿2 K/s; specimen 62B B4-8.

phase II response, at higher temperatures, is very different from the normal response. Following a bias-temperature stress on the capacitor which drove any mobile ions which were present in the oxide to the metal-oxide interface, the normal response of the gold acceptor was obtained. This response, shown as curve b in the figure, has the phase I shoulder at about 225 K and the phase II peak at about 280 K. If the mobile ions are driven to the silicon-oxide interface by a second (reversed) bias-temperature stress, the response again becomes abnormal as shown in curve c of the figure. These results suggest that the presence of mobile charge at or near the silicon-oxide interface greatly affects the charge state or the emission process of the traps in the depletion region of the semiconductor. However, by removing such mobile charge from the interface, it is still possible to obtain the proper thermally stimulated current response. The presence of mobile ion contamination can be determined by means of bias-temperature stress measurements (NBS Spec. Publ. 400-19, pp. 29-30) prior to the thermally stimulated current measurement.

(R. Y. Koyama)

B. Low-Temperature Processing of MOS Capacitors. Typical processing of MOS capacitors for thermally stimulated current and capacitance measurements includes the following principal steps:

1. Clean wafer,
2. Grow silicon dioxide 0.1 to 0.2 μm thick in dry oxygen at 1000°C,
3. Deposit aluminum,
4. Photoengrave gate contacts with level 4 (METAL) mask of test pattern NBS-3 [20],
5. Metallize back side, and
6. Microalloy at 500°C for 20 min in dry nitrogen.

The high-temperature oxidation step in this process is likely to cause alterations in the impurity and defect characteristics of the material. Hence the suitability of three types of oxides for forming the capacitor dielectric at lower temperatures is being considered: anodic oxidation of silicon at room temperature, chemical vapor deposition (CVD) of silicon dioxide at 400°C, and oxidation at 400°C of evaporated tantalum to form tantalum pentoxide.

Capacitance-voltage (C-V) characteristics were used to determine the properties of the various oxides. The C-V curves were analyzed to find the oxide thickness, X_o; the average dopant density, N_D, in the depletion region; and the flat-band capacitance, C_{fb}. The flat-band voltage, V_{fb}, was determined directly from C_{fb}.

Figure 12 displays typical measured C-V characteristics for each of the oxide types fabricated. For comparison purposes, the C-V characteristics of a standard, dry thermal oxide are also shown in the figure. Theoretical curves [39] are shown as dots for comparison; these points have been shifted along the voltage axis to allow coincidence of V_{fb} with the experimental value. The silicon-dioxide capacitors (curves a, b, and d) show similar characteristics; the flat-band voltage is negative (indicating a positive surface-state charge) and the experimental curve lies above the theoretical one in the inversion region (indicating interface-state dispersion). By contrast, the tantalum pentoxide capacitor (curve c) shows a negative surface-state charge and the theoretical curve shows higher dispersion than the experiment. Since the dielectric film in this case was very thin, it is not clear that the C-V measurement is valid because of the possibility of leakage in the oxide; hence, it is possible that the devices goes into deep depletion rather than to true inversion. (F. H. Brewer, R. Y. Koyama, J. Krawczyk, Y. M. Liu, and D. A. Maxwell)

At this time, due to the ease of in-house fabrication, the CVD silicon dioxide is the most promising low-temperature oxide. However, neither the anodic silicon dioxide or the tantalum pentoxide processes have been eliminated from consideration.

The low-temperature processing procedure was further tested with a lot of n-type, 10 Ω·cm <100> silicon wafers which had been diffused with gold to introduce the known gold acceptor [38]. These simulated starting wafers were then processed with a 400°C CVD oxide and 500°C microalloyed aluminum metallization.

Thermally stimulated current measurements were made on these capacitors in the modified wafer apparatus. Although detailed measurements were not made, the response of the gold acceptor was clearly observed. These results indicate that the MOS structure used in these measurements is a suitable vehicle for detecting defects in the starting material.

(R. Y. Koyama)

The microalloy step is necessary with aluminization using an e-gun source. This is done

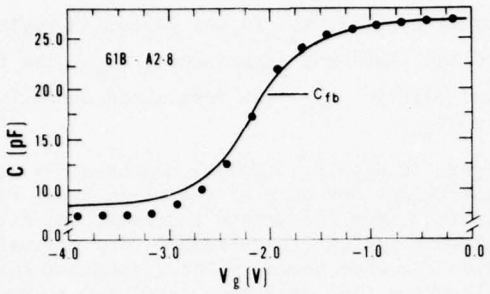

a. Chemical vapor deposited silicon dioxide, 142.5 nm thick.
$N_D = 6.6 \times 10^{14}$ cm^{-3};
$V_{fb} = -2.07$ V.

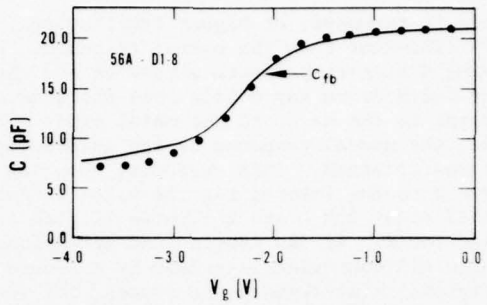

b. Anodically grown silicon dioxide, 180.8 nm thick.
$N_D = 6.7 \times 10^{14}$ cm^{-3};
$V_{fb} = -2.12$ V.

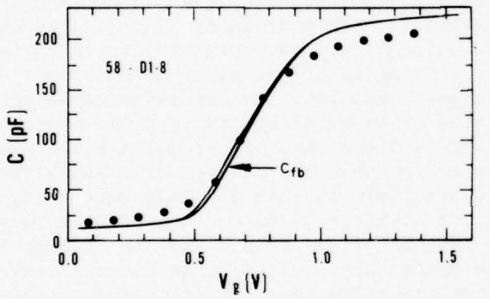

c. Oxidized tantalum (Ta_2O_5), 33.1 nm thick.
$N_D = 1.6 \times 10^{15}$ cm^{-3};
$V_{fb} = 0.62$ V.

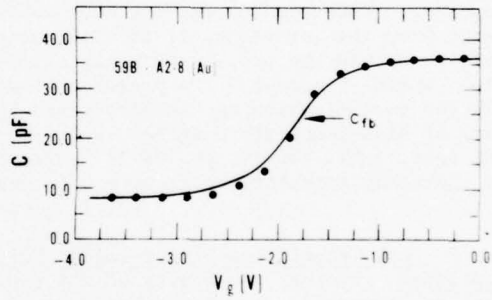

d. Thermally grown silicon dioxide (dry), 105.3 nm thick.
$N_D = 6.7 \times 10^{14}$ cm^{-3};
$V_{fb} = -1.77$ V.

Figure 12. Capacitance-voltage characteristics of various oxides on *n*-type silicon with aluminum gate electrodes. (Solid lines: measured values; dots: theoretical values, displaced to account for flat-band voltage.)

to remove the interface state dispersion in the C-V curve due to the x-ray damage [40] (see sec. 5.2.) from the e-gun. In addition, it promotes better adhesion of the aluminum to the oxide surface. Since this microalloy temperature was higher than the maximum oxide fabrication temperature, a series of measurements was conducted to see if a lower microalloy temperature would be acceptable.

Four wafers were processed with dry thermal oxides, about 90 nm thick. After gate metallization (e-gun aluminum) and photoengraving, each of the four wafers was microalloyed at a different temperature for 20 min in dry nitrogen. Capacitance-voltage measurements were made on MOS capacitors of the resulting wafers; the results are displayed in figure 13. Four C-V measurements from each of the four wafers are shown. Wafer 74A was not microalloyed at all. It shows the typical interface state distortion accompanied by the higher than normal flat-band voltage shift due to the x-ray damage. The other three wafers, 74C, 74B, and 74D, alloyed at 300°, 400°, and 500°C, respectively, show very little interface-state distortion but varying quantities of oxide charge. From the standpoint of thermally stimulated current and capacitance measurements, the presence of oxide charge is not a problem, providing that it remains stable. Since this is usually the case, the 400°C microalloy step would be appropriate for use. (R. Y. Koyama and J. Krawczyk)

Tentative Catalog of Defect Centers — In order to utilize the thermally stimulated current or capacitance response of a diode or capacitor to identify impurities and defects in silicon, it is necessary to know the char-

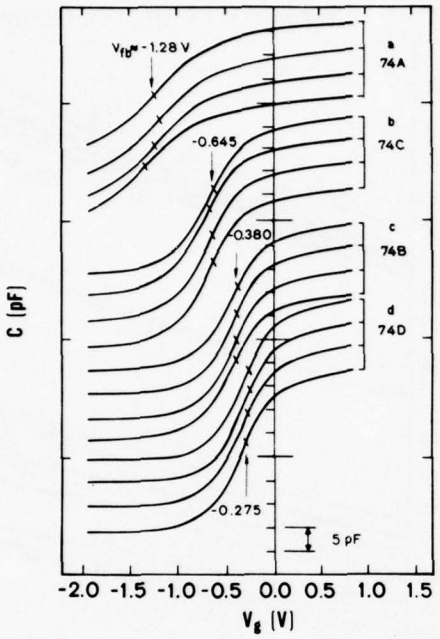

Figure 13. Capacitance-voltage characteristics of four MOS capacitors on each of four *n*-type silicon wafers with dry thermal oxides, about 90 nm thick, and e-gun evaporated aluminum gates microalloyed at different temperatures. (For clarity, the curves are displaced vertically; the oxide capacitance is about 42 pF. Curves a: no alloy treatment; curves b: microalloy temperature, 300°C; curves c: microalloy temperature, 400°C; curves d: microalloy temperature, 500°C.)

acteristic responses of such impurities and defects. Emission coefficients and activation energies of 31 impurity or defect centers in silicon were compiled from the literature and used as the basis of plots of the temperature, T_e, at which the majority carrier (phase I) thermal emission from charged defect centers produces a discharging current peak as a function of the heating rate, β, at T_e. Impurities include cobalt [41], gold [42], irridium [43], platinum [44], rhodium [43], silver [45], sulfur [46], tantalum [47], and zinc [48]. Defects include those induced by 1-MeV electron irradiation [49], 1.5-MeV electron irradiation [50], 1-MeV neutron irradiation [50], and high-temperature processing [50,51].

To obtain the T_e-β curves, the relationship between β and T_e previously derived for electron emission in *n*-type silicon (NBS Spec. Publ. 400-4, p. 31) was rearranged and generalized as:

$$\beta = \frac{B_x T_e^{\,3} \exp(-\Delta E_x/kT_e)}{2 + \Delta E_x/kT_e} \qquad (6)$$

where B_x is the emission coefficient, the subscript x is n or p designating the conductivity type of the silicon, k is Boltzmann's constant, ΔE_n is $E_c - E_t$, and ΔE_p is $E_t - E_v$ (energy levels of the defect center as measured from the conduction and valence bands respectively). The model used for this calculation [38] assumes a single emission process (minority carrier emission rate is trivial at the majority carrier emission current peak) and a small defect density relative to the dopant density. Violation of the former condition, as in the case of the mid-gap gold center, shifts the peak temperature only by 1 K. Uncertainties in the emission coefficients and activation energies of the order generally reported in the literature result in uncertainties of only a few degrees in the peak temperature. The model also assumes that the emission rates are described by the empirical equation of Arrhenius of the form: $e_x = B_x T^2 \exp(-\Delta E_x/kT)$. Because the temperature variation of the emission is so dominated by the exponential term when $\Delta E_x/kT$ is fairly large, experiments cannot distinguish between various values of s in the more general form: $e = AT^s \exp(-\Delta E_x/kT)$ [52]. The value 2 for s was adopted since it corresponds to a temperature independent cross section.

The T_e-β curves are given in figure 14; the values of emission coefficient and activation energy used to construct these curves are listed in table 6. The intersection of a horizontal line at the peak temperature with a vertical line at the heating rate should occur on the T_e-β curve of the center responsible for the response.

It would be desirable to add to this catalog centers which result from other impurities including copper, iron, lithium, manganese, mercury, molybdenum, nickel, neodymium, oxygen, thalium, thulium, tungster, and vanadium.

(M. G. Buehler and W. E. Phillips)

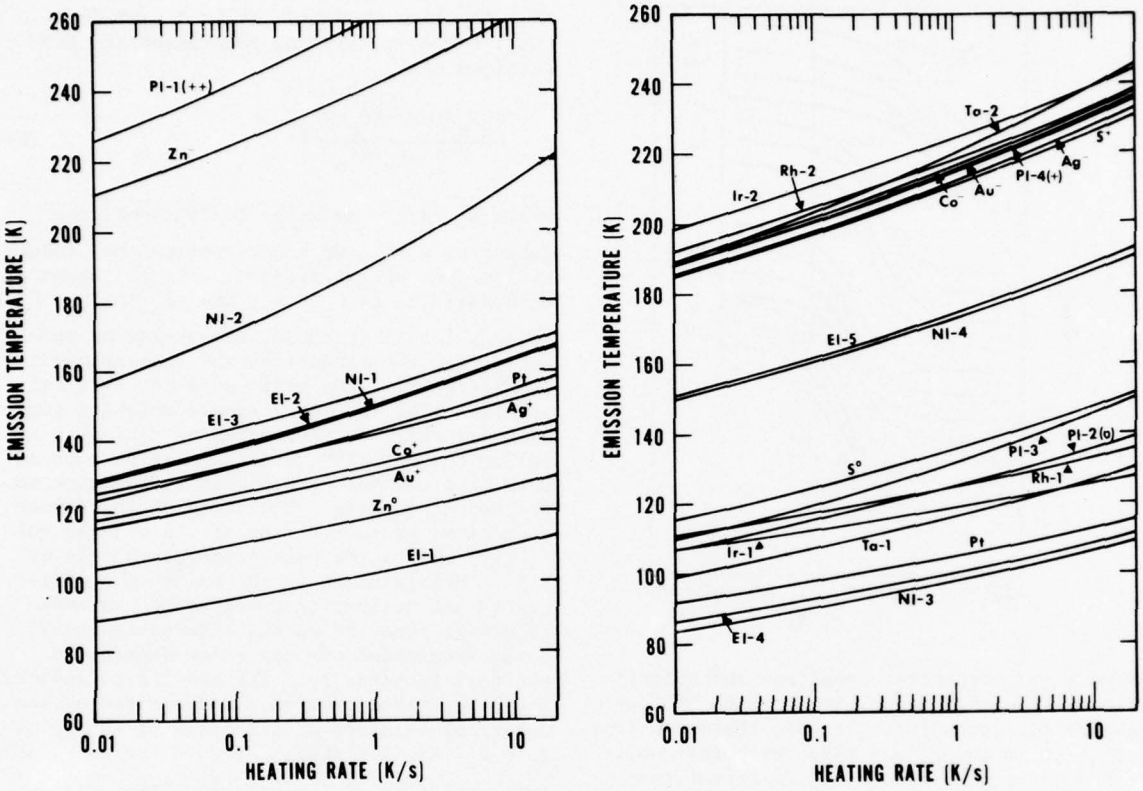

a. Hole emission in *p*-type silicon.

b. Electron emission in *n*-type silicon.

Figure 14. Temperature of peak value of thermally stimulated current response as a function of heating rate for selected defect centers in silicon. (See table 6 for identification of symbols.)

3.8. Extended Range MIS C-V Method

Design and evaluation work on the modified instrument for measuring capacitance, C, at applied voltages, V, of up to 10 kV (NBS Spec. Publ. 400-19, pp. 31-32) has been completed [53].

Detailed studies have been carried out on the influence of bias-protection circuitry on the accuracy of the capacitance measurement. It was found that with the three commercially available 1-MHz capacitance bridges tested (NBS Spec. Publ. 400-25, p. 28), the bias-protection circuitry introduces an error of less than 1.1 percent when measuring capacitances up to 130 pF.

A modified specimen holder and probe assembly were designed and constructed to permit the use of a guard ring around the electrode on the free surface of the sapphire. Use of an unguarded electrode resulted in a nonuniform electric field at the silicon surface in the region opposite the edge of the unguarded electrode. The total edge capacitance in the vicinity of the nonuniform electric field is on the order of a few percent. WWhile this is not important for the determination of the flat-band charge and silicon doping, it may introduce an undesirable error in a determination of the interface-state density.

The measurement technique has been extended to permit the measurement of the conductance, G, as a function of voltage. The results of measurements on two specimens indicate that there is reasonable agreement between the value for the density of interface states at the silicon-sapphire interface obtained from the peak value of the C-V characteristic at one point in the forbidden-band gap and the

Table 6 — Emission Coefficients and Activation Energies of Selected Defects in Silicon

Defect Center	Symbol	Emission Coefficient, $s^{-1} \cdot K^{-2}$	Activation Energy, eV	Source Reference
a. Centers Which Emit Holes in *p*-Type Silicon				
1 MeV electron induced	EI-1	1.53×10^{7}	0.239	[49]
Zinc	Zn^{0}	7.53×10^{7}	0.297	[48]
Gold	Au^{+}	2.70×10^{8}	0.345	[42]
Cobalt	Co^{+}	2.73×10^{8}	0.352	[41]
Silver	Ag^{+}	2.89×10^{8}	0.378	[45]
Platinum	Pt	1.77×10^{6}	0.320	[44]
1 MeV neutron induced	NI-1	2.2×10^{5}	0.311	[50]
1.5 MeV electron induced	EI-2	2.3×10^{5}	0.313	[50]
1 MeV electron induced	EI-3	2.63×10^{6}	0.354	[49]
1 MeV neutron induced	NI-2	17	0.281	[50]
Zinc	Zn^{-}	1.57×10^{6}	0.571	[48]
Process induced	PI-1(++)	3.06×10^{5}	0.585	[51]
b. Centers Which Emit Electrons in *n*-Type Silicon				
1 MeV neutron induced	NI-3	5.8×10^{5}	0.201	[50]
1.5 MeV electron induced	EI-4	1.75×10^{6}	0.216	[50]
Platinum	Pt	7.06×10^{7}	0.260	[44]
Tantalum	Ta-1	1.67×10^{5}	0.232	[47]
Iridium	Ir-1	4.22×10^{11}	0.385	[43]
Rhodium	Rh-1	2.85×10^{9}	0.353	[43]
Process induced	PI-2(0)	6.13×10^{5}	0.264	[51]
Process induced	PI-3	4.1×10^{3}	0.226	[50]
Sulfur	S^{0}	1.82×10^{5}	0.276	[46]
1 MeV neutron induced	NI-4	2.7×10^{6}	0.401	[50]
1.5 MeV electron induced	EI-5	1.54×10^{6}	0.397	[50]
Sulfur	S^{+}	1.14×10^{7}	0.528	[46]
Silver	Ag^{-}	3.34×10^{7}	0.544	[45]
Process induced	PI-4(+)	1.67×10^{7}	0.542	[51]
Gold	Au^{-}	1.97×10^{7}	0.547	[42]
Cobalt	Co^{-}	8.52×10^{6}	0.534	[41]
Rhodium	Rh-2	1.46×10^{8}	0.591	[43]
Iridium	Ir-2	4.3×10^{8}	0.629	[43]
Tantalum	Ta-2	1.63×10^{5}	0.472	[47]

corresponding value previously obtained from point-to-point differentiation of the C-V curve. (A. M. Goodman[x])

It is well known that e-gun aluminization of MOS devices produces positive charge at the silicon-oxide interface. The effect is presumably due to the generation of soft x-rays by the electron beam striking the melted aluminum. The charge is generally removed during a 400° to 500°C annealing step in a neutral or reducing atmosphere that follows the metallization.

It was found that a large positive charge develops at the silicon-sapphire interface during the e-gun aluminization and that conventional annealing at 400°C in forming gas does not entirely remove it. Further annealing does not help to remove the radiation induced charge and, in fact, increases the interfacial positive charge. This information has strong implications not only for current device processing but also for possible contemplated use of soft x-ray lithography in the fabrication of C-MOS/SOS devices and device arrays on sapphire.
(A. M. Goodman[x] and C. E. Weitzel[x])

The developed apparatus is useful for a variety of applications. The present ±10 kV capability of the system appears sufficient for all anticipated applications with the exception of the characterization of silicon-on-sapphire substrates thicker than 150 μm. For sapphire substrates 2 in. (51 mm) or more in diameter which are about 325 μm thick it would be necessary to have a higher bias voltage capability. Design considerations are now being given to develop a system which would allow characterization of thick sapphire substrates at applied voltage up to ±25 kV. This new system includes a linear-sweep high-voltage supply, high-voltage bias-protection circuitry, and a high-voltage specimen holding system. (A. M. Goodman[x])

---

[x]Work performed at RCA Laboratories under NBS Contract No. 5-35912. NBS contact for additional information: R. Y. Koyama.

4. MATERIALS CHARACTERIZATION BY PHYSICAL ANALYSIS METHODS

4.1. Optical Test for Surface Quality of Sapphire Substrates

Specular reflection measurements offer the possibility of providing useful information on both silicon and sapphire surfaces. The infrared surface analysis of sapphire (NBS Spec. Publs. 400-19, pp. 22-24, and 400-25, pp. 20-23) [54] is a useful means of detecting lattice-related damage, but is much less sensitive to surface scratch lines which may remain after the associated lattice damage is removed by substrate annealing. This is not surprising since the dimensions of these imperfections are much smaller than the infrared wavelength used, and scattering losses are relatively small. Thus, reflectance measurements at ultraviolet wavelengths comparable in magnitude with the dimensions of surface defects should be more effective in detecting surface irregularities. Similar considerations apply to epitaxial silicon films which, in turn, exhibit a surface texture related to the substrate surface condition and deposition parameters. Epitaxial silicon films are generally accepted or rejected on the product line in a subjective manner by visual inspection for light scattering effects or "haze." Films which exhibit haze appear to have inferior electrical properties; a fast, nondestructive, quantitative test is needed to place the screening on an objective basis.

An optical technique which measures the surface roughness of a reflective surface has been described by Bennett and Porteus [55]. This technique is based on published work on the reflection of radar waves from rough surfaces [56]. According to the theory presented in these publications, the reflectance of a surface is related to the root mean square roughness, σ, of a surface and to the root mean square slope of the profile of the surface, m. The complete expression is [55]

$$R = R_o\{\exp[-(\frac{4\rho\sigma}{\lambda})^2] + \frac{32\rho^4}{m^2}(\frac{\sigma}{\lambda})^4(\Delta\theta)^2\}, \qquad (7)$$

where R is the reflectance of a nonideal surface, R_o is the reflectance of an ideal surface (without roughness), λ is the wavelength of the incident radiation, and $\Delta\theta$ is an instrumental acceptance angle. The second term takes into account diffusely reflected light. If the reflectance measurement is made at wavelengths much longer than the root mean square surface roughness, the diffusely reflected component can be ignored and eq (7) becomes

$$\log R_o/R = [(4\rho\sigma)^2/2.303](1/\lambda^2). \qquad (8)$$

This technique requires that the surface be highly reflecting with R greater than about 40 percent. This requirement can be met by using a wavelength that is heavily absorbed. Since silicon is highly absorbing in the ultraviolet region of the spectrum, while sapphire is transparent, reflection measurements can be easily made on silicon-on-sapphire composites to evaluate the quality of the silicon.

Initial experiments were performed on four bulk silicon substrates which had been variously polished in order to introduce different degrees of surface roughness. The reflectance for each surface was measured as a function of wavelength and the ratio R_o/R at 240 and 280 nm was determined for each specimen; an aluminum mirror was used to determine R_o. The logarithm of this ratio is plotted against (on a logarithmic scale) the size of the polishing grit in figure 15. The values of σ to be used in eq (8) are not known but are related to the size of the polishing grit. Scanning electron micrographs show that surface roughness is related to the polishing grit size. It appears from these preliminary

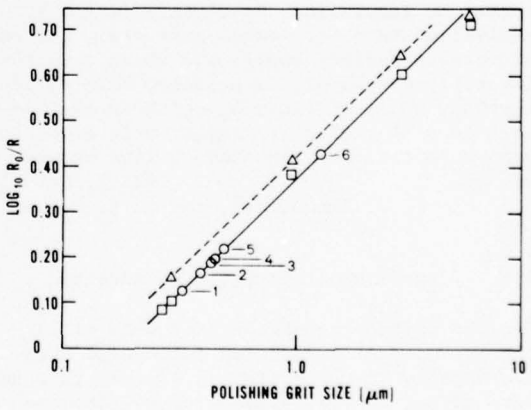

Figure 15. Specular reflection data for four bulk silicon substrates polished with different polishing grits and for six silicon-on-sapphire composites. (Δ: bulk silicon at 240 nm; □: bulk silicon at 280 nm; ○: silicon-on-sapphire at 280 nm.)

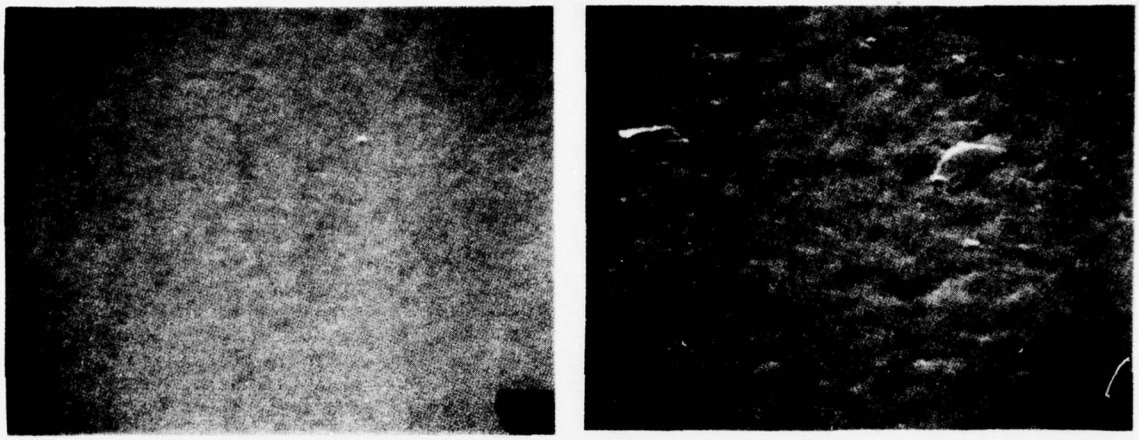

a. Acceptable quality. Magnification: ∿600x. b. Rejected specimen. Magnification: ∿600x.

Figure 16. Scanning electron micrographs of silicon-on-sapphire surfaces.

results that this plot may be used as a reference curve for determining silicon surface roughness on this scale and at these wavelengths.

On this basis, reflection data were obtained at 280 nm on six silicon-on-sapphire composites. These results are also plotted in figure 15; in this case the point for each specimen is placed on the 280-nm line at the measured value of reflectance. The horizontal position, then, should give some indication of the surface roughness. Scanning electron micrographs of two typical specimens are presented in figure 16. Specimen 1, which is equivalent to a very small grit size, had an acceptable surface smoothness which compares favorably with a highly polished bulk silicon surface, while specimen 4, which is equivalent to a significantly larger grit size, had been rejected from the product line because of haze. (M. T. Duffy*, P. J. Zanzucchi*, and G. W. Cullen*)

4.2. Impurities in Sapphire Substrates

Besides surface roughness (see sec. 4.1.), the presence of impurities introduced unintentionally in the epitaxial silicon film can also affect the performance of silicon-on-sapphire devices. One potential source of these undesired impurities is the polished sapphire substrate. In order to determine the typical impurity levels in commercially available polished sapphire substrates, three substrates from different sources were characterized by neutron activation analysis.†

Two specimens cut from half of each of the circular polished sapphire slices, one near the center and one near the edge, were weighed, sealed in polyethylene, and irradiated in a neutron flux of 6×10^{13} $cm^{-2} \cdot s^{-1}$ for 30 min in the NBS reactor. After a cooling period of about 30 min, the specimens were cleaned with a 50-percent hot nitric acid solution to remove possible external contamination. The specimens were then counted using a Ge(Li) detector-multichannel analyzer system. Calcium was determined 30 min after irradiation and manganese was determined 120 min after irradiation. Standards were aqueous solutions of the two elements.

Subsequently, the specimens were again irradiated, this time for 10 h. After a cooling period of about 10 days to eliminate ^{24}Na matrix activity, the specimens were counted to determine the amounts of molybdenum, chromium, antimony, scandium, iron, cobalt, and zinc which were present. This counting was also

*Work performed at RCA Laboratories under NBS Contract No. 5-35915. NBS contact for additional technical information: K. F. Galloway.

†The substrates were supplied by Rockwell International Corporation which had obtained them from various sources for evaluation under Air Force Contract F19628-75-C-0108.

Table 7 — Elemental Content of Sapphire Substrates

Element	Concentrations of Element, ppb (by weight)					
	Substrate 1		Substrate 2		Substrate 3	
	Center	Edge	Center	Edge	Center	Edge
Molybednum	1000	1000	<10	<10	400	400
Chromium	100	100			∿10	40
Antimony	0.2	0.2	4	3	1	2
Scandium	0.1	0.1	0.1	0.1	0.3	0.02
Iron	70	60	300	300	60	60
Cobalt	0.1	0.1	0.1	0.1	0.1	0.1
Manganese	0.5	0.5	1	1	0.5	0.5
Calcium	<10000	<10000	<10000	<10000	<10000	<10000
Zinc	<10	<10	<10	<10	<10	<10

done with the Ge(Li) system. Standards for all elements were either aqueous solutions or small amounts of metal foils dissolved and aliquoted after irradiation.

The results are presented in table 7. The chromium content of substrate 2 could not be determined because it contained a small amount of iridium which interfered with this determination. (S. Mayo and G. J. Lutz[§])

4.3. Electron Spectroscopy Techniques

Effect of Ion Flux Distribution on Depth Resolution in Auger/Ion Beam Profiling of Oxide-Silicon Structures — As a result of an electrical breakdown and attempts to repair the ion gun in the Auger spectrometer, the depth resolution was seriously deteriorated. This was manifested by an apparent widening of the oxide-silicon interface in a previously measured specimen, and also by a large scattering in the data. In order to clarify the source of the deterioration, the flux distribution in the primary ion beam was measured for typical operating conditions.

Consider the experimental conditions outlined in figure 17. The specimen surface, S, is positioned at the focal point, F, of the cylindrical mirror analyzer, CMA, with its normal at an angle $\theta \approx 30$ deg with respect to the primary electron beam, EB. The ion beam, IB, is incident on the surface at an angle η and is carefully aligned so that it strikes the specimen at the focal point, as depicted in the figure. The ion current (flux) distribution at the specimen surface is also shown in the figure; the electron beam is considered infinitesimally narrow since it is much smaller than the ion beam. During the alignment procedure there is a finite possibility of displacing the specimen along the z (CMA) axis. The broken lines and curves show how the ion and electron beams are displaced. Notice that in this case the electron beam strikes the wall of the ion sputtered crater in the specimen. A similar situation arises when the ion beam is not perfectly aligned and hits off the focal point of the CMA, or if a shift occurs in the ion beam alignment during sputtering. The latter effect may result from thermal drift in the ion optics, particularly when the total sputtering time is long (hours).

It can be shown that the fractional change in apparent interface width is equal to the fractional change in ion flux density provided that fluctuations in sputtering yield and specimen density can be neglected [57]. To demonstrate the importance of reducing flux inhomogeneities to a minimum, a 100-nm thick oxide thermally grown on a (100) silicon surface was profiled using two ion guns,

[§]NBS Activation Analysis Section, Analytical Chemistry Division.

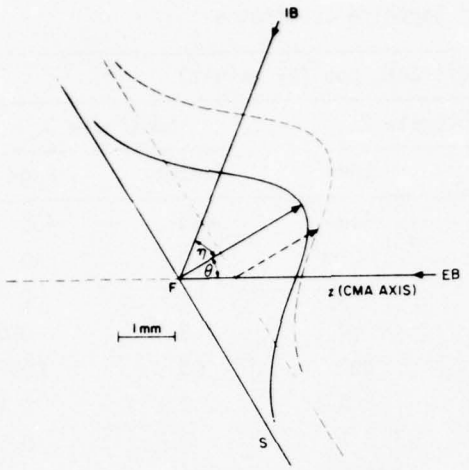

Figure 17. Schematic of experimental conditions for ion sputter etching and Auger electron spectroscopy. (Note that the angles θ and η are not in the same plane.)

one normal and one with a defect in the optics. With the former the observed width of the oxide-silicon interface was 4.3±0.3 nm. With the defective gun there was a large scatter in the observed width but the average of the minimum width was about 6 nm.

The spatial distribution of the ion beam current in the two guns was measured by moving a square Faraday cup 250 μm on a side, along the z-axis. The results are plotted in figure 18 as ion flux density normalized to its value at the CMA focus (z=0). Both stationary and rastered beams were measured; the additional broadening of an interface at a depth of 100 nm, due to the flux inhomogeneities in the rastered beams are shown in figure 19. The predicted broadening is consistent with the experimental results described above. Note that in figure 19 there is a region of zero broadening for the normal gun if the specimen is located about 0.4 mm behind the CMA focus. This occurs as a result of the flat distribution of the normal rastered ion beam in this region (see fig. 18a).

These results show that in Auger/ion depth profiling it is of critical importance to check routinely the ion current distribution and to apply a suitable rastering with compensation for small displacements of the rastered beam with respect to the focal point of the CMA. In most of the depth profiling work reported in the literature neither of these measures is taken. It is, therefore, reasonable to conclude that flux inhomogeneities have been a limiting factor in the depth resolution [58] and that interface broadening larger than several nanometers can occur. Such effects have probably been important in producing the idea that the depth resolution in sputter milling is 5 or 10 percent of the

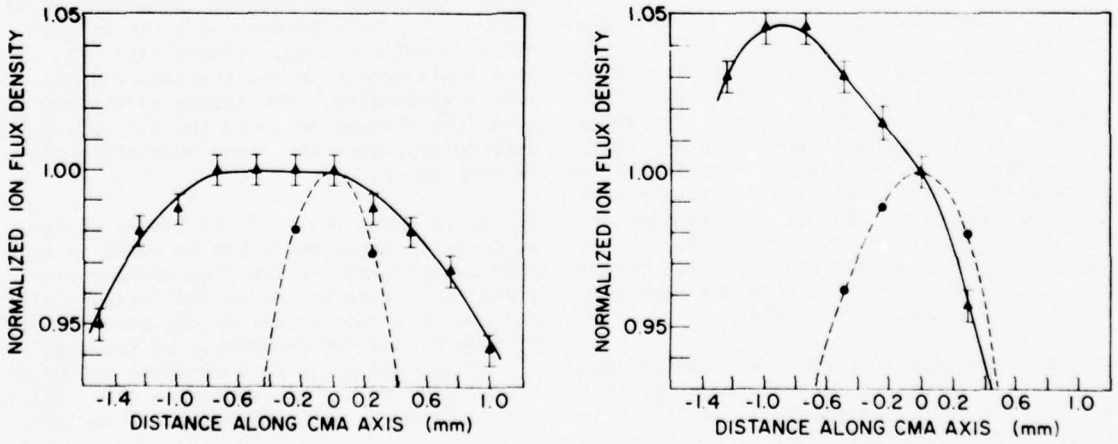

a. Normal gun.

b. Defective gun.

Figure 18. Spatial distributions of ion beam current. (●: stationary beam directed at CMA focal point (z=0); ▲: rastered beam with ion current at z=0 reduced to one-half of its stationary value.)

total depth milled. The present work shows that this is not the case if proper techniques are used. (J. S. Johannessen[¶#], W. E. Spicer[¶], and Y. E. Strausser[×])

Interface Broadening by Electron Stimulated Desorption — Another important parameter in Auger analysis and in Auger/ion depth profiling is the primary electron fluence. To demonstrate the adverse effect of a high primary electron current density on depth reslution, the interface profile of the oxide film described above was measured with a 5-μA primary electron beam. In one case the beam was held stationary; in the other case it was rastered over an area 250 μm by 250 μm. The defective ion gun was used to obtain both profiles. The two 502-eV O_{KLL} profiles are shown in figure 20. The horizontal axis is based on the sputter rate associated with the ion beam and the sputtering time. The interface appears to be significantly wider when measured with the stationary electron beam. The early reduction in the measured oxygen density occurs because the sputtering rate in the area where the specimen is exposed to both ions and electrons is greatly enhanced [59] as illustrated in the inset of the figure. As a result the electron beam reaches the interface ahead of the main portion of the sputtered crater. The reason for the enhanced sputtering rate is probably due to electron stimulated desorption of oxygen. The enhancement of the sputtering rate is not uniform across the area of the electron beam; therefore, the measured oxygen density decreases gradually until the main portion of the sputtered crater reaches the interface. (J. S. Johannessen[¶#] and W. E. Spicer[¶])

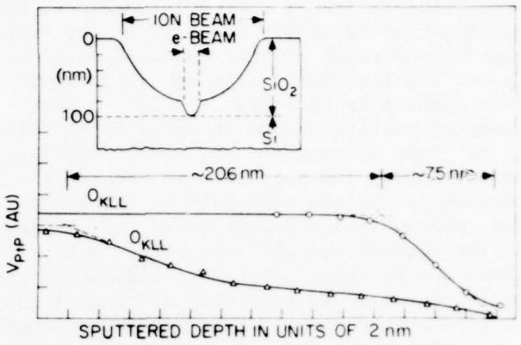

Figure 20. Oxygen KLL profiles showing effects of electron-beam enhancement of sputtering rate. (Δ: stationary electron beam; o: rastered electron beam; the inset shows the sputtered crater profile for the case of a stationary electron beam.)

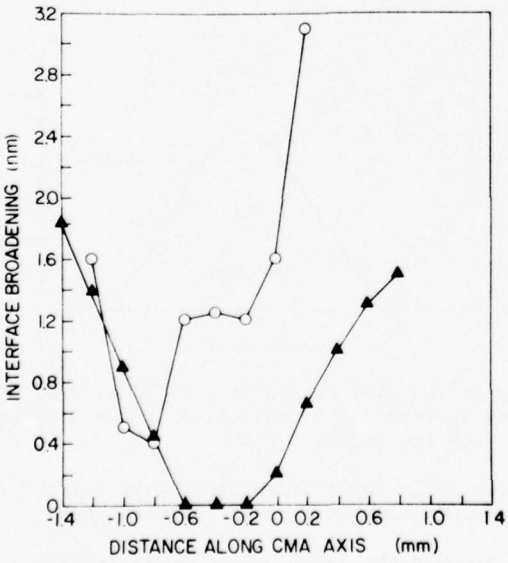

Figure 19. Additional broadening of an interface at a depth of 100 nm due to flux inhomogeneity in rastered ion beams of normal (▲) and defective (O) ion guns.

Crater Edge Profiling — The crater edge formed by appropriate ion beam etching provides a beveled surface analogous to that produced by more usual mechanical lapping [60]; however, the angle can be usefully reduced by three orders of magnitude, allowing much greater spatial resolution. The very shallow angle is made possible by the well controlled and chosen parameters of the ion beam and practical by the shallow analysis depth (~1 nm) of Auger electron spectroscopy. To carry out a crater edge profile analysis

---

[¶]Work performed at Stanford Electronics Laboratories of Stanford University under NBS Contract No. 5-35944. NBS contact for additional information: K. F. Galloway.

[#]Partially supported by Electronics Research Laboratory, University of Trondheim and the Royal Norwegian Council for Scientific and Industrial Research.

[×]Work performed at the Surface Analysis Laboratory of Varian Vacuum Division under subcontract to Stanford University.

of an oxide-silicon (or other) interface, the electron beam is slowly swept in a line scan across the portion of the crater edge which exposes the interface. The Auger spectrum of an element is recorded. In this manner elemental profile shapes essentially identical to those of conventional depth profiling are obtained. The abscissa now becomes the position of the electron beam on the crater edge, which, from a knowledge of the ion beam current density and the associated sputter rates, can be transformed to a distance normal to the specimen surface. Although a number of elements can be recorded simultaneously by using a multiplexer, repetitive scans can be made across the interface, so there is no absolute need to multiplex.

This procedure was tested by carrying out experiments on specimens with 50- to 150-nm thick oxides thermally grown on phosphorus-doped silicon [61]. The experimental geometry is shown in figure 21a; the rastered 1-keV ion beam (current density ≈ 40 μA/cm^2) formed an approximately elliptical crater as shown in figure 21b. The ion beam current density as measured along the x-direction through the focal point of the analyzer by using a small Faraday cup is shown in figure 21c.

In an experiment to compare conventional depth profiling with crater edge profiling the specimen was depth profiled to the interface as determined by monitoring oxygen, and then for an additional time equal to 20 percent of the time that it took to reach the interface. The additional sputtering time was chosen such that the position of the interface was along a relatively linear part of the ion current density distribution of figure 21c. The width of the crater at the interface along the x-direction should then be given by the width of the current density distribution at five-sixths of maximum. This was checked and the widths were found to be identical within the experimental error of 0.1 mm, giving confidence that the slope of the crater wall may also be obtained from the slope of the current density distribution provided that the sputtering rate is known and that it remains unchanged across the interface.

Line scans for oxygen, phosphorus, and elemental silicon were made along a 530-μm length of the crater edge which included the oxide-silicon interface (C to C^1 in fig. 21b). The results are shown in figure 22. From the slopes of the oxygen curve and the crater wall (fig. 21c) the interface width was found to be 5.0 ± 0.2 nm as compared with the value of 4.9 ± 0.2 nm obtained from the initial depth profile. Of chief significance, however, is the relative ease with which the measurement could be repeated.

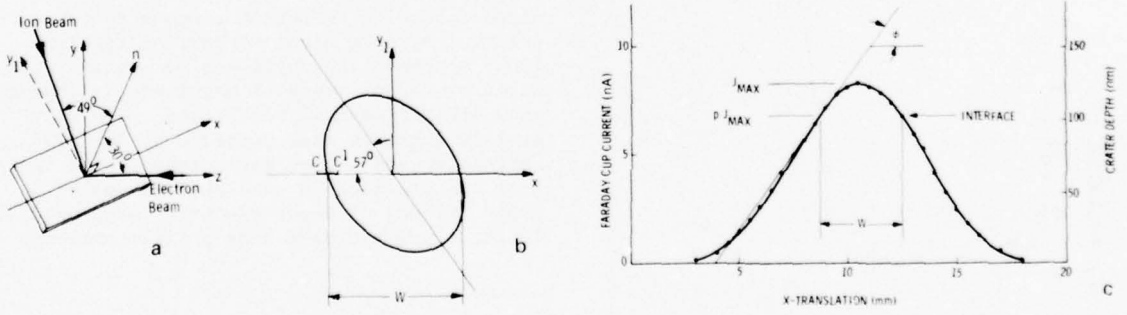

a. Orientation of electron and ion beams relative to the specimen normal, n. The axis, y_1, is the projection of the y-axis on the specimen surface. The projection of the ion beam on the specimen surface is at an angle 57 deg from the x-axis.

b. Ion-beam crater in the plane of the specimen surface. The ellipse represents exposed interface; to obtain the profile, a line scan is made along the x-axis between C and C^1.

c. Ion current density measured along the x-axis through the focal point of the cylindrical mirror analyzer (z=0). The interface occurs at a position equal to five-sixths of the crater depth.

Figure 21. Geometry for crater-edge profiling using Auger electron spectroscopy.

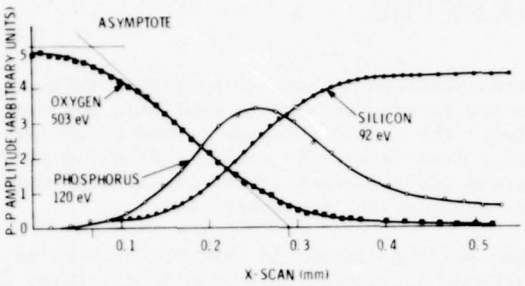

Figure 22. Line scans for oxygen, phosphorus, and elemental silicon across the interface between the points C and C^1 on the x-axis.

The crater edge interface analysis technique can be used as an adjunct to the conventional technique but in many cases it can be used quite independently since the positioning of the electron beam during sputtering is much less critical when the monitoring of Auger peaks is mainly to determine the time to an interface. In many cases the sputtering may be rapid and fears of bulldozing too rapidly through the interface are no longer important, since the sputtering and analysis are now separated. When there is difficulty in measuring details of the ion beam shape, the slope at an interface can be calibrated by making a good conventional depth profile from which the interface width can be measured. Obviously not all interface analysis lends itself to this technique since in a macroscopic sense the films must be uniform, parallel to the surface over a distance of a few millimeters. However, films of this degree of uniformity are not uncommon.

(N. J. Taylor[×], J. S. Johannessen[¶#], and W. E. Spicer[¶])

[¶]Work performed at Stanford Electronics Laboratories of Stanford University under NBS Contract No. 5-35944. NBS contact for additional information: K. F. Galloway.

[#]Partially supported by Electronics Research Laboratory, University of Trondheim and the Royal Norwegian Council for Scientific and Industrial Research.

[×]Work performed at the Surface Analysis Laboratory of Varian Vacuum Division under subcontract to Stanford University.

5. MATERIALS AND PROCEDURES FOR WAFER PROCESSING

5.1. Sodium Contamination in Oxidation Furnaces*

Additional experiments verified the previous conclusion (NBS Spec. Publ. 400-25, pp. 29-30) that despite its great sensitivity for free sodium, the resonance fluorescence method [62] is not adequate to detect sodium contamination in furnace tube atmospheres at 1000°C which produce oxide films with sodium contamination of the order of 10^{11} cm^{-2}.

To investigate the relationship between free sodium density and the density of sodium compounds, thermodynamic calculations were made to determine the equilibrium partial pressures of various species at 1300 K in oxygen flowing at 4 cm^3/s. It was assumed that the source of sodium was the contamination in the fused silica tube wall which generally has an average sodium content of about 10 ppm by weight [63]. Because of errors and approximations in thermodynamic data involved in these equilibrium calculations an absolute error of ±50 percent could be expected, although the relative error of these results is believed to be much smaller.

The results of these calculations [64] are summarized in table 8 which lists both partial pressures, P, of appropriate compounds and density of sodium, N, for several levels of water content in the oxidation atmosphere. For dry oxygen, free sodium is the predominant species but as water vapor is added the total sodium density increases significantly because of the formation of sodium hydroxide. The effect of the added water vapor is illustrated in figure 23 which also includes the results of calculations made for 1200 and 1400 K.

Calculations were also made to establish the effect of cleaning the furnace tube walls with hydrogen chloride or chlorine. The results of these calculations for the case of a 10-percent mixture of hydrogen chloride or chlorine in an inert carrier gas at atmospheric pressure are summarized in table 9. The calculations indicate a pressure of NaCl higher than the vapor pressure for NaCl(liq), but under the actual conditions, equilibrium is probably not reached. Micro-droplets of liquid sodium chloride, if formed on the tube wall hot zone, would be removed by the gas stream and transported to a cooler tube zone where sodium chloride precipitates on the wall (sodium chloride melts at 801°C). This "transpiration mechanism" continues while sodium in the hot zone is available for reaction. The sodium chloride formed in the gas phase also is carried down the flushing gas stream and condenses at the cooler zone where the temperature is appropriate.

The cleaning action can thus be interpreted in terms of relocating sodium in the tube, depleting the hot zone and enriching the exhaust tube end where the wall temperature is appropriate for condensation. Assuming that the oxidation tube wall surface is about 4000 cm^2 and that the reaction depth in the wall is 10^{-3} cm, the total reacting volume is 4 cm^3 or about 10 g of fused silica, which at a 10-ppm sodium content in the fused silica is equivalent to 0.1 mg of sodium which requires the use of only 0.15 mg of chlorine or hydrogen chloride for complete reaction equilibrium.

At a typical flow rate of 4 cm^3/s (0.5 scf/h), this quantity of chlorine or hydrogen chloride is transported through the oxidation tube in about 1/2 s. Thus the reaction rate is regulated by diffusion of sodium in the fused silica. When sodium in the wall bulk diffuses to the wall surface, the reaction with chlorine effectively takes place immediately. In practice, a cleaning period of about 20 h is generally used to deplete the tube wall. The longer the cleaning period, the longer the oxidation tube can later be operated under acceptable oxide growing conditions. (S. Mayo and W. H. Evans[+])

5.2. X-Ray Dose in Electron-Beam Evaporators*

Additional calculations were made to estimate the x-ray dose received by the oxide films in MOS structures with aluminum or chromium gate electrodes deposited by electron-beam evaporation [40]. Results of a preliminary experiment (NBS Spec. Publ. 400-17, pp. 20-21) suggested that an absorbed dose of the order of 1 kGy (0.1 Mrads(SiO_2)) is received during the evaporation of a 1-μm thick aluminum film over silicon dioxide with 10-keV electrons.

---

*Principally funded by the Defense Nuclear Agency.

[+]NBS Chemical Process Data Evaluation Section, Physical Chemistry Division.

Table 8 — Equilibrium Partial Pressures and Sodium Densities in Fused Silica Oxidation Tubes at 1300 K as a Function of Water Content in Flowing Oxygen

Water Content, ppm:	0		1		30	
Compound	P, atm	N, cm^{-3}	P, atm	N, cm^{-3}	P, atm	N, cm^{-3}
Na	2.5×10^{-12}	1.4×10^{7}	2.5×10^{-12}	1.4×10^{7}	2.5×10^{-12}	1.4×10^{7}
NaO	9.1×10^{-13}	5.2×10^{6}	9.1×10^{-13}	5.2×10^{6}	9.1×10^{-13}	5.2×10^{6}
Na_2O	2×10^{-24}	—	2×10^{-24}	—	2×10^{-24}	—
NaOH	—	—	8.6×10^{-11}	4.9×10^{8}	6.1×10^{-10}	3.5×10^{9}
$Na_2(OH)$	—	—	3.7×10^{-20}	—	1.1×10^{-18}	—
Total Sodium	3.4×10^{-12}	1.9×10^{7}	8.9×10^{-11}	5.1×10^{8}	6.1×10^{-10}	3.5×10^{9}

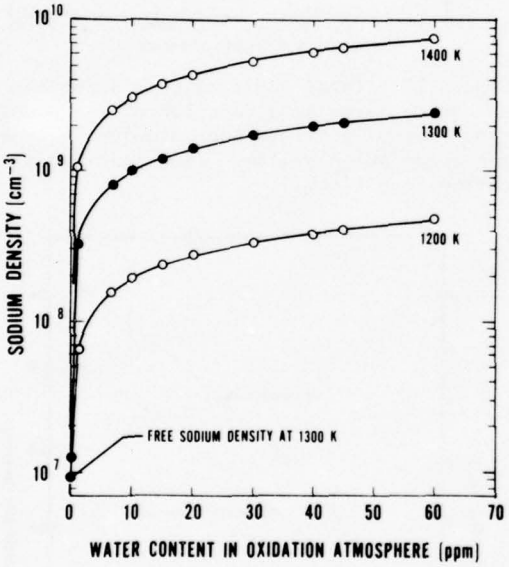

Figure 23. Sodium density in the atmosphere of a fused silica oxidation tube as a function of water vapor content at temperatures from 1200 to 1400 K.

Table 9 — Equilibrium Partial Pressures and Sodium Densities in Tubes at 1300 K With an Atmosphere of 10% Hydrogen Chloride or Chlorine in an Inert Carrier Gas

Compound	10% HCl		10% Cl_2	
	P, atm	N, cm^{-3}	P, atm	N, cm^{-3}
NaCl	5.5×10^{-3}	3.1×10^{16}	1.4×10^{-2}	7.9×10^{16}
Na_2Cl_2	8.2×10^{-4}	9.3×10^{15}	5.4×10^{-3}	6×10^{16}
H_2O	3.6×10^{-3}			
O_2			6.3×10^{-3}	

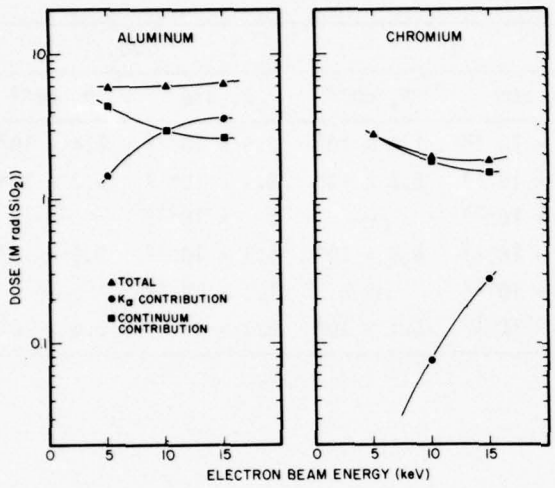

Figure 24. Total ionizing dose deposited in the oxide layer as a function of electron-beam energy during the electron-gun evaporation of aluminum and chromium. (See text for evaporation conditions.)

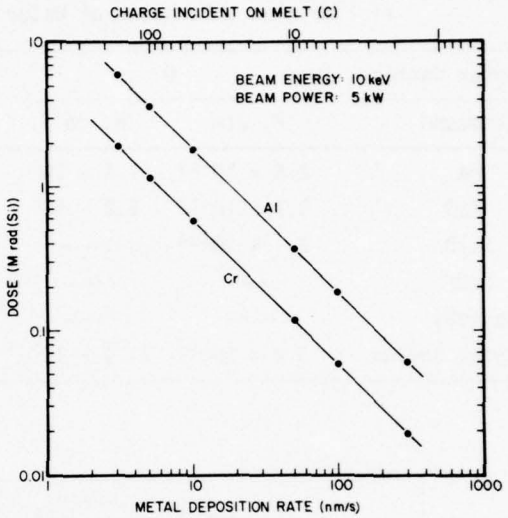

Figure 25. Total ionizing dose deposited in the oxide layer as a function of the deposition rate of aluminum and chromium in an e-gun evaporation system. (See text for evaporation conditions.)

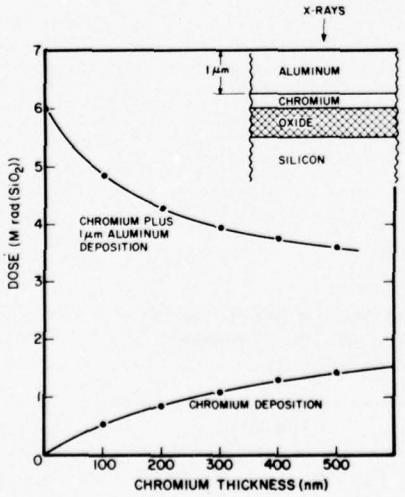

Figure 26. Total ionizing dose deposited in the oxide layer as a function of chromium layer thickness during the e-gun evaporation of chromium or of a 1-μm thick aluminum layer over chromium. (See text for evaporation conditions.)

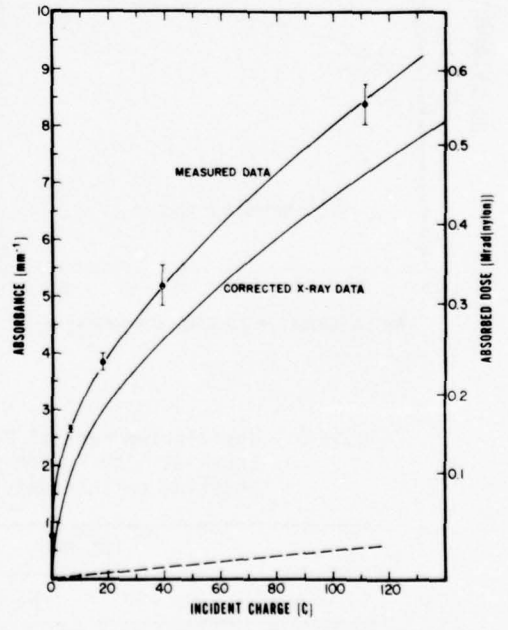

Figure 27. Absorbance of x-ray energy in nylon film dosimeter as a function of the electron charge incident on aluminum in an e-gun evaporator. (Solid points are measured values, dashed curve is the signal due to optical radiation, solid curve is the corrected x-ray dose.)

The results of calculations of absorbed dose as a function of electron-beam energy are shown in figure 24. The calculations were made for the case of the deposition of aluminum or chromium metallization on a 50-mm diameter silicon wafer covered with a 100-nm thick layer of silicon dioxide and located about 500 mm from the melt. The wafer subtends a solid angle of 0.01 sr. For each energy, the beam current was taken as the value necessary to maintain the beam power at 5 kW. A typical deposition rate of 3 nm/s was assumed and the process was continued for 333 s in order to deposit 1 μm of metal.

With this set of parameters, the absorbed radiation dose in the oxide due to both K_α and and bremsstrahlung radiation was calculated as a function of beam energy. In the range 5 to 15 keV the absorbed dose was found to be essentially independent of energy; approximately 60 kGy (6 Mrads(SiO_2)) was absorbed in the oxide film for aluminum evaporation and approximately 20 kGy (2 Mrads(SiO_2)) for chromium evaporation. It should be noted that no significant dose reduction can be expected during aluminum evaporation by operating the electron gun at energies below 1.5 keV, where the aluminum K_α x-ray is not excited, because of the increase in the bremsstrahlung radiation at low energies.

To evaluate the shielding effect of the metal film, the x-ray dose in the oxide was evaluated under the assumption that the metal absorbed no energy. At a beam energy of 10 keV the aluminum film was found to reduce the absorbed dose in the oxide by a factor of 1.7 while the chromium film was found to reduce it by a factor of 3.9. The calculation of energy deposited per unit thickness of oxide indicated that the dose is essentially uniformly distributed throughout the oxide, being only approximately 10 percent higher at the metal-oxide interface than at the oxide-silicon interface.

The effect of absorbed dose on the metal deposition rate was calculated for several beam energies. The radiation dose for depositing 1 μm of metal as a function of deposition rate is given for a beam energy of 10 keV and a beam current of 0.5 A in figure 25; the results of calculations at other beam energies were similar.

These calculations are based on the assumption of the deposition of equal thicknesses of aluminum and chromium for comparison. However, in actual practice, a chromium gate layer of 100 to 300 nm would probably have about 1 μm of aluminum deposited over it. Assuming the depositions are carried out with a 10-keV electron beam at 0.5 A yielding a deposition rate of 2 nm/s, figure 26 illustrates both the dose absorbed in the oxide as a function of chromium thickness and the dose absorbed in the oxide with a 1-μm thick aluminum layer deposited over the chromium layer of thickness as shown on the abscissa. The shielding effect of the chromium is clearly illustrated.

The discrepancy between the results of these calculations and the preliminary experimental results is thought to arise from the sensitivity of the thermoluminescent dosimeters (TLDs) used to measure the absorbed dose to *in-situ* annealing effects caused by optical radiation and thermal effects due to the kinetic and condensation energies of the metal film being deposited. A temperature rise during irradiation causes a well known glow peak indicative of release of trapped electrons. The net reading after irradiation of TLDs in contact with a silicon wafer therefore corresponds to only a fraction of the actual dose deposited.

Therefore to test the accuracy of the calculations, a second experiment was performed in which polychlorostyrene and nylon film dosimeters, 50 and 60 μm thick respectively, were used to measure the x-radiation produced in the electron-beam evaporator. These films were exposed at the normal wafer location in the evaporator while a 10-keV electron beam impinged on aluminum. The beam intensity was reduced to 0.04 A while the crucible containing the metal was cooled to prevent any aluminum evaporation. Under these conditions, an x-ray exposure equivalent to that obtained in a typical metal deposition is obtained provided the total number of electrons (or total charge) incident on the metal is equivalent to that during metal deposition. Two groups of nine 1-cm^2 polychlorostyrene and nylon films were exposed in pairs to increasing x-ray doses. Figure 27 shows the measured nylon film absorbance as a function of total electron charge incident on the metal. The measured absorbance must be corrected to account for the sensitivity of the film to optical radiation which is present in the evaporator chamber during metallization. The figure also shows the correction factor and the corrected results for nylon films. Similar results were obtained for the polychlorostyrene films which, however, required no correction for optical sensitivity.

The dose absorbed in the dyed films when a 10-keV electron beam deposits 100 C in aluminum was calculated. This charge incident on the metal at an appropriate current is typical of that necessary to deposit 1 μm of aluminum at a rate of about 3 nm/s. The calculations yielded an absorbed dose of 3.9 kGy (0.39 Mrads(nylon)) and 4.5 kGy (0.45 Mrads (poly)) in the nylon and polystyrene films, respectively. This compares reasonably well with the experimentally measured values of 4.3 kGy (0.43 Mrads(nylon)) and 3.0 kGy (0.30 Mrads(poly)) and provides the basis for the deposited dose calculations in silicon dioxide films during the metallization process. Discrepancies can be explained in terms of errors introduced by the extrapolation of the aluminum bremsstrahlung below 2 keV.

The trends in x-ray dose due to the electron-beam metallization process illustrated by these calculations can be used in examining experimental results on device hardness. The deposition of chromium results in reduced dose when compared to aluminum deposited under equivalent evaporation conditions. However, since chromium sublimates, less electron beam injection power is necessary to deposit a chromium layer of the same thickness as an aluminum layer. This can result in a significant reduction in dose absorbed in the oxide. Several experimenters have noted that MOS devices fabricated with electron-beam evaporated chromium gates exhibit a higher degree of radiation resistance than devices fabricated with aluminum gates [65-68]. Gates formed by depositing aluminum over chromium result in a reduced x-ray dose in the oxide when compared to gates formed only of aluminum as illustrated in figure 26.

An attempt to reduce the electron-gun damage in the fabrication of aluminum gates by reducing the electron-gun beam energy to about 3 keV and reducing the deposition time to about 20 s has been reported [69]. The authors concluded that even under these conditions considerable damage to the oxide occurred. Figure 24 illustrates that reducing the electron-beam energy does not reduce the x-ray dose absorbed in the oxide; however, figure 25 indicates that reducing the evaporation time (increasing the deposition rate) can reduce the oxide dose.

(S. Mayo, K. F. Galloway, and T. F. Leedy)

5.3. Ion Implantation Parameters

This task is concerned with the development of methods for measuring critical parameters associated with ion implantation. Study of Schottky barriers for use in measuring implanted profiles by the capacitance-voltage (C-V) technique was extended to the case of phosphorus-implanted silicon. As part of a comprehensive study of methodology for dose measurement, the characteristics of various current integrators were investigated.

Schottky-Barrier Capacitance-Voltage Technique — The four metallization systems, aluminum, gold, titanium-gold, and molybdenum-gold, previously studied on boron-implanted silicon (NBS Spec. Publ. 400-25, pp. 31-32), were studied on cleaned, natural (unetched) surfaces. Gold consistently yielded rectifying current-voltage (I-V) characteristics, stable C-V profiles, and barrier capacitance in the range 200 to 400 pF/mm^2. Results with aluminum were mixed; some barriers yielded fairly rectifying I-V characteristics, satisfactory but slightly unstable C-V profiles, and barrier capacitance in the range 200 to 300 pF/mm^2 while others yielded non-rectifying I-V characteristics, unstable C-V profiles, and barrier capacitance in the range 2000 to 3000 pF/mm^2. Molybdenum-gold yielded poorly rectifying I-V characteristics, barrier capacitance of the order of 1600 pF/mm^2, and C-V profiles which were only occasionally satisfactory. Titanium-gold yielded resistive I-V characteristics, barrier capacitances in the range 1000 to 5000 pF/mm^2, and no C-V curves.

The quality of the I-V characteristic and the value of the barrier capacitance are good indicators to determine whether the C-V curve is going to be good or bad. For satisfactory C-V profiles, the I-V characteristics should be at least fairly rectifying and the barrier capacitance should be in the range from 200 to 400 pF/mm^2. It was found that the metal film thickness should be about 100 nm; films less than 50 nm or more than 200 nm thick were likely to yield poor or time-dependent C-V curves. In the case of silicon implanted with phosphorus, gold is the preferred metallization material.

Dose Measurement Technology — Measurement of the ion beam current density and integration of the beam current for dose measurement are important parts of the implantation process and must be done before as well as during implantation. Figure 28 shows a typical target configuration for characterizing the ion beam before beginning an implantation step. The suppressor electrode is maintained at a slightly negative potential with respect to the target collector in order to reduce er-

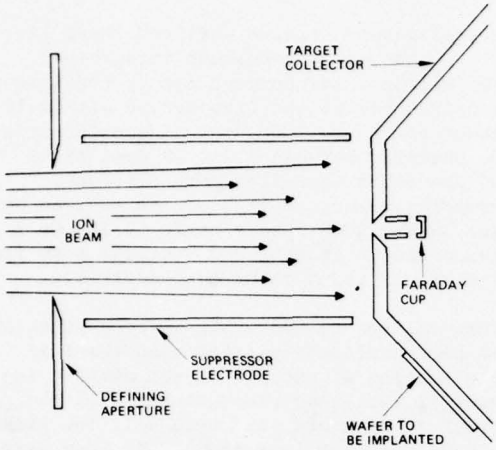

Figure 28. Typical target configuration for characterizing the ion beam before ion implantation.

rors in current measurement which would result from the emission of secondary electrons for the target collector. The dimensions and spacing of the various electrodes can be changed to provide for differences in target area.

In order to obtain a uniform ion current over large areas, the beam must be scanned in both vertical and horizontal directions or the target must be scanned mechanically. The ratio of scanning frequencies is usually such that a series of high frequency pulses is superimposed on a series of low frequency pulses. . Since the area of the ion beam itself is much smaller than the area of the circular defining aperture, this type of scanning produces a square pattern over the aperture as shown in the inset of figure 29. The ratio of the area of the circular defining aperture, $\pi d^2/4$, to the area covered by the beam scan, D^2, which is known as the overscan efficiency, is a measure of the utilization of the ion beam. As shown in figure 29, this is about 80 percent for the case where the scanned area fills the entire circular aperture (D=d) and drops to less than 10 percent when the beam is overscanned one full target diameter on each side of the aperture (D=3d), a condition necessary if the beam shape is badly distorted.

During the set-up procedure, the Faraday cup current (see fig. 28) can be compared with the total target collector current to determine when the current density is equal in the two areas. Typical plots of the two current

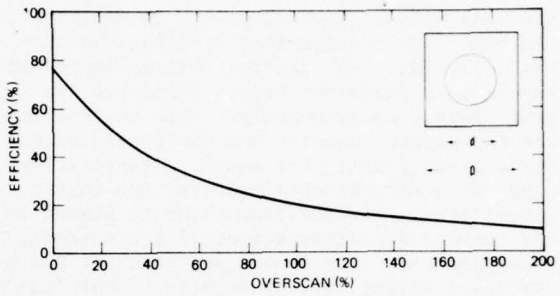

Figure 29. Scanning geometry and overscan efficiency. (Overscan (%) = $[(D/d)-1] \times 100$; overscan efficiency (%) = $(\pi d^2/4D^2) \times 100$.)

densities are shown in figure 30. With no scanning voltage applied, the steady-state ion beam is centered on the cup and shows a relatively high reading depending on how well the beam can be focused. As the scanner voltage is increased, the beam starts to move back and forth across the cup, resulting in a series of pulses which are averaged by the current measuring instrument (an electrometer, for example). The target collector current measured by a current integrator remains essentially the same, increasing slightly as less current is collected by the cup, until

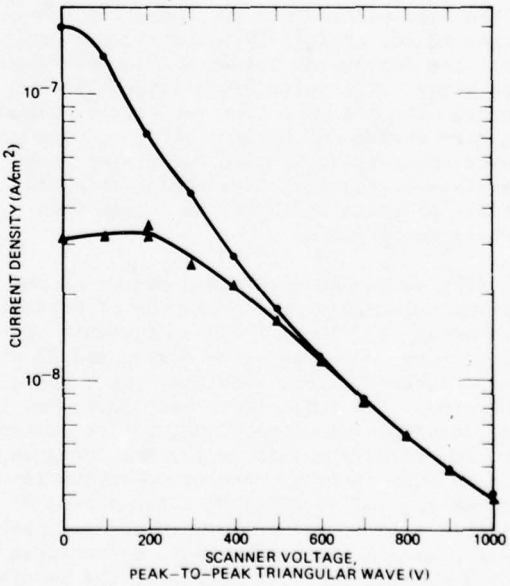

Figure 30. Target current densities as a function of scanner voltage for an 84-keV boron ion beam. (●: collector cup current; ▲: total target current.)

the scan voltage is high enough to deflect the beam past the aperture defining the target collector area. As the voltage increases beyond this point the target collector current drops proportionately. When the collector cup current density and the total collector current density are equal, a satisfactory beam uniformity is obtained over the entire target area. For the case shown in figure 30 the current densities are equal for current densities less than about one-fourth of the unscanned target current density. From figure 29, this is seen to be equivalent to an overscan of about 80 percent so that the beam deflection distance, D, is equal to 1.8 times the diameter of the defining aperture.

Measurement of target area is critical in determining the correct implantation dose. It is advisable to use a calculated area based on the physical measurements of the system being used. The distances between the scanner, target, and defining aperture must be known to calculate the ratio by which the target area is larger than the defining aperture. Other methods, such as measurement of visible implanted areas, are subject to a number of uncontrolled factors, such as beam size and instability, that cause shifting of the beam and uncertainty in the location of the implanted region boundaries.

As the beam passes over the center of the target in the typical 80-percent overscan case, the integrator measures a square-wave type pulse. The pulse width gradually decreases with distance from the center, becoming zero during the maximum levels of the slower sweep voltage. The integrator must therefore be capable of measuring this wide variety of pulse widths which ranges from zero to about 250 μs.

In order to investigate the accuracy of the current measurements, two sources of current were used: 1) actual ion beam currents obtained from an implantation system and 2) simulated current pulses obtained from a pulse generator. The currents in both instances were measured and compared using five different commercially available current integrators as well as other current measuring instruments. The readings were taken from dc conditions to 10,000 pulses per second (pps). The ion beam scanner unit used was variable over a range from 20 to 2000 pps; the remaining frequencies were covered with the pulse generator. Average current readings were checked over the range from about 50 nA to 500 μA, usually with a 50-percent duty cycle.

The preliminary conclusions from these studies are that all the current integrators agree within a few percent for dc conditions, but only three of the five agreed within 10 percent for 10 to 2000 pps. Inconsistencies were observed between 1 and 10 pps; above 2000 pps other anomalies were observed. Therefore, both scan frequencies must be between 10 and 2000 pps; a ratio of 100 to 1 between the horizontal and vertical scan frequencies was found to be most desirable.

Errors related to measuring current pulses with peak amplitude greater than the full scale setting of certain of the current integrators were also encountered. All the current integrators performed well for peak ion beam currents less than 1 μA; four were satisfactory to 10 μA; three, to 100 μA; and two to 1 mA. Significant inaccuracies were observed for higher beam currents. Since the present trend in industry is toward the use of implantation currents of the order of 1 mA or more, these inaccuracies may cause difficulties in defining and comparing implantation conditions.

(R. G. Wilson[§] and D. M. Jamba[§])

5.4. Passivation Integrity

A corona discharge, reverse decoration technique was found to be a rapid, nondestructive method for decorating cracks and other defects in passivation overcoats [70]. This is a two-step method. In the first step, ions from a glow discharge at atmospheric pressure are deposited on insulating regions of the device. Then the device is immersed in a suspension of oppositely charged particles which are attracted to the charged insulating regions.

The charging process is illustrated schematically in figure 31. The source of ions is an array of seven parallel 40-μm diameter nickel alloy wires, 1.8 cm apart, held in a plastic frame in a horizontal plane. The power supply is typically an rf-type, high-voltage, dc source capable of ±10 kV and a maximum current of 10 mA. A grounded plate, not shown in the figure, is placed about 3 cm above the wires to provide greater current uniformity and to protect the wires from mechanical damage. The specimen is placed on a

[§]Work performed at Hughes Research Laboratories under NBS Contract No. 5-35891. NBS contact for additional information: K. F. Galloway.

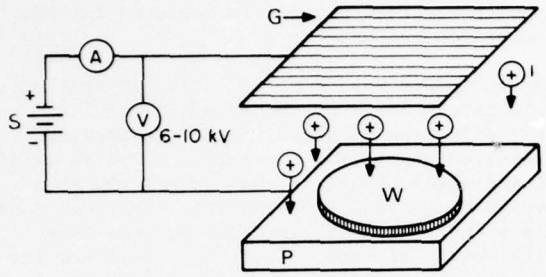

A Ammeter
G Corona grid wire array
I Ions
P Ground plate
S Power supply
V Voltmeter
W Specimen wafer

Figure 31. Schematic representation of corona charging with positive ions.

grounded plate about 2 cm below the wire array.

The charging process is carried out in a nitrogen atmosphere with about 25-percent relative humidity for 15 to 20 s. It was established that the charging of a surface containing closely spaced insulator and conductor regions is limited mainly by the conducting areas. As the ions collect on the insulator they generate an electric field in the gas ambient which causes subsequent ions to move toward the regions of ground potential before arriving at the wafer surface. Thus, for the geometries of interest, the oxide surface voltage is not determined by the oxide breakdown potential (except for very thin oxides or very large insulator areas).

The ambient relative humidity must be controlled to prevent lateral current flow on the oxide surface. The oxide surface voltage decay rate after charging was found to increase greatly above 30-percent relative humidity for thermal silicon dioxide, chemical vapor deposited (CVD) silicon dioxide, and CVD phosphosilicate glass (PSG). The surface voltage also decays rapidly if the bulk conductivity of the oxide is high due to the presence of moisture. Thus, for some wafers with CVD silicon dioxide or PSG passivation, it was found to be necessary to remove adsorbed or absorbed water before charging. This can be done by heating in room air at 200°C for 5 min. This has been made the initial step in the standard charging process to ensure retention of surface charge on the specimen.

This procedure is satisfactory for devices or wafers in which the passivating layer has been etched open at the contact pads or at the grid lines. These etched regions furnish the closely spaced insulator-conductor geometry required so that the surface voltage does not depend on whether the passivating layer is over metal or over insulator. It is also possible to decorate wafers before the passivation layer is etched open by placing a grounded conducting grid over the wafer during the charging. A convenient grid consists of an aluminum sheet 0.8 mm thick with 3.5-cm diameter holes on 5.0-cm centers. When the grid is used, charge is deposited only at openings in the grid. The entire wafer can be charged if the grid is moved laterally during charging while it is spaced about 0.3 mm above the wafer.

An important consequence of the charging properties is that the surface charge and potential around a defect decreases laterally as the defect is approached. This is due to ion deflection during charging and to surface conduction. Thus, there is a margin around a crack or pinhole of lower surface potential than the potential in nondefect areas. This effect increases detectability since it magnifies the defects as far as charged particle deposition is concerned. The margin is of the order of 25 μm in lateral dimension.

It is necessary that the surface charge remain on the passivating layer for a time about equal to the delay between charging and deposition plus the deposition time. The dielectric relaxation time of the passivation layer must be longer than the total time which is about 20 s. Thus, a bulk resistivity of about 10^{13} Ω·cm or greater is needed. The resistivity of an insulating layer may be increased by reducing its temperature; this can be accomplished by cooling the specimen during charging and by the use of cooled particle suspensions.

The reverse decoration process is illustrated schematically in figure 32. This process has been accomplished with various powders including phosphors, zinc oxide, and lead aluminosilicate glass, but the best results in terms of sensitivity and contrast were obtained using carbon black suspensions. Various carbon black suspensions were tested. These included commercially available electrophotographic toner concentrates and specially prepared formulations.

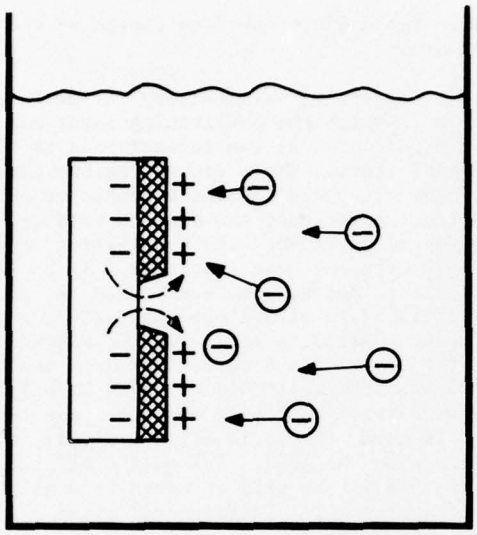

Figure 32. Schematic representation of the reverse decoration of defects with negative ions following corona charging with positive ions.

Best results were obtained with a carbon black suspension prepared in the following way.[¶] First, a concentrate is made from 17.0 g Raven 1255 carbon black [71], 100.0 ml toluene, 10.0 ml of a mixture of 50 g Lubrizol 894 [72] in 50 ml toluene, and 10.0 ml of a mixture of 50 g A-C Polyethylene, grade 430, [73] in 90 ml toluene. These materials are readily available.[#] The carbon black has a mean particle diameter of 22.0 nm and a nitrogen absorption surface area of 130 m^2/g. The surface of the carbon black as supplied is acidic by addition of volatiles [71]. Lubrizol 894 is an ashless dispersant additive for heavy duty engine oils; the weight percent of nitrogen ranges from 1.65 to 1.95 percent [72]. A-C Polyethylene, grade 430, is a polyethylene-vinyl acetate copolymer (30 percent vinyl acetate); its softening point is 60°C [73]. The concentrate is agitated for about 5 min with a 100-W ultrasonic probe to disperse the carbon black.

To make the dilute suspension, about 1 ml of the concentrate is added to 400 ml of Freon TF[#] and stirred. This results in a suspension which contains about 0.1 g of carbon black. This amount has been found to be adequate for decorating at least ten 3-in. (76-mm) diameter wafers. Both the concentrate and the dilute suspension are stable for long periods (months). In this suspension, the carbon black is negatively charged so that positive corona potentials are used for reverse decoration.

Measurements were made to characterize the electrical state of the carbon particles in the dilute suspension. These measurements involved depositing the carbon black on metal foils while recording the current and then weighing the deposited carbon. This was done as a function of applied voltage and time. The weight of carbon black deposited and the charge transported varied approximately linearly with voltage and time. For electrode spacings of 1.7 cm on each side of a metal foil, an applied voltage of 10 V for 4 min resulted in a deposition of 3.2×10^{-4} g/cm^2 of carbon black. The average charge per single particle of carbon black, with the assumption that all such particles were 22.0 nm in diameter and singly dispersed, was 0.05 times the electronic charge. Since the minimum charge per particle is one electronic charge, it is clear that the carbon black is aggregated to at least a factor of 20 times. This aggregation is essential for obtaining dense black on the charged insulator surface.

The detection of cracks and pinholes decorated in this way is quite convenient under microscopic observation. An example is shown in figure 33. It was demonstrated that every defect detected by etching of the underlying aluminum through the defects was detected by the carbon black reverse decoration procedure. This was done in two ways. Wafers and chips were decorated with carbon black and photomicrographs were taken of crack and pinhole patterns. The carbon black was then removed and the aluminum was etched (NBS Spec. Publ. 400-25, p. 33) at 50°C for 5, 7, 10 or 15 min. The specimens were then photomicrographed again and the results compared. Hundreds of micrographs from many different specimen types were compared, and, in every case, all defects detected by etching were also clearly outlined by the carbon black. In the second method, specimens were decorated with carbon black and then aluminum etched with the carbon black in place. Again, the correlation was excellent. An example of the latter test is shown in figure 34.

The density of demarcated or decorated localized structural defects in a dielectric layer can be determined by counting the number of

[¶]This suspension was originally formulated by G. S. Lozier, RCA Laboratories.

[#]See disclaimer, p. viii.

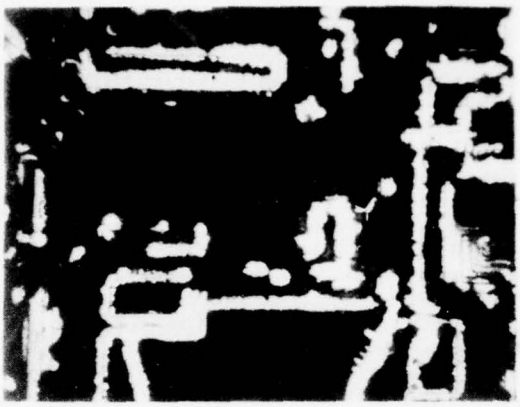

Figure 33. Photomicrograph of reverse decorated device showing high contrast which renders microscopic evaluation fast and sensitive. (Magnification: ∿100x.)

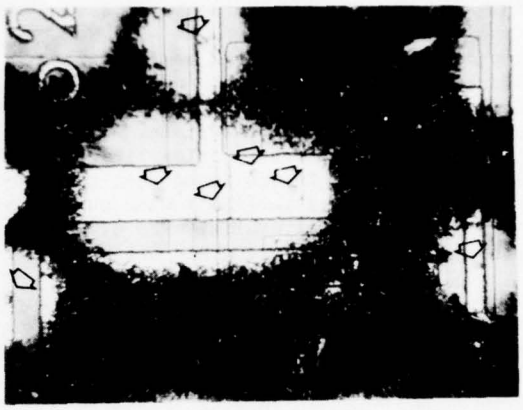

Figure 34. Photomicrograph of portion of reverse decorated device aluminum-etched at 50°C for 5 min without removing carbon black. (Magnification: ∿325x; etched defects appear inside the regions without carbon black as denoted by the arrows.)

defect sites per unit area, using one of several microscopic techniques discussed previously [74]. The choice depends on the uniformity and density level of defects, the type of material used in decorating, the degree of accuracy required, and the specific purpose of analysis. Incident white-light, bright-field illumination is most suitable for observing specimens decorated with carbon black. The magnification used should be sufficient to allow resolution of individual demarcated defect sites, but not higher, so that the largest possible specimen area is included within the field of view. It is impossible to specify a fixed magnification that would hold for all cases, but a magnification in the range from 50 to 500 diameters has been found to be most useful.

The greatest difficulty in determining the density of defects by any method concerns the distribution uniformity. If the uniformity of distribution is "good", counting within a few sites may provide an adequate measure of the true statistical distribution. If it is "fair", which is the most common occurrence, examining a substantial number of areas (5 to 15) over the specimen may be necessary to arrive at a valid average density value. Specimens with "poor" uniformity are best treated by dividing it into "good", "fair", and "poor" regions and computing separate density values for each, rather than computing a meaningless average value.

The sampling areas for counting should be spread reasonably uniformly over the specimen surface. If the specimen is a device wafer or is otherwise patterned, one may choose to examine every nth unit, and count the defects within that defined area. If the specimen is not patterned, then the microscope stage micrometer can be used to space the observation sites uniformly over its area. The circular area of the microscope field of view for the magnification may be used as a convenient unit. Photomicrography affords a useful record of the defect density and often facilitates counting of the defect sites, especially if the density is high; it also provides an accurately defined area of the specimen surface.

A major advantage of the carbon black reverse decoration method is the high optical contrast available in reflected-light microscopy. This high contrast permits a fairly simple form of automated quality assessment with a microscope-mounted photocell to measure the integrated light reflected from the defect areas. This technique is much simpler than the use of computer-implemented image analysis. Although the latter would provide a defect count, which the integrated reflected-light method does not furnish, it is believed that the simple method explored here could be used in a production facility to rank wafer quality and set a pass, no-pass criterion.

Initially, photomicrographs were made of carbon black reverse decorated devices on integrated circuit wafers. Transparencies made from these micrographs were then mounted in an optical system so that a collimated light

beam was passed through the transparency and then focused on the faceplate of a vacuum photocell to form an image of the light source. An image of the transparency is not desired since the photocell response may not be uniform across the faceplate. The current output of the photocell varies linearly with incident light. It was found that the current output varied inversely with subjective judgments of device quality made by counting pinholes and estimating crack lengths.

Based on these preliminary encouraging results, a photocell-microscope system was assembled to take direct readings of reflected light from decorated wafers. The arrangement used is shown schematically in figure 35. By placing a plano-convex lens with a focal length of 57 mm at the end of the camera tube, an image of the light source field stop was obtained at the photocell faceplate about 6 cm from the end of the camera tube. The photocell employed an S-11 cathode and was operated at 100 V. Light intensity was adjusted to give convenient current levels and the overall magnification was chosen so that a large portion of the circuit was visible, but bond pads and grid lines were excluded. Shielding prevented introduction of ambient light. Photocell current readings were taken on 20 circuits of each of two wafers. For the "good" wafer, the lowest individual current was 2.9 nA, the highest was 5.5 nA, and the average was 3.5 nA. For the "bad" wafer the lowest current was 6.7 nA, the highest was 15 nA, and the average was 10 nA. Pinhole counts on these wafers resulted in a difference of a factor of two in defect density. Thus, the photocell current measurement can easily detect a difference of a factor of two in pinhole density and is probably more sensitive than this.

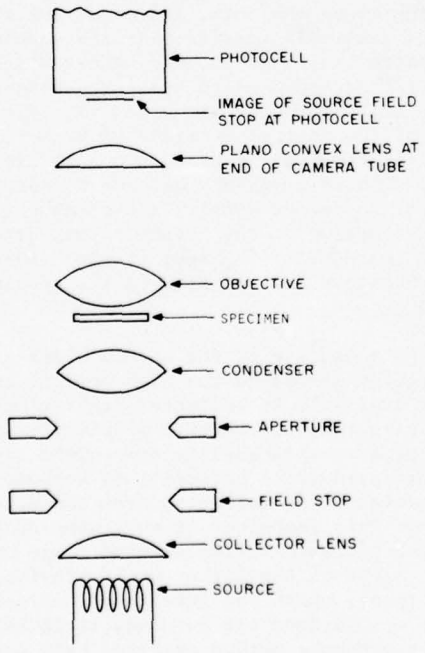

Figure 35. Schematic representation of microscope modified to obtain image of source field stop at the photocell to measure the integrated light reflected from defective areas. (Note that in the actual (vertical illumination) system the source and photocell are on the same side of the specimen.)

The only fundamental limitation encountered thus far has been devices with regions of metal not connected to the semiconductor. This floating metal is brought to a high potential by the corona so that the metal is outlined with carbon black, but no defects can be detected over it. Thus, the process cannot be used with floating gate memory devices, for example, unless the floating metal can in some way be grounded or connected to the semiconductor body.

The carbon black can be removed by soaking the specimens in toluene for 15 min, followed by ultrasonic agitation in toluene and rinsing in Freon TF.[#] When ultrasonic energy is used, care must be taken to avoid specimen damage. Contact of the wafer with hard surfaces, such as beaker sides or bottom, should be avoided. It has been found that careless use of the ultrasonic bath has actually caused pinholes in previously good passivating layers.

Several experiments were conducted to establish that this method is nondestructive. First, a set of device wafers was aluminum etched to reveal pinholes. Then the wafers were exposed to the corona discharge at 10,000 V dc for various times ranging up to 100 s. After the corona discharge, aluminum etching revealed no new pinholes.

In a second test, one set of five device wafers was reverse decorated with carbon black and a second set of five was direct decorated with phosphor (NBS Spec. Publ. 400-25, p. 34). After cleaning, the decoration was repeated. This process was repeated for a total of five times. Only one wafer showed new defects (pinholes). During cleaning, this wafer had

[#]See disclaimer, p. viii.

been placed face down in the bottom of the ultrasonic tank and it is believed that the mechanical contact caused these defects. Subsequent tests with the ultrasonic tank used in this manner did induce defects.

A third test involved automatic probe testing of C-MOS wafers. These were chosen since it is expected that C-MOS devices are most susceptible to static electrical damage. Two 3-in. (76-mm) diameter C-MOS device wafers were probed, and a map was made of good and bad devices. Then the wafers were charged, decorated, and cleaned. The wafers were probed again. One wafer showed a net loss of four devices out of about 130 good devices, initially. The other wafer showed a net gain of five devices out of about 100 good devices, initially. These variations are within the normal tolerance of repeated wafer probe testing.

It was concluded that the process of corona charging and decoration is nondestructive. However, since no life tests have been carried out on decorated and cleaned devices, the effect of this test on service life and reliability has not yet been directly established. (W. Kern[×] and R. B. Comizzoli[×])

5.5. Process Materials Characterization

Boron Nitride Diffusion Sources — Transport studies were made of known amounts of zinc from simulated boron nitride diffusion sources. Two glasses, which were designed to simulate the oxide layers on activated boron nitride of two types (pure and mixed with silica), were prepared with admixtures of 0.75 mole percent zinc oxide [75]. One of the glasses was boron oxide (B_2O_3) and the second was a borosilicate glass composed of silica (SiO_2) and boron oxide in a 3 to 7 weight ratio. The transfer experiments were conducted at 1000°C in a dry nitrogen atmosphere for times up to 12 h. The glass which formed on the surface of the silicon wafer was analyzed for zinc by means of flameless atomic absorption. In the case of the B_2O_3 glass, no zinc transfer was observed within the detectability limit of one part per million by weight. The zinc content of the borosilicate glass is shown in table 10. The confidence limits for these data have not been established at this time, but it seems likely that the variations are not statistically significant. (J. Stach[+], T. A. Yager[+], and R. E. Tressler[+])

Table 10 — Zinc Content in Glass Transferred from Doped Borosilicate Glass to Silicon at 1000°C

Time, h	Zinc Concentration, ppm (by weight)	
	Trial 1	Trial 2
0.5	210	295
1.0	65	140
2.0	40	100
3.0	70	120
4.0	45	100
5.0	440	145
12.0	615	135

Hydrogen Chloride Gas — The SOLGAS program [76] was used to compare the equilibrium partial pressures at 1100°C of the chemical species in the hydrogen chloride (HCl) and trichloroethylene (TCE) oxidation systems. The most significant difference is that the partial pressure of water vapor in the TCE system is lower by an order of magnitude when compared with that in the HCl system [77]. The calculations also indicate that the partial pressure of ClO is nearly equal in both systems whereas the partial pressures of HCl, HO, and HOCl are approximately five times greater in the HCl system. (R. Tressler[+], W. H. Grubbs[+], M. B. Das[+], and J. Stach[+])

[×]Work performed at RCA Laboratories under NBS Contract No. 5-35913. NBS contact for additional information: T. F. Leedy.

[+]Work conducted at the Pennsylvania State University under NBS Contract No. 5-35717. NBS contact for additional technical information: R. I. Scace.

6. PHOTOLITHOGRAPHY

6.1. Line-Width Measurement with Spatially Filtered Coherent Optical Radiation

Measurement of the widths of lines and spaces on the order of 1 μm wide or less is made difficult since this regime lies at the resolution limit of optical microscopes. In this regime, imagery tends to be nonlinear (see sec. 6.2.) because of the partial coherence of the illumination. The nonlinearity is generally evidenced by edge ringing which distorts the image of the line edges.

The common attachments used on the microscope for line-width measurement are the filar and image-shearing eyepieces. The problems in applying these when measuring narrow lines have been detailed previously (NBS Spec. Publ. 400-19, pp. 34-41) [78]. An analysis has demonstrated that these problems can be alleviated if the image is properly spatially filtered [79].

The analysis is based on a microscope which employs a single-lens coherent optical system as shown in figure 36. For illustration, an opaque line in a clear background is shown as the object, A. The objective lens, B, assumed to be thin, forms a real image in the image plane, D, a fixed distance, Z_2, away. This distance, which is called the tube length, has been standardized at about 160 mm. Although an ocular is added in a microscope to form a virtual image with apparent magnification given by the product of the magnifications of both elements, the significant imagery is carried out by the objective and the ocular can be ignored in the analysis. The Fourier transform of the object field, the complex object spectrum, is located at a plane, C, one focal length, f, behind the lens.

The physical makeup of the microscope in the σ-plane determines the frequency content of the image. The outer aperture of the system determines the spatial frequency limit of this plane; the origin of the σ-plane is equivalent to optical "dc", and spatial frequency increases linearly outward to the aperture limit. A clear aperture therefore acts as a low-pass filter, passing without attenuation all frequencies below its upper cutoff, but truncating all those above. If an opaque line of width $2\sigma_1$ is inserted in the center of the σ-plane, frequencies lower than σ_1 will also be truncated. With such an occluding band-pass filter, it can be shown that the image of an opaque line in a clear background is identical with that of a clear line in an opaque background [79]. For an optimum filter, the image has a zero intensity at the line-edge image locations; examples of such images are given in figure 37. The optimum filter is defined such that

$$\sigma_1 = \{1/[(2\pi)(2a)]\}\,{}^{0}\mathrm{Si}^{-1}\{\mathrm{Si}[(2\pi)(2a\sigma_2)]\} \quad (9)$$

where σ_1 is the lower cutoff frequency, σ_2 is the upper cutoff frequency, 2a is the width of the line, $\mathrm{Si}[x] = \int_0^x [(\sin\xi)/\xi]\,d\xi$ (the sine integral), and the pre-superscript zero on the inverse sine integral indicates that the lowest value (between 0 and π) must be taken. The upper cutoff frequency is determined from

$$\sigma_2 = (\mathrm{NA})/\lambda \quad (10)$$

where (NA) is the numerical aperture of the objective lens and λ is the wavelength of the incident illumination; this is the diffraction limit. Thus, for any given microscope system, the optimum values of σ_1 and σ_2 are fully defined for a specific line width, 2a.

Since lines of unknown test width cannot *a priori* be paired with their optimum filters, measurements must be made on images formed by non-optimum filters. To assess the ability to correct routine measurements made with non-

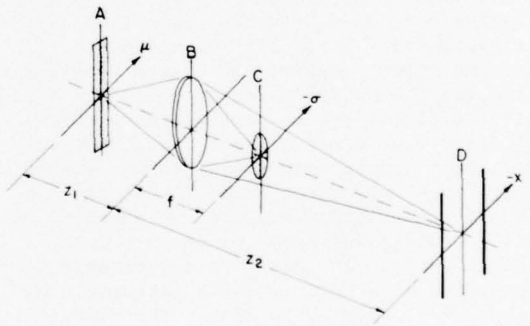

A Object plane, with an opaque line as the object
B Plane of lens
C Plane of object spectrum, located one focal length from the lens, with an opaque obstacle inserted at the center of the field.
D Image plane, with an idealized filtered image.

Figure 36. Sketch of the single-lens coherent optical system, showing the locations of various planes and coordinate systems.

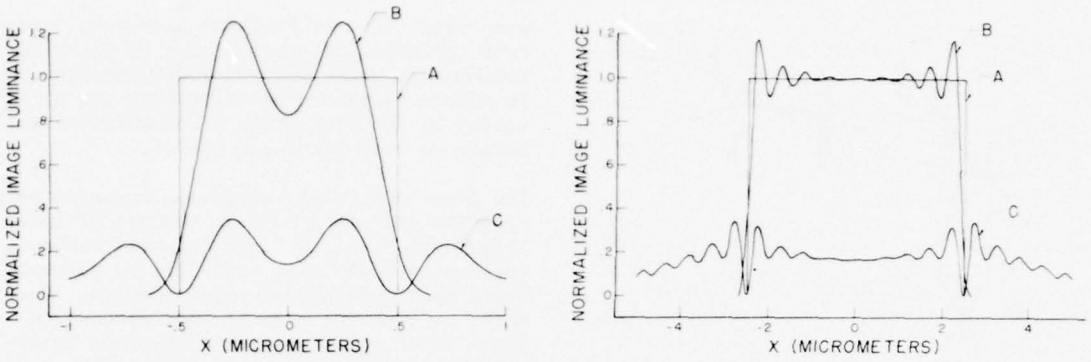

a. Width of line: 1 μm.

b. Width of line: 5 μm.

Figure 37. Calculated images of clear lines in opaque backgrounds for coherent illumination of wavelength 500 nm, and a 0.95 numerical aperture objective lens. (A: object line; B: image without filtering; C: image with optical filtering.)

optimum filters, calculations of the measured dimension of 4.6-, 5.0-, and 5.75-μm test line widths were carried out for filters optimized for 4.0-, 4.75-, 5.5-, and 6.0-μm lines; and of 1.7-, 2.0-, and 2.3-μm test line widths for filters optimized for 1.6-, 1.8-, 2.1-, and 2.4-μm lines. All of these calculations were made for objective lenses with numerical apertures of 0.5, 0.65, and 0.95. These calculations [79] showed that when the lines are well-resolved by the optics, as are the lines greater than 4 μm for all the numerical apertures used, measurements can be corrected to less than 1 percent of their actual dimension for all of the filters used. However, when the lines are marginally resolved as in the case of the nominal 2-μm grouping, the range of filters with which they can be imaged and the measurements corrected is greatly reduced. An important result of the calculations shows that when the measurements can be corrected, the errors are reduced to the order of hundredths of a percent for all numerical apertures.

The problems associated with misalignment of the filters were also examined [79]. The effect of such misalignment is to change the zero intensity at the line-edge image location to a minimum because a shift in the cutoff frequencies results in unequal portions of positive and negative sides of the spectrum passing through to the image. The largest error is produced by physically misaligning the lower cutoff filter. However, fabrication of adequate filters should be well within normal machine tolerances since the effects of misalignment of optimum filters corresponding to these tolerances are vanishingly small, and no significant measurement error should result.

To implement this filtering-measurement system successfully in a microscope, it is clear that the lower cutoff frequency must be adjustable. With a continuously adjustable filter, once a test line is placed in the system, the lower cutoff is continuously increased from zero until an image is obtained similar to those in figure 37 with the line edges defined by zero intensity and approximately equal luminance peaks on either side of the zeroes. If an appropriate correction algorithm [79] is then applied, the resulting line width can be accurately determined.

One way to achieve a variable filtering which appears to be feasible would be to prepare a high-precision adjustable slit so that its surfaces are reflecting. The lower cutoff is achieved by opening the slit to allow the unwanted portions of the spectrum to pass through and be trapped while the desired portion of the spectrum is reflected into the system along a different optical path and is imaged. A conceptual scheme of this is sketched in figure 38. Implementation of this scheme would necessitate a partial redesign of some microscope systems, but in some models presently in use, such a path is already incorporated. Since nonuniformly opening slit jaws can be compensated through calibration, imperfect jaw motions need not be a bar to application.

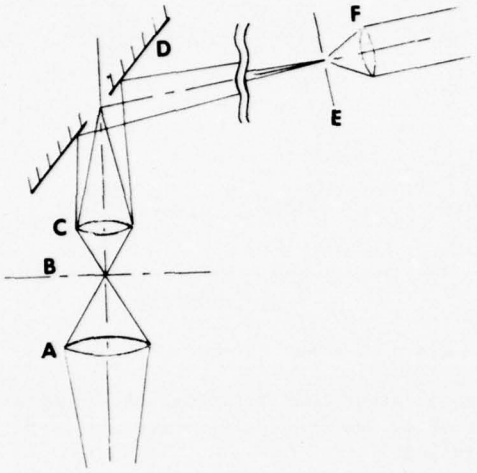

A Substage condenser lens
B Specimen (object plane)
C Objective lens
D Front-surface mirror, with its center one focal length from the lens, C, and an opening which can be varied as the jaws of a slit; the portion of the image spectrum that is eliminated passes through this opening
E Plane of intermediate image, one tube length from the lens, C
F Microscope eyepiece

Figure 38. Sketch of a possible configuration for a microscope system with spatial filtering.

Although this technique appears to be theoretically feasible, there are several practical limitations. Most present microscope objectives are designed so that the object spectrum imaged by the objective lens is located inside the physical dimensions of the lens system where a filter cannot be constructed. Introduction of additional optics to re-image this spectrum would degrade the performance of the objective and compromise the system. Reflecting objectives or catadioptric systems could be used without major modifications, but their range of numerical apertures is limited. Full and unrestricted application of these ideas will require that microscope objectives be redesigned to place the object spectrum outside the last glass surface.

It was assumed for this analysis that the line shapes had a rectangular profile and possessed symmetry about their centerlines. Not very many lines in practice have such a perfect profile, and the modeling of lines to accommodate variations in their description is necessary before these results can be extended to the prediction of measurement accuracy on real lines and spaces.

The large number of reflecting surfaces in microscope systems precludes the use of laser illumination with a large temporal coherence because the resulting interference patterns would seriously affect image clarity. Further, because the size of the intended objects is so small, lateral coherence intervals need not be extremely large. The mercury arc, filtered for the 546.1-nm line, appears to provide sufficient lateral coherence and virtually no temporal coherence, and would seem to be ideal because the green wavelength is near the peak of the eye response and would be reasonably comfortable for viewing. On the other hand, since radiance falls off as the square of the magnification, and because the central portion of the spectrum where most of the image energy is located is occluded in the filtering process, high illumination power is required. Additional testing is necessary to choose the best light source.

A great many simplifications were introduced in the analysis. The simple scalar theory employed is sufficient to illustrate the technique and develop the basic concepts, but at the high numerical apertures that must eventually be used in a practical system, a more rigorous analysis is needed. In addition the assumption of diffraction-limited optics ignored the spherical aberration, flare light, and the difficulty of focusing in coherent illumination that are commonly present with such systems. Flare light alone is sufficient to significantly reduce the contrast of the imagery of the zero crossings at the line edges. To develop this technique more fully it will be necessary to take these practical aspects of the microscope into account. (R. E. Swing*)

6.2. Optical Imaging for Photomask Metrology

Theoretical and experimental investigation of the optical microscope, as used for linewidth measurement on photomasks, continued. A research microscope system, shown schematically in figure 39, was assembled to make

* NBS Optics and Micrometrology Section, Mechanics Division.

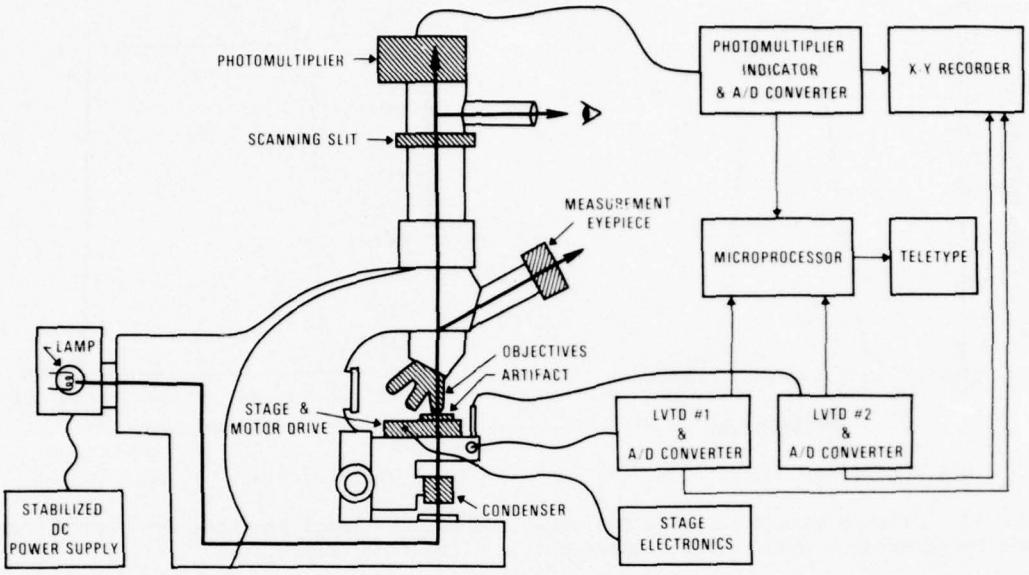

Figure 39. Diagram of optical research microscope as modified for line-width measurement.

photometric scans of line image profiles for comparison with theoretically computed profiles.

The system is based on a commercially available research microscope modified to include a higher-wattage tungsten-halogen lamp, smaller scanning apertures to produce higher resolution of the scanned image, a special one-dimensional scanning stage controlled by a stepping motor with function generator drive, and linear voltage transducer (LVTD) gauges for positional readout of stage and focus settings. Both analog and digital outputs are available from the photometer and gauges. The analog outputs of the photometer and position gauge are fed to an X-Y recorder; the digital outputs are intended for use with a microprocessor-based data handling system now being constructed.

In addition, the prism beam splitter, which appears to obscure part of the light path, was removed and the incident illumination was filtered by a combination of a Wratten No. 60 filter and a heat reflecting mirror to produce a limited passband peaked at about 560 nm. Use of a scanning slit instead of a circular aperture was found to improve overall system performance by reducing photon noise as a result of the increased flux reaching the detector and by averaging over some of the minute imperfections along the edges of the lines being scanned.

Although a variety of optics and scanning apertures may be used, the system has been found to give best optical performance for viewing photomasks in transmitted light when employing a 63x, 0.9 NA objective lens, designed for use without a cover glass, as the objective and a 32x, 0.6 NA long-working distance objective lens as the condenser. This combination of optics appeared to produce minimal flare.

Measured line-image profiles of typical clear lines on a chromium-on-glass photomask are shown in figure 40. Some edge ringing, characteristic of images formed with coherent or partially coherent light, is evident.

Calculated line-image profiles corresponding to the measured line images are also shown in figure 40. These calculations were made with a computer program which takes into account a wide range of operating parameters including partial coherence, lens aberrations, scanning slit width, objective numerical aperture, and variations in the object being scanned including geometry, edge degradation, and contrast. The computation involves numerical integration of a three-dimensional integral whose integrand is complex and oscillates over the range of integration. The derivation is omitted here, but the integral in one-dimensional form is

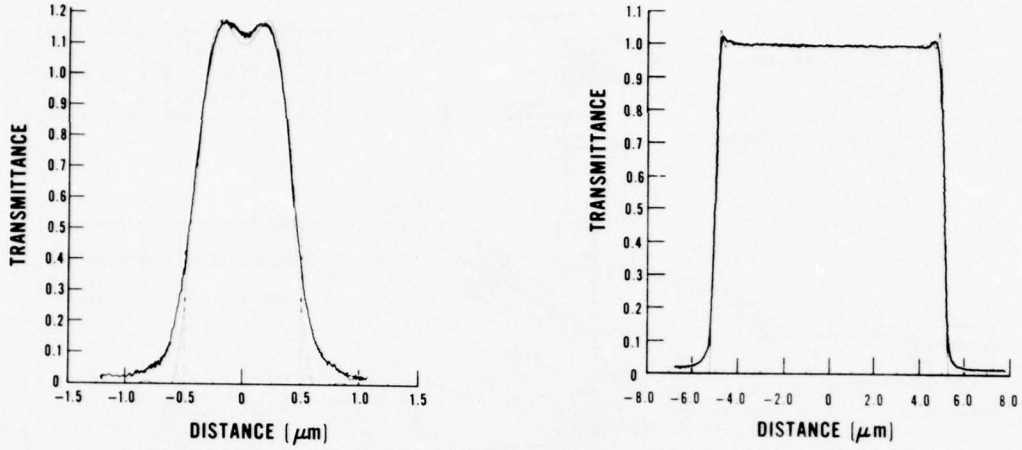

a. Width of line: 1 μm.

b. Width of line: 10 μm.

Figure 40. Calculated and experimentally determined line-image profiles for clear lines in opaque backgrounds. (Heavy line: experimental; light line: calculated.)

$$I(\xi_o) = \iiint \tilde{\Gamma}(\alpha)\tilde{t}(\alpha-\mu_2)\tilde{t}(\alpha-\mu_1) \times \exp\left[-\frac{ik\xi_o}{Z_1}(\mu_1-\mu_2)\right] F(\mu_1)F(\mu_2) \times \tilde{S}\left(\frac{\mu_2-\mu_1}{\lambda Z_2}\right) d\alpha d\mu_1 d\mu_2, \quad (11)$$

where $I(\xi_o)$ is the image profile seen by the photomultiplier, $\tilde{\Gamma}(\alpha)$ is the Fourier transform of the mutual coherence function at the object, $t(\mu)$ is the Fourier transform of the amplitude transmittance of the object, $F(\mu)$ is the pupil function of the imaging objective, $\tilde{S}(\mu)$ is the Fourier transform of the intensity transmittance of the scanning aperture at the photomultiplier, and Z_1 and Z_2 are the object and image conjugates of the objective, respectively.

A detailed study of the coherence properties of the microscope, which is not reproduced here, has shown that for typical modes of operation, $\tilde{\Gamma}(\alpha)$ is the modulus squared of the pupil function of the condenser. Thus, as has long been known [80], the aberrations of the condenser lens do not affect the imagery. However, it is noted that the conditions under which this formulation is applicable are that the condenser aperture be uniformly illuminated (making it the limiting aperture in the illumination system regardless of the mode of illumination) and that the illuminated area at the object be large compared to the dimensions of the impulse response of the condenser. When the area of illumination becomes very small the system must be treated theoretically as a microdensitometer for which a different description applies [81].

The amplitude transmittance spectrum $\tilde{t}(\mu)$ of the object is general and can be changed as desired. At present, single and multiple lines with variable contrast and edge degradation have been considered. The pupil function, $F(\mu)$, of the imaging objective, assumed to be diffraction limited, includes the aberration function and the various terms corresponding to defocus and spherical aberration, etc., may be varied. This formulation assumes quasi-monochromatic illumination of mean wavelength λ and does not take into account the variation of the aberration function or other parameters with wavelength.

Although the agreement between the measured and calculated line-image profiles is quite good, which suggests that the system can be used to measure the width of transparent lines nearly as narrow as the impulse response of the objective lens, differences do remain. It is felt these are due principally to 1) the unknown influence of edge quality which would affect the 1-μm line imagery more than the 10-μm line imagery, 2) non-zero transmittance of the opaque background, and 3) the presence of undetermined amounts of optical aberrations in the system, principally spherical aberration. (D. Nyyssonen[†])

[†]NBS Optical Physics Division.

6.3. Calibration Standards for Photomask Metrology

Artifacts of the design previously described (NBS Spec. Publ. 400-17, pp. 37-38) have been successfully manufactured. These artifacts consist of the hard-surface material, either "black" chromium approximately 90 nm thick or iron oxide approximately 180 nm thick, deposited directly on a 6-mm thick polished glass substrate, approximately 36 mm square. They contain design patterns of from one to four cycles with both clear lines on opaque backgrounds and opaque lines on clear backgrounds. Compatibility with the scanning electron microscope is achieved by overcoating the artifact with approximately 50 nm of carbon (NBS Spec. Publ. 400-19, p. 41).

Figure 41 is a photomicrograph of the pattern on a chromium-on-glass artifact as observed in an optical microscope with bright-field transmitted light at about 85x magnification. At this magnification, the multiple 1-μm wide lines and spaces cannot be resolved. Dimensional measurements (see sec. 6.4.) show that the line widths as measured with an optical microscope generally equal the design values to within the specified tolerance of ±0.25 μm.

The 180-nm thick iron oxide is partially transmitting and equivalent to coatings used on some "see-through" integrated circuit photomasks. Viewing these specimens under transmitted light in an optical microscope shows a dark border at the edge of the iron oxide as shown in the photomicrograph of four 1-μm wide clear spaces in an iron oxide artifact in figure 42. The cause of this optical effect has not been identified, but it results in a large uncertainty in setting the image-shearing and filar eyepieces for optical linewidth measurements. For this reason and also because the edge profile of iron-oxide lines is less sharp than that of chromium lines, iron-oxide artifacts are not being considered for primary line-width calibration with the SEM interferometer. (J. M. Jerke[§])

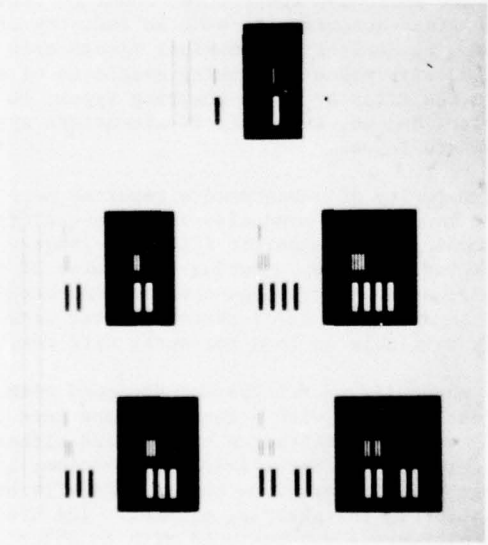

Figure 41. Photomicrograph of chromium-on-glass artifact, viewed under bright-field transmitted light at a magnification of about 85x.

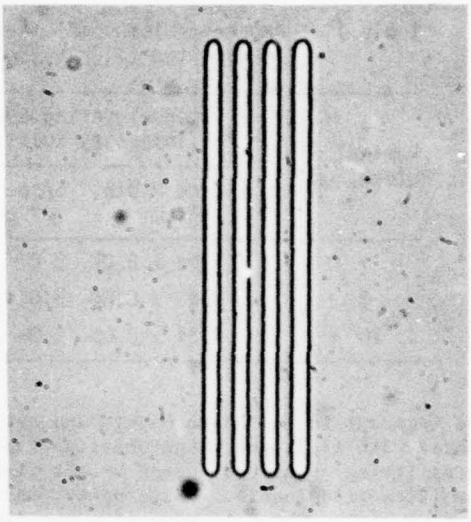

Figure 42. Photomicrograph of four 1-μm wide clear spaces each separated by 1 μm in an iron-oxide-on-glass artifact viewed under bright-field transmitted light at a magnification of about 2000x.

6.4. Line-Width Measurements on Chromium-on-Glass Artifacts[¶]

Line-width measurements were made with an optical microscope on several chromium-on-glass artifacts (see sec. 6.3.). Single opaque lines on a clear background and single clear

[§] NBS Optics and Micrometrology Section, Mechanics Division.

[¶] Funded through the NBS Dimensional Metrology Program.

Table 11 — Apparent Widths of Lines and Spaces Measured in Bright-Field Transmitted Illumination

Nominal Width, μm	Image-Shearing Eyepiece (Intensity Splitting)		Filar Eyepiece	
	Line Width, μm	Space Width, μm	Line Width, μm	Space Width, μm
1	1.04 ± 0.07	0.87 ± 0.03	0.75 ± 0.21	1.18 ± 0.08
3	3.03 ± 0.06	3.01 ± 0.06	2.84 ± 0.13	3.25 ± 0.02
10	9.84 ± 0.05	9.98 ± 0.04	9.73 ± 0.26	10.31 ± 0.20

lines (spaces) in an opaque background were measured with filar and image-shearing (intensity splitting) eyepieces using bright-field transmitted illumination. Five measurements were made of the width of each of three lines and spaces using each eyepiece. The means and three-sigma values (three sample standard deviations) are listed in table 11. These data further confirm the previously reported result that with transmitted illumination the filar eyepiece indicates a wider width than the image-shearing eyepiece for clear spaces and a narrower width for opaque lines (NBS Spec. Publ. 400-19, pp. 38-41, 41-43).

An investigation into the effect of focal position on line-width measurement with an optical microscope was also made. Measurements were made on a single clear space, nominally 3-μm wide, in bright-field transmitted illumination with the image-shearing eyepiece. The objective lens had a magnification of 63x, a numerical aperture of 0.90, and a depth of field of 1.23 μm. The position of best focus was a subjective decision by the operator based on the quality of the image. The results obtained at seven focal positions, extending beyond the normal depth of field, are given in table 12. Within this range, the clear line measures maximum width at or near best focus. This result is also consistent with the previously reported model (NBS Spec. Publ. 400-19, pp. 38-41). (F. W. Rosberry[#])

Table 12 — Effect of Focal Position on the Apparent Width of a Clear Space Measured with an Image-Shearing Eyepiece in Bright-Field Transmitted Illumination

Distance from Best Focus, μm	Measured Width, μm
-1.5	2.87 ± 0.14
-1.0	2.93 ± 0.19
-0.5	2.91 ± 0.06
0.0	3.00 ± 0.05
+0.5	3.00 ± 0.06
+1.0	2.96 ± 0.10
+1.5	2.98 ± 0.10

An experimental comparison was made of line-width measurements using optical microscopes and operating conditions representative of those employed by the microelectrics industry for photomask inspection. Most photomask line-width measurements made in industry are done with conventional optical microscopes fitted with visual measuring eyepieces of either the filar or image-shearing types; to a limited degree, automatic TV-microscope systems are in use.

The majority of measurements reported here were made with a monocular research-quality microscope with separate filar and image-shearing eyepieces. During the course of the study, a binocular image-shearing microscope and an automatic TV-microscope system were made available on loan for short term use.

The monocular microscope was equipped with an objective lens, with a numerical aperture of 0.95 and a magnification of 80x, and either bright-field or dark-field illumination; its image-shearing eyepiece had an intensity beam-splitter as the shearing element. The binocular microscope was equipped with an objective

[#]NBS Optics and Micrometrology Section, Mechanics Division.

lens, with a numerical aperture of 0.90 and a magnification of 63x, and bright-field illumination only; its image-shearing eyepiece had a polarization beamsplitter as the shearing element. The TV-microscope system was equipped with an objective lens, with a numerical aperture of 0.95 and a magnification of 80x, and bright-field illumination only. All three microscopes had both reflected and transmitted light capabilities. The three systems differed in their fundamental principles of operation and means of data output. The filar and image-shearing eyepieces require operator judgment for locating image edges in a line-width measurement; the TV system uses automatic image scanning and electronic thresholding. The filar eyepiece had a vernier scale readout which requires the calculation of line widths from arbitrary scale divisions; the binocular image-shearing system had direct digital readout as did the TV-microscope system.

Three filar eyepieces were available for use with the monocular microscope. One, with a 7x magnification and a movable, full-field pair crosshair configuration, had the best repeatability of the three and was used throughout the study. Preliminary repeatability tests for each of the optical microscope measurement systems resulted in variations from the mean of ten measurements of the width of a 5-μm transparent line of 0.03 to 0.09 μm (three sample standard deviations). The linearity of each of the microscope systems was checked for gross misbehavior by measuring four line spacings after calibration with the NBS line-standard interferometer [82]. Within the measurement repeatability and the calibration accuracy, no significant deviations from linearity were observed.

Cosine error results when the axis of measurement is not perpendicular to the line whose width is to be measured. In a filar eyepiece, cosine error is minimized when the crosshair lies parallel to the line and travels perpendicular to it. In the shearing eyepiece, the direction of shear must also be perpendicular; similarly with a TV-microscope system. For filar and image-shearing eyepieces, the degree to which the line to be measured can be made to lie along the axis of measurement depends on the fraction of the field of view the line occupies and the least detectable increment of field of view between some part of the line and a reference mark on the viewer. A series of experiments showed that, provided the line fills at least 5 to 10 percent of the field, misalignment need not be a significant source of measurement error.

Detailed line-width measurements were made with each of the systems on transparent lines of 2-, 5-, and 10-μm nominal width in an opaque field. Each microscope was calibrated in magnification using a line spacing previously measured to be 34.927 ± 0.007 μm with the NBS line-standard interferometer [82]. In addition, the TV-microscope system was adjusted to measure a line-to-space ratio of a value predetermined by an artifact supplied by the manufacturer.

The results of the measurements appear in table 13. Each of the entries in the table represents the mean of ten measurements taken one after another. To determine how much significance can be attributed to each entry, measurements on each of three systems were repeated ten times successively on nine occasions for measurements of the 5-μm line in bright-field transmitted illumination. Typical data for a series of ten measurements on a single occasion are summarized in table 14 which also shows the arithmetic means and sample standard deviations of the means for nine such series taken on different occasions.

The spread in the means of measurements taken on different occasions cannot be explained by the spread within measurements on one occasion. If the standard deviation associated with n repetitions of a measurement made on a single occasion is σ_w, the sample standard deviation of the means of these n repetitions taken on a number of occasions is a measure of the total standard deviation [83]:

$$\sigma_{total} = \sqrt{\sigma_B^2 + \frac{\sigma_w^2}{n}} ,$$

where σ_B^2 is the between-laboratory component of the variance. The reproducibility can be defined as the spread about the grand mean which includes 95 percent of all test results. The reproducibility associated with test results based on a single measurement on each occasion is therefore [83]:

$$\text{Reproducibility} = \pm 2.77\sqrt{\sigma_B^2 + \sigma_w^2} .$$

The results of the study above suggest that the reproducibility is about ±0.3 μm for the filar eyepiece and about ±0.1 μm for both the shearing eyepiece and TV-microscope system. Therefore, it can be concluded that the discrepancies between measurements made on the same line with different microscopes and illuminations are statistically significant.

(F. W. Rosberry[#] and D. A. Swyt[#])

Table 13 — Apparent Widths of Clear Lines in an Opaque Field

Microscope	Apparent Line Width, μm		
a. Bright-Field Transmitted Illumination:			
Filar Eyepiece	2.25	5.25	10.05
Shearing Eyepiece (Intensity)	1.95	4.65	9.10
Shearing Eyepiece (Polarization)	2.00	4.85	9.40
TV Display	2.55	5.35	9.75
b. Bright-Field Reflected Illumination:			
Filar Eyepiece	2.15	5.00	9.80
Shearing Eyepiece (Intensity)	2.45	5.35	9.75
Shearing Eyepiece (Polarization)	2.50	5.40	9.90
TV Display	2.55	5.25	9.75
c. Dark-Field Transmitted Illumination:			
Filar Eyepiece	2.10	4.80	9.30
Shearing Eyepiece (Intensity)	2.15	5.15	9.65
d. Dark-Field Reflected Illumination:			
Filar Eyepiece	2.25	5.15	9.50
Shearing Eyepiece (Intensity)	2.25	5.20	9.55

Table 14 — Representative Data for Line-Width Measurements Repeated on the Same Line

Microscope		Filar Eyepiece	Shearing Eyepiece (Intensity Type)	TV Display
Typical Results of Ten Measurements on Same Occasion	Mean, μm	5.25	4.65	5.40
	Sample Std. Dev., μm	0.077	0.014	0.009
Average Sample Std. Dev., μm		0.078	0.015	0.010
Mean of Means of Ten Measurements on Nine Occasions	Mean, μm	5.22	4.65	5.40
	Sample Std. Dev., μm	0.072	0.034	0.028
Reproducibility, μm		0.28	0.10	0.08

6.5. Line-Width Measurement by Diffraction Pattern Analysis

A study was undertaken to delineate the tolerances, design criteria, and limitations associated with the measurement of line widths by analysis of the diffraction pattern. The instrument for performing this measurement is shown schematically in figure 43 [84]. A laser beam is shaped into a line by means of two cylindrical lenses, C_1 and C_2, and is focused on the plane, P, through an adjustable aperture slit A. The specimen to be measured is placed at the focus of the slit image, S, formed by a spherical 50x microscope objective lens with a numerical aperture of 0.85. This lens also serves to focus the effective source, P, on a diode array, D, located an appropriate distance behind the specimen.

In this arrangement, the diffraction pattern in the plane of the diode array is given by the convolution of the source image with the object transform. In the case of a gap of width w in an opaque background in the object plane (fig. 44a) with ideal transmission characteristics (fig. 44b), the object transform is given by $w\sin(\pi fw)/(\pi fw)$ (fig. 44c). The intensity distribution of this diffraction pattern (fig. 44d) is measured and digitized (fig. 44e), and a discrete Fourier transform is computed (fig. 44f). The intercept of this autocorrelation function on the horizontal axis occurs a distance w from the origin. When the instrument is used to measure opaque lines, it is necessary to consider the image of the aperture slit which surrounds the line in the object plane. In this case, provided that the line is reasonably well centered in the image of the slit, the autocorrelation function has a region of positive slope to the right of the vertical axis which, when extrapolated back, intercepts the horizontal axis a distance equal to the width of the line from the vertical axis [85].

Experiments were carried out to determine the sensitivity of the system to focus, aperture size, source intensity, the nature of the object measured (line or gap), and the width of the object. The measurement process was found to be sensitive to the centering of the line in the aperture, the aperture width relative to the line width, and focus and location of the aperture. In addition, a theoretical analysis showed that if the optical density of the opaque regions is less than 3.0 the positions of the intercept can be significantly different from that expected on the basis of ideal considerations. Variations in the intensity of the illuminating laser do not appear to affect the measurement.

Better linearity and repeatability were achieved for measurement of opaque lines in a clear field than for measurement of clear gaps (or slits) in an opaque field. This appears to be due in part to the different criteria used for centering the aperture on the object plane; the criterion used in the case of opaque lines is both more sensitive and more repeatable.

Analysis of the optical system shows that the system response depends on the uniformity and phase of the aperture illumination and on the numerical aperture and quality of the objective lens as well as the characteristics of the line or gap being measured. Anomalies which have been noted in the autocorrelation functions suggest that additional analysis and instrumental improvements are required to

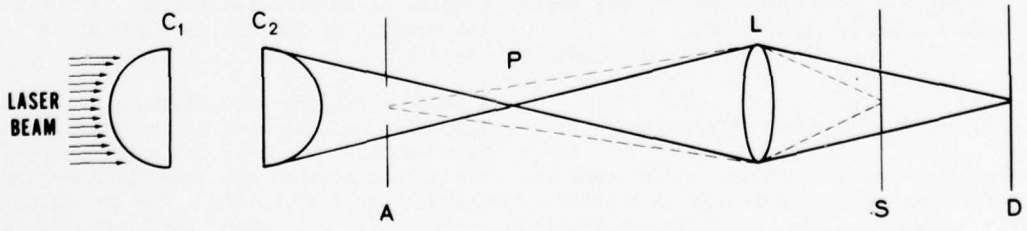

A Adjustable aperture slit
C_1, C_2 Cylindrical lenses
D Diode array
P Focal plane of source
S Specimen, focal plane of slit

Figure 43. Schematic representation of optical system for diffraction pattern analysis.

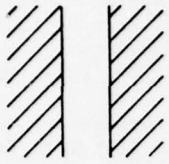

a. Gap of width w.

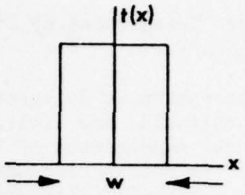

b. Transmission function of gap (t(x) = 1 for x between ±w/2, 0 elsewhere).

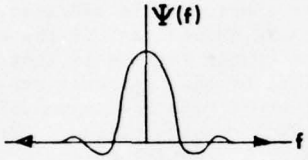

c. Optical Fourier transform of gap ($\Psi(f) = w(\sin\alpha)/\alpha$, where $\alpha = \pi fw$).

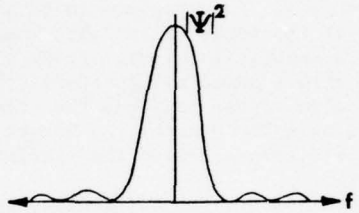

d. Transform intensity ($|\Psi(f)|^2$).

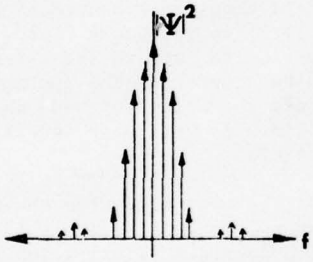

e. Discrete sampling of transform intensity.

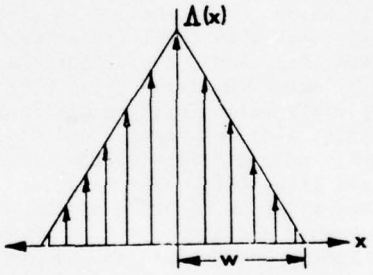

f. Inverse transform of $|\Psi(f)|^2$ ($\Lambda(x) \propto 1-|x/w|$ for x between ±w, 0 elsewhere).

Figure 44. Schematic flow diagram for estimation of width of gaps.

interpret accurately widths of lines less than 2.5 μm wide. Various instrumental modifications are being considered.

(H. L. Kasdan[×])

6.6. Automated Photomask Inspection

Detailed analyses of the state-of-the-art automated technologies previously identified (NBS Spec. Publ. 400-4, pp. 49-50) as applicable to inspection of photomasks for defects were completed. In this work the basic physical principles on which these technologies are based were analyzed, limitations of each of these technologies were identified, the approximate times necessary for inspection of defects on a 76- by 76-mm photomask with 3.8- by 3.8-mm die patterns were calculated and problem areas were identified. A summary of the results of the analyses are given in table 15.

A basic criterion used in these analyses was that 2-μm defects must be detected (NBS Spec. Publ. 400-17, p. 32). The approach used in the calculation of the time for 100-percent inspection of a photomask was to calculate the sampling rate which is the maximum number of 2- by 2-μm areas that can be inspected per second. Total inspection times were calcu-

[×]Work performed at Recognition Systems, Inc. under NBS Contract No. 5-35890. NBS contact for additional information: D. B. Novotny.

Table 15 — Characteristics of Automated Photomask Inspection Techniques

Technique	Inspection Sampling Rate, s^{-1}	Total Inspection Time, h:min	Required Alignment or Indexing Accuracy, μm	Estimated Cost, k$
Optical Overlay	4.0×10^6	0: 5	±1	150
Spatial Filtering	NA	∿0: 5	NA	50
Dual-Beam Flying Spot Scanner	3.5×10^6	0: 7½	±0.2	150
Single-Beam Flying Spot Scanner	2.0×10^5	∿2:10	±1	500
Microdensitometer	1.5×10^4	∿26: 4	NA	150
TV-Microscope	1.2×10^6	∿0:40	±0.4	130

lated from this fundamental sampling rate on the basis of 1.44×10^9 such areas on a 76- by 76-mm mask, plus all the additional times that are needed to completely scan the masks. The total inspection times, listed in the table, do not include loading times. The estimated costs listed in the last column are primarily based on estimates given by persons working with similar equipment and should be interpreted only in an approximate comparative sense.

In the *optical overlay method* two die patterns are viewed simultaneously through two microscope objectives, typically of 10x magnification. This technique has been used for many years for visual observation of the registration of the different layers in a mask set. In an automated version, pattern information from the same coordinate position on two die patterns is read by two identical in-line diode or CCD arrays [86-88]. The signal from each device in one of the arrays is subtracted from the corresponding signal on the other array. Resultant differences are interpreted as defects. For the analysis it was assumed that each array consisted of 512 devices in an area 13 mm long by 25 μm wide and that scanning and inspection occur simultaneously and continuously. For a typical array scanning rate of 4×10^6 devices per second, the entire array can be scanned once while the stage, traveling at 20 mm/s, advances 2.5 μm, the width of the area observed by the array. These conditions imply that one scanning sweep across the mask can be made every 3.8 s and that the entire mask can be scanned in 59 sweeps. Under these conditions the total inspection time is less than 5 min which includes about 1 min for reversing the stage motion and indexing the scan.

One serious problem with this method is the critical alignment required between the two die patterns being inspected. Misregistration resulting from various sources, such as run-out errors between the dice in the mask, lack of consistency in line widths, and yaws in the stage motion of the inspecting device, can cause differences in the outputs that are erroneously interpreted as defects. The 2-μm defect detection criterion requires that the two patterns be in register with deviations nowhere greater than ±1 μm. In addition, the method requires intense illumination, and, in common with all directly comparative technologies, it is insensitive to any defect which appears on all die patterns.

The *spatial filtering method* is based on the property that for coherent light the Fraunhofer diffraction pattern of the object, which is represented by the optical Fourier transform of the object, is produced by a lens at the focal plane of the radiation source. Therefore, if a photomask is placed in front of a lens and illuminated by a collimated laser beam, the Fourier pattern of the object is produced behind the lens at the focal plane of the source (cf. secs. 6.1. and 6.5.). If a mask that blocks the light radiation produced by the desired mask pattern geometry is placed at this focal plane, only the diffraction pattern produced by defects passes through this filter. These diffraction patterns may be reconstructed by means of a second lens to form a real space mapping of the defects.

While this technique appears straightforward, it is not practical for the detection of 2-μm defects. Both variations in the refractive index of the glass larger than 1.6×10^{-4} or thickness variations greater than 0.17 μm are sufficient to distort the diffracted wavefronts by a half wavelength and prevent the expected interference effects. Although the surface irregularity problems can be alleviated through the use of liquid gates, this creates contamination and cleaning problems which are more severe than the original defect problems. In addition, the filters must also be made with tolerances tighter than those with which the photomasks being inspected are made. This technique is further hampered by focusing problems and difficulties encountered in registering the filter with the transformed image.

With the *dual-beam, flying-spot scanner*, the transmittances through equivalent portions of two die patterns illuminated by two simultaneously scanning laser beams focused to a spot size of about 3 μm are compared. A difference in the transmission is interpreted as a defect.

This technology has been developed and a working prototype exists [89]. Although the time required to actually inspect a 76- by 76-mm mask is only slightly greater than 7 min, an additional period of about the same time is required for loading the mask and registering the two beams. The beam registration is held to 0.2 μm; misregistrations as large as 0.4 μm, caused by step and repeat errors or edge raggedness, do not register spurious defects. As in the case of the optical overlay method, this technique is not sensitive to defects repeated on each of the die patterns.

In each of the other three technologies analyzed, the information from each die pattern is digitized and compared with information representing the ideal or true mask pattern which is stored in the memory of a computer. These techniques are limited by the data transfer rate and require a high speed computer as an integral part of the equipment. Since the storage requirements for a 3.8- by 3.8-mm die are well within the capabilities of a computer system with digital disk storage and an 8.7-MHz bit transfer rate, the criteria of word transfer rate and needed bits per word can be used to select viable combinations.

With a *single-beam, flying-spot scanner*, a 2-μm diameter light spot is scanned over the pattern and the transmitted intensity is recorded with a photomultiplier tube. The spot may be generated either by a laser or a cathode ray tube (CRT). The accuracy and speed of the optical density measurement depends on the time response of the photomultiplier and the number of detectable grey levels. A CRT flying-spot detector utilizing a 5-μs dwell time per inspection point for beam indexing and stabilization and a four-level grey scale was assumed for the analysis. These conditions can be satisfied by commercially available cathode ray tubes with a 76- by 76-mm screen and a square matrix of 1.6×10^7 accessible points. If these points are serially focused on a mask through a 10x reduction lens, it takes 80 s to scan each 7.6- by 7.6-mm field of view which includes four complete 3.8- by 3.8-mm die patterns. Since there are 100 such fields of view on the mask, about 2¼ h are required for the inspection.

Microdensitometers are designed primarily to measure the optical density of a pattern as a function of position rather than to inspect for mask defects. To inspect for 2-μm defects, the die pattern must be scanned with a 2-μm spot in 2-μm swaths. If the stage travels at the highest practical velocity of 30 mm/s, a data acquisition rate of 1.5×10^4 words per second is required. This in turn requires a photomultiplier response time of less than 70 μs for accurate optical density mapping. If these conditions can be achieved, the scan time per individual die pattern, not including stage indexing time, is about 4 min. The total time to inspect the 400 die patterns on the mask is about 26 h.

There exists the possibility of reducing this scan time by scanning with a rectangular aperture. If a 2- by 100-μm aperture is used the inspection time could be reduced by a factor of 50 to about 32 min. However with this approach, serious questions arise concerning the response time of the photomultiplier and its ability to make accurate density measurements under these conditions. Furthermore, the integrated intensity over a 2-μm scan length is changed by approximately 1 percent for every 0.02 μm of misregistration of any transparent to opaque edge extending the length of the aperture. This effect combined with those from scanning table yaws, die runout, and other registration errors commonly found in photomasks would lead to the detection of copious spurious defects.

The analysis of the *TV-microscope method* has been reported in detail (NBS Spec. Publ. 400-17, pp. 32-36). The results listed in table

15 are for the case of a vidicon tube which scans one 0.4- by 0.4-mm field of view in 1/15 s.

The only two inspection systems commercially available at the present time are modifications of systems that were developed for other purposes. One, a TV-microscope system, was originally designed to scan films of rocket launches. It is a defect inspection system, but its slow speed is a major factor inhibiting use. The second, a microdensitometer, was originally designed to scan astronomy films. It is most widely used for dimensional analysis of photomasks. Other defect inspection systems have been developed by several large corporations but these are not available on the commercial market.

Masks can also be inspected for dimensional errors with the systems analyzed above. Two basic limitations common to all approaches are the dependence on suitable line-width standards and the need for a thorough understanding of the optical system employed. It was concluded from this work that the search for dimensional errors and the search for defects differ significantly, and that these functions should be performed independently. Speed is the most important consideration in the automated search for visual defects; the analyses showed that few systems as presently envisioned have economically attractive inspection times.

To provide a means for evaluation of various automated mask inspection systems, work was initiated on the design and fabrication of a test mask with intentionally added defects. This can be used to determine the minimum detectable defect size, inspection speed, missed defects, false indications, and differences in observation of pinhole and spot defects. In addition to comparing the characteristics of different machines, such a mask can also be used on a regular basis to verify the performance of an operating system [89].

An MOS metallization pattern of moderate complexity was chosen as the basis for this test mask. The smallest line widths or spaces in this pattern are 0.30 mils (7.6 μm). The width of the pattern is 10.5 mils (0.27 mm) and the height is 7.9 mils (0.20 mm). Each die consists of a 10 by 10 array of this basic pattern. The final mask consists of a 14 by 14 array of dice with a center-to-center spacing of 150 mils (3.81 mm) in each direction. Of the 196 dice in the array, 15 contain intentional defects.

These 15 defective dice are inserted into the array by the use of three extra 10x reticles each of which contains 36 intentionally introduced defects including pinholes, spots, breaks, bridges, intrusions, and protrusions located in different parts of the pattern. Each of these reticles is stepped into the array at five different places, more or less randomly located, so that each mask contains 540 defects. Since the area covered by the 14 by 14 array is 28.5 cm^2, the defect density is about 19 cm^{-2}.

Initial versions of these test masks have been fabricated and are being evaluated. Preliminary test results suggest that although not all of the smallest pinholes and spots printed, a range of defects down to about 2 μm is available on the mask. It is intended that these test masks be subjected both to additional visual inspection and to inspection on various automated inspection systems at cooperating laboratories in order to characterize them more fully and evaluate their utility. (D. R. Ciarlo[+], P. A. Schultz[+], and D. B. Novotny)

[+]Lawrence Livermore Laboratory, Livermore, California 94550. Work conducted under NBS Order No. 503183.

7. TEST PATTERNS

7.1. Square Array Collector Resistor

The square array, four-probe, collector resistor structure (NBS Spec. Publ. 400-17, pp. 25-26) [21] was further analyzed for the case where the probe spacing is comparable with the lateral dimensions of the specimen. It was assumed in the analysis that the specimen is square, has nonconducting boundaries, and is thin with respect to the probe spacing, and that the probe contacts lie on specimen diagonals. This configuration is one which may be encountered in measuring the sheet resistance of the collector region of an integrated circuit.

An early attempt to solve this problem [90] was incorrect because the solution does not approach the van der Pauw [91] solution for the case where the probes are on the periphery of the specimen. Other early solutions based on conformal transformation [92] and the method of images [93,94] are correct but the results were not presented in a convenient form for engineering use. The present solution is based on the method of images in a complex plane. The results are expressed in the form of algebraic equations which are easy to evaluate and converge rapidly.

The geometry analyzed is shown in figure 45. The current was assumed to be two-dimensional in the plane of the specimen. The current carrying probes were assumed to be a point source and a point sink so that the boundary conditions can be satisfied by a system of images placed symmetrically about the boundaries. Complex variables theory was used to solve for the potential difference, $V_1 - V_2$. Omitting the details of the solution, the result is:

$$V_1 - V_2 = (\rho I/2\pi w)C$$

where

$$C = \ln\frac{(\cosh x+1)(\cosh x-\cos x)}{2(1-\cos x)} + (-1)^m \sum_{m=1}^{\infty} \ln\frac{(\cosh x+\cosh a)^2[(\cosh x-\cosh a\cos x)^2+\sinh^2 a\sin^2 x]}{(\cosh a+1)^2(\cosh a-\cos x)^2} ,$$

$a = m\pi$, and $x = s\pi/d$.

This result goes to the proper limits for the cases where the specimen is an infinite sheet ($d >> s$) and where the probes are on the periphery of the specimen ($d = s$). In each of these cases the series in the expression for C is identically equal to zero. In the former case, C approaches ln2; this is the result found by Uhlir [95] for a square four-probe array on an infinite sheet with a nonconducting back side (NBS Spec. Publ. 400-25, pp. 39-40). In the latter case, C approaches 2ln2; this is the symmetrical van der Pauw solution [91]. When neither limiting case applies, C can be computed to an accuracy of 0.1 percent with the use of only the first three terms in the series.

Correction factors can be applied to the limiting cases to determine the region over which the limiting case expressions are valid. When $d >> s$, the resistivity is given by

$$\rho_\infty = \frac{V_1-V_2}{I}\frac{2\pi w}{\ln 2} . \qquad (13)$$

For large, but finite, ratios of d to s, a correction factor $C_5 = C/\ln 2$ can be calculated such that

$$\rho = \rho_\infty/C_5 . \qquad (14)$$

The percentage error introduced by using the uncorrected value ρ_∞, is

$$\varepsilon_\infty = 100(\rho_\infty - \rho)/\rho = 100(C_5 - 1) . \qquad (15)$$

For $d/s \geq 23$, the uncorrected value exceeds the true value by less than 1 percent.

When $d \simeq s$ the resistivity is

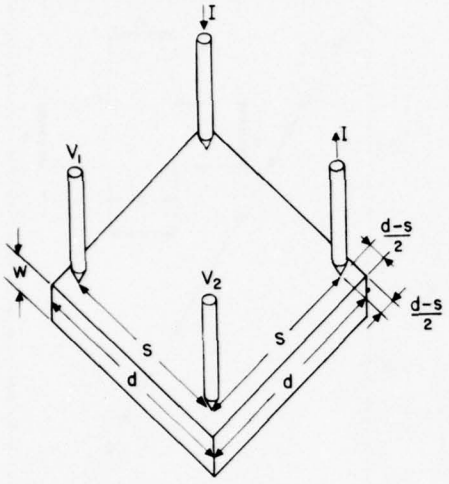

Figure 45. Arrangement of a square four-probe array on the diagonals of a thin, square specimen.

$$\rho = \rho_1/C_6 \qquad (16)$$

where $\rho_1 = 2\rho_\infty$ and $C_6 = C/2\ln 2$. In this case the percentage error introduced by using the uncorrected value, ρ_1, is

$$\varepsilon_1 = 100(\rho_1 - \rho)/\rho = 100(C_6 - 1) \; . \qquad (17)$$

For d/s between 1.0 and 1.35 the uncorrected value is less than 1 percent below the true value. The correction factors C_5 and C_6 and the errors ε_∞ and ε_1 are tabulated in table 16.

These results can also be extended to other cases. The present results are approximately correct for the case in which the probe locations are rotated away from the diagonals of the square even for small values of d/s [92-94]; the differences are such that ρ_1 approximates the true resistivity for somewhat larger values of d/s. For example, for d/s = 1.5,

Table 16 — Correction Factors for a Square Four-Probe Array on a Thin Square Specimen

d/s	C_5	ε_∞	C_6	ε_1
1.0	2.0000	100.0	1.0000	0.0
1.1	1.9997	100.0	0.9999	0.0
1.2	1.9967	99.7	0.9984	0.2
1.3	1.9880	98.8	0.9940	0.6
1.4	1.9721	97.2	0.9860	1.4
1.5	1.9491	94.9	0.9745	2.6
1.6	1.9199	92.0	0.9600	4.0
1.7	1.8862	88.6	0.9431	5.7
1.8	1.8493	84.9	0.9247	7.5
1.9	1.8107	81.1	0.9054	9.5
2.0	1.7716	77.2	0.8858	11.4
3.0	1.4500	45.0	0.7250	27.5
4.0	1.2773	27.7	0.6386	36.1
5.0	1.1849	18.5	0.5924	40.8
7.0	1.0977	9.8	0.5488	45.1
10.0	1.0487	4.9	0.5244	47.6
15.0	1.0219	2.2	0.5109	48.9
20.0	1.0123	1.2	0.5062	49.4
25.0	1.0079	0.8	0.5040	49.6
30.0	1.0055	0.6	0.5027	49.7
∞	1.0000	0.0	0.5000	50.0

the value of C_6 for the case of 45 deg rotation, so that the probes lie on the bisectors of the sides of the specimen, is 2.2 percent larger than the value for the probes on the diagonals. In addition, similar techniques can be used to solve the problem of a square array on a rectangular specimen.

(M. G. Buehler and W. R. Thurber)

7.2. Sheet Resistor Test Structures

Additional analysis of cross-type sheet resistor test structures was completed. These analyses were carried out with the use of the same numerical analysis used previously in the analysis of orthogonal quadrate crosses and offset quadrate crosses (pinwheels) (NBS Spec. Publ. 400-19, pp. 44-45) [96]. Two limiting cases of the cross structure were studied. The relative geometrical errors for these cases were determined by computing the true sheet resistance, R_s, and comparing it with the sheet resistance calculated from the symmetrical van der Pauw formula [91]:

$$R_s(vdP) = (\pi/\ln 2)(\Delta V/I), \qquad (18)$$

where $\Delta V = V_1 - V_2$ for a current I passed into I_1 and out of I_2 as shown in figures 46 and 47. The error, E, is defined as

$$E = [R_s - R_s(vdP)]/R_s \ . \qquad (19)$$

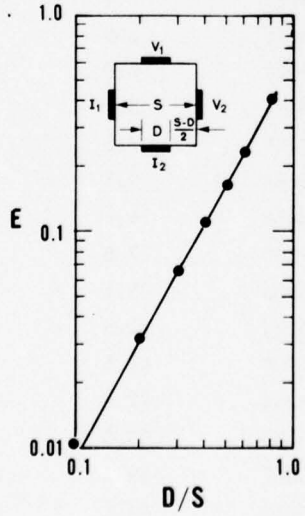

Figure 46. Normalized sheet resistance error resulting from shorting contacts on the periphery of a square test structure.

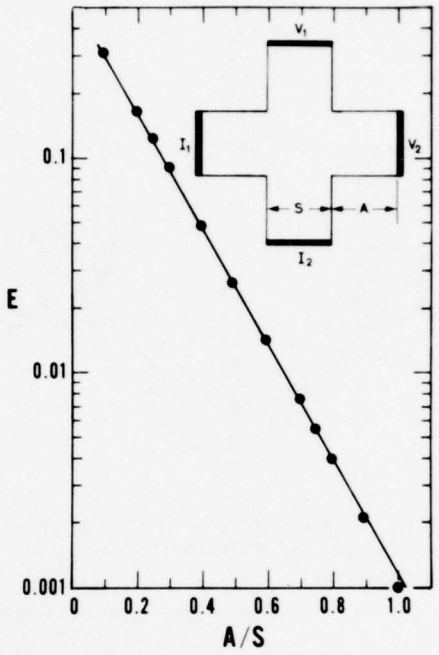

Figure 47. Normalized sheet resistance error resulting from shorting contacts at the ends of the arms of a Greek cross test structure.

One limiting case, where the arm length is zero, is illustrated in figure 46. Over most of the range the error is found to fit the empirical relation

$$E = (0.595 \pm 0.015)(D/S)^{1.82 \pm 0.03} \ . \qquad (20)$$

When D/S = 0, this case reduces to the symmetrical van der Pauw structure and the error goes to zero. If D/S < 0.1, the geometrical error associated with this structure is less than 1 percent. The integral equations for this limiting case had been formulated by Wick [97] but he did not solve and evaluate the equations.

Another limiting case, where D = S, is the Greek cross.* This is illustrated in figure 47. Except for a very short arm length (A/S < 0.1), the error is found to fit the empirical relation

*The conclusion that the Greek cross is a van der Pauw structure was reached intuitively and independently by W. E. Ham, RCA Laboratories (private communication).

$$E = (0.590 \pm 0.006)\exp[-(6.23 \pm 0.02)A/S]. \quad (21)$$

When $A/S > 0.65$, the geometrical error associated with this structure is less than 1 percent. If $A/S > 1.02$, which is easily achieved in practice, the error is less than 0.1 percent.

The technological implication of this test structure is found in the realization that the sheet resistance of a very small region can be accurately measured because the width of the arms of the Greek cross is limited only by the minimum line width achievable by the photolithographic technology utilized in device fabrication.

(M. G. Buehler and J. M. David)

7.3. Test Pattern for TTL Technology

One approach to assurance of built-in component reliability involves the use of a process validation wafer (PVW). This type of wafer is intended to evaluate process and circuit parameter uniformity, and to measure the occurrence of random faults. The PVW is an entire wafer of test structures and is intended to be fabricated along with product wafers on a periodic basis. This approach is a supplement or alternative to a test pattern substituted for an IC chip on a product wafer. As a process characterization tool the PVW can be used to qualify vendors and can serve as a circuit acceptance criterion. The PVW concept has the potential of greatly reducing the user-imposed requirements that now accompany a high-rel component purchase. Various forms of this approach are currently being used by the British Post Office [98] and by a few U.S. Government agencies in the procurement of reliable, custom components.

As an illustration of a microelectronic test pattern under development for use as a process validation wafer, consider the TTL test pattern shown in figure 48. This pattern consists of various test structures which are intended to be tested electrically with a high-speed dc wafer tester. The test structures are arranged so that all structures can be probed by a 2 by 10 probe array (NBS Spec. Publ. 400-25, pp. 41-43). This modular arrangement allows the structures to be called from a computer library and arranged quickly into a new test pattern to fit available space. In addition, the modular concept allows for standardization of each test structure in its entirety including its probe pads which must be an integral part of the test structure.

The TTL pattern is divided into quadrants, each 1.7 mm (67 mil) by 1.3 mm (51 mil). The lower left quadrant contains strings of contacts and metal runs of varying length over oxide steps. The lower right quadrant contains multi-emitter transistors of varying size. These structures are intended to check for random faults such as contact window problems, incomplete metal coverage, and emitter-collector shorts (pipes). The two upper quadrants contain process control structures, circuit elements (both transistors and resistors), and NAND gates. Among the process control structures are several versions of the cross sheet resistor (see sec. 7.2.).

At the present time artwork for the mask set for this test pattern is being prepared. On completion of the mask set, wafers are to be fabricated and correlations established between the properties of appropriate test structures and the circuit characteristics.

(D. E. Sawyer, D. A. Maxwell, J. M. David, and M. G. Buehler)

7.4. Test Pattern Design and Analysis for SOS/LSI

The mask set for the SOS/LSI test pattern (NBS Spec. Publ. 400-25, pp. 44-45) was completed and two initial lots of wafers were processed with the previously outlined single-epitaxial, p^+-polysilicon gate process. Preliminary observations were made on some of the optically accessible structures in the type V pattern and on the p-channel transistor in the type II pattern (NBS Spec. Publ. 400-19, p. 47).

The two-level interaction test structure for p^+-polysilicon over epitaxial silicon is shown in figure 49. The structure consists of polysilicon lines of various widths extending from the sapphire up onto a silicon island. The design line widths (in mils; 1 mil ≈25 μm) are indicated outside the pattern. It can be seen that no polysilicon remains for designed dimensions of 0.1 mil (2.5 μm) or less. This suggests that the polysilicon lines are smaller than their designed dimensions by about 0.05 mil (1.2 μm) on a side. It can also be seen directly that the dimensions on top of the epitaxial silicon and on top of the sapphire are nearly identical, that a severe distortion in the polysilicon occurs at the edge of the epitaxial silicon, and that a discontinuity in the polysilicon at the edge of the epitaxial silicon exists for lines with designed width of less than about 0.3 mil (7.6 μm).

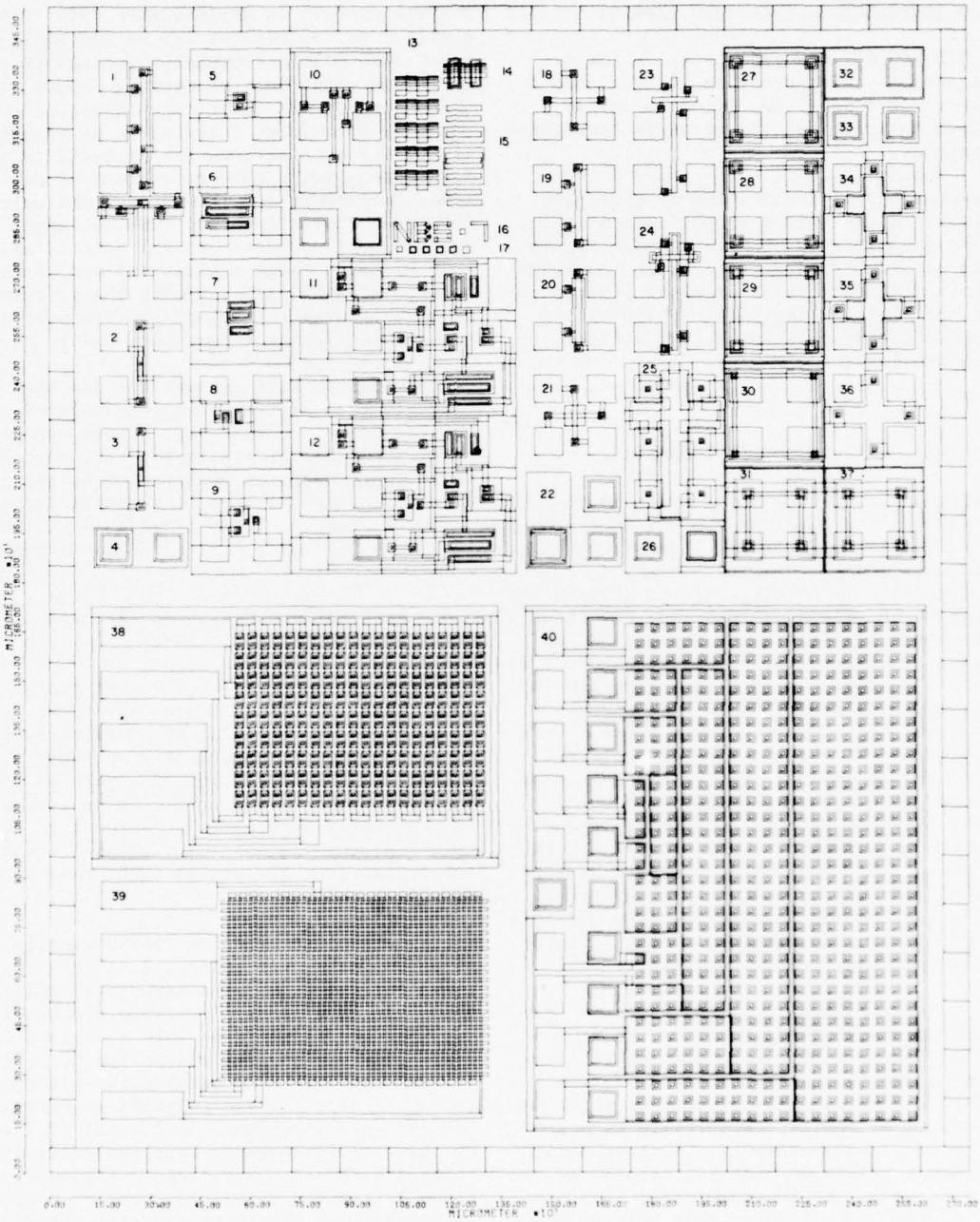

Figure 48. Junction-isolated TTL test pattern. (Upper left quadrant: process control structures, circuit elements, and NAND gates; upper right quadrant: process control structures; lower left quadrant: contact resistors and metal step coverage string; lower right quadrant: multi-emitter transistors.)

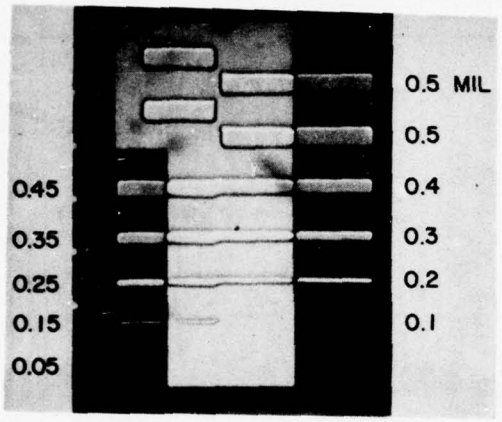

Figure 49. Two-level interaction test structure.

The two-level alignment test structure is shown in figure 50. This structure consists of a trapezoidal polysilicon region over a rectangular silicon island. It is clear that no difficulty exists in determining the intersection point where the trapezoid crosses the rectangle. The index markers are placed on 1.0-mil (25-μm) centers. The difference in intersection points on the two sides of the trapezoid in figure 50a is approximately 0.4 mil (10 μm) which corresponds to an actual misalignment of about 0.02 mil (0.5 μm). An orthogonal pair of structures can be used for complete alignment measurement as shown in figure 50b. Even when the edge crossing is not ideal, as shown in figure 50c, the crossing points can be determined quite precisely. The resolution of the structure appears from these results to be about 1 μin. (25 nm) when using an ordinary microscope. This structure can also be used as a very accurate ruler to measure the change in the lateral size of an object (such as a wafer) after some processing step or with temperature. In this case, the upper level would not necessarily be printed but could be simply observed.

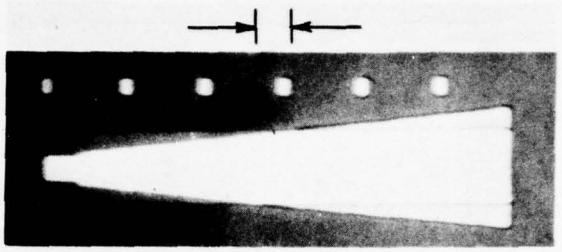

a. Single structure.

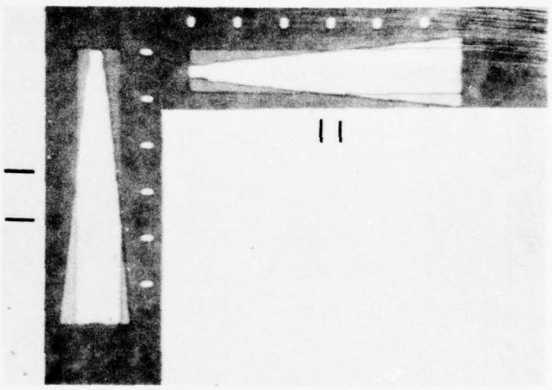

b. Orthogonal pair.

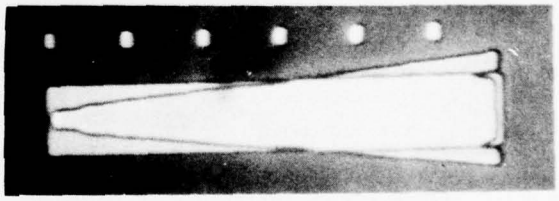

c. Single structure with non-ideal edge crossing.

Figure 50. Two-level alignment structures.

An example of some preliminary results from the type II tests is shown in figure 51. This plot shows the distribution of drain current for a p-channel transistor in saturation across approximately 1.5 in. (38 mm) of a 2-in. (51-mm) diameter wafer. Several very interesting features of these data are noted:

1. A significant number of the devices have no output on the scale used; there is a tendency for these zero-output devices to cluster together;
2. The distribution observed shows a very "fuzzy" nature;
3. Gradual trends in the data over relatively large distances are observed; approximately ±20 percent total variation is seen across the wafer for operating devices.

The interpretation of these data in detail is not clear at present, but the following comments are relevant.

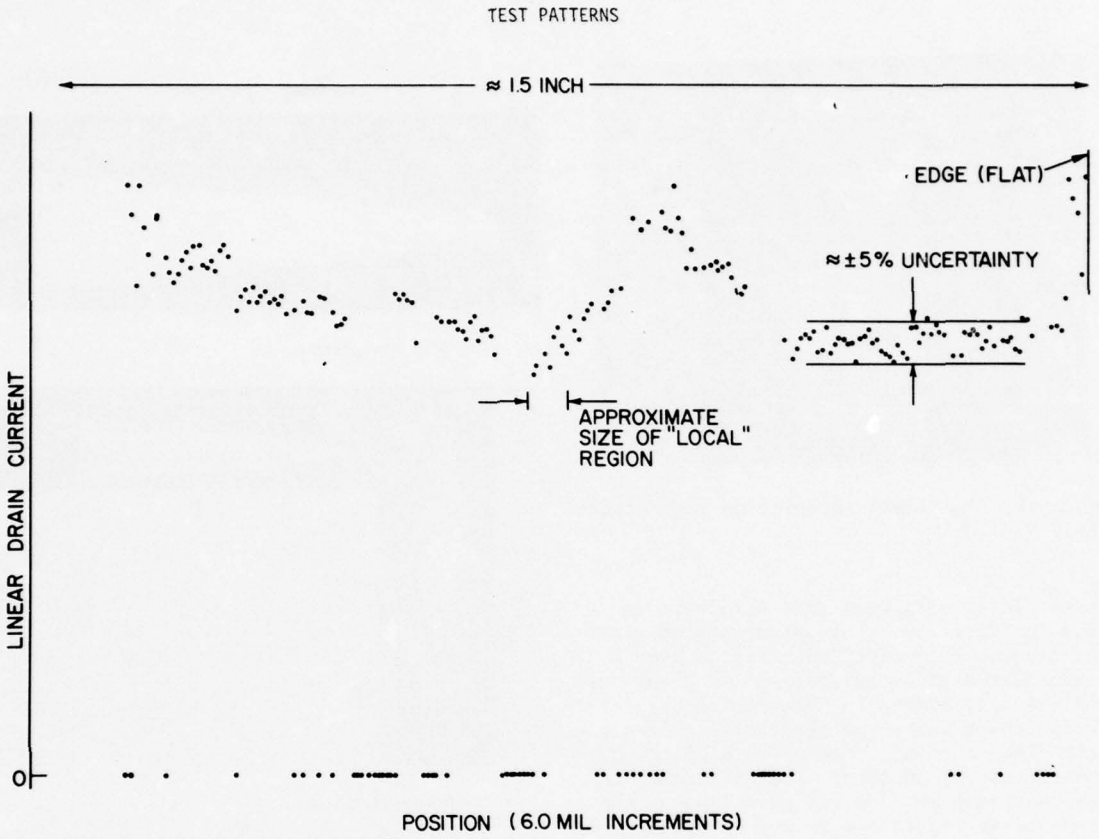

Figure 51. Distribution of *p*-channel saturation current in heavy inversion along the diameter of an SOS wafer perpendicular to the edge flat.

1. The zero-output devices are probably not caused by probing problems since low currents were detected on the same devices under different bias conditions. Furthermore, *n*-channel devices in the same row exhibited many fewer instances of zero-output devices.

2. The fuzziness is probably caused primarily by differences in the geometry of the channel regions.

3. Within a local area, approximately 50 mil (125 μm) in extent, an uncertainty of about ±5 percent exists.

Obviously, the most interesting observation here is the zero-output devices since these would be fatal to virtually any circuit. The personality of the system is readily apparent from data of this type taken over an extended region of the wafer which provides considerably more information than data on one or a small number of single devices. (W. E. Ham[+])

[+]Work conducted at RCA Laboratories under NBS Contract No. 5-35916. NBS contact for additional information: M. G. Buehler.

8. ASSEMBLY AND PACKAGING

8.1. Nondestructive Test for Beam-Lead Bonds

Detailed experiments were carried out to evaluate the acoustic emission test (NBS Spec. Publs. 400-12, pp. 31-32; 400-19, pp. 48-50; and 400-25, pp. 46-49) [99] as a nondestructive means for evaluating the quality of beam-lead and other types of multiple bonds. The measurement system is capable of detecting acoustic emission signals barely above the average noise level of the preamplifiers and considerably below various system and line transients. Most acoustic emission detector output signals produced in the present experiments were in the range of about 10 to 100 μV and were easily captured by the equipment. Because of the variety of gain adjustments possible (preamplifiers, pulse capturing equipment, and oscilloscope), the vertical scale of most acoustic emission oscillograms has no particular significance. The only important consideration is the signal-to-noise ratio, and this can be easily observed from the photographs. Signal sizes given in the discussion below refer to the detector output.

Pull Tests — In order to demonstrate the sensitivity of the method, several beam-lead devices were tested by cutting all but one of the beams and pulling the uncut beam to destruction with an electrolytically etched, 150-μm diameter tungsten hook inserted into a dab of silicone rubber on top of the device. Acoustic emission signals picked up by a substrate detector are displayed in figure 52. In the case of a well-bonded beam (fig. 52a), failure occurred by a break at the bond heel. The clipped waveform peaks indicate that the substrate detector output was significantly greater than 1 mV (peak-to-peak) during the initial part of the break. The signal from such breaks generally continues erratically for several times the time interval shown in the figure. In the case of a well-bonded beam with a weak anchor (fig. 52b), failure occurred by peel at the anchor at a force of about 30 mN (1 gf = 9.8 mN). The peak-to-peak detector output in this case was about 0.3 mV.

Pull tests were conducted on several well-bonded devices with weak anchors. A series of short bursts was observed starting at about 15 millinewtons per beam (about half the peel strength of the anchors). Similar well-bonded devices with strong anchors produced no signal until a pull force of about 25 millinewtons per beam was applied; the bursts in this case were longer and higher in amplitude than the devices with weak anchors. Several groups of commercially available devices from four different manufacturers were tested. Devices from three of these sources produced no acoustic emission signal until they were stressed to about 25 millinewtons per beam as noted above. However, devices from the fourth source produced large bursts of acoustic emission, such as those shown in figure 53a, when they were stressed to only about 10 millinewtons per beam; these bursts increased in number and amplitude with increasing stress. Examination of these devices in a scanning electron microscope following stressing to 10 millinewtons per beam revealed no evidence of mechanical failure. However, examination following stressing at about 25 millinewtons per beam revealed elongation of the beams, separation of the relatively thick titanium layer, peeling of the anchors, separation of the silicon nitride from the beams or silicon, and broken chips of silicon at the anchor as shown in figure 53b. Any of these observed degradations could be responsible for the acoustic emission signals. These problems can be attributed to design deficiencies; they were observed on three different device types from the same source on lots purchased 18 months apart. It should be noted that a normal destructive pull-off [100] or push test (NBS Tech. Note 806, pp. 34-35) would not have revealed any problems with the structures because the beams ultimately broke with forces typical of mechanically strong devices. The consequences of the poor mechanical integrity on device performance or reliability were not established.

In a large series of pull tests on devices bonded to substrates with chrome-inhibited bonding pads (NBS Spec. Publ. 400-25, pp. 46-47), it was found that a force of 10 to 15 millinewtons per beam was required to produce acoustic emission from one or two weakly-bonded beams on an otherwise well-bonded device. On the other hand, a force of only 5 to 10 millinewtons per bond was often sufficient to produce acoustic emission when all beams were poorly bonded; such devices would pull off completely at forces of 10 to 15 millinewtons per beam.

Push-Down Test on Devices Encapsulated in Silicone Rubber — Both well-bonded and poorly-bonded devices were encapsulated, except for the top of the chip, with a silicone rubber thinned with xylene [99] and allowed to cure. For testing, the device was mounted on a vacuum chuck and the top of the chip was uniformly pressed downward with an acoustic

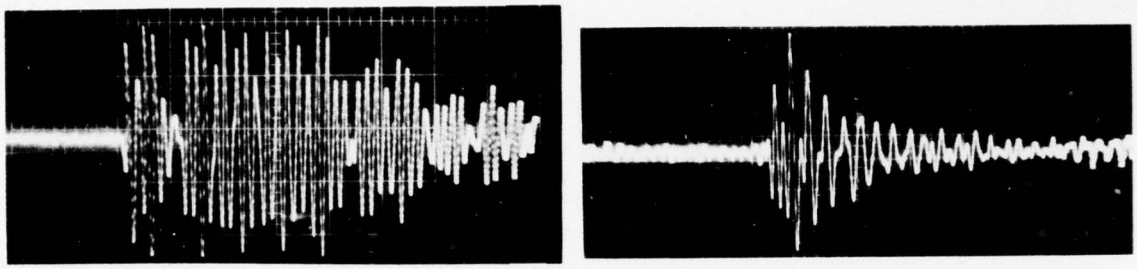

a. Well-bonded beam which failed by breaking at the heel at a force of about 35 mN. Horizontal scale: 20 μs/div.

b. Well-bonded beam which failed by peeling at the anchor at a force of about 30 mN. Horizontal scale: 16 μs/div.

Figure 52. Acoustic emission signals from single beams pulled to destruction.

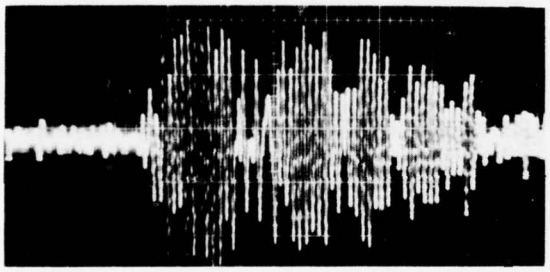

a. Acoustic emission signal at a pulling force of about 12 millinewtons per beam. Horizontal scale: 20 μs/div.

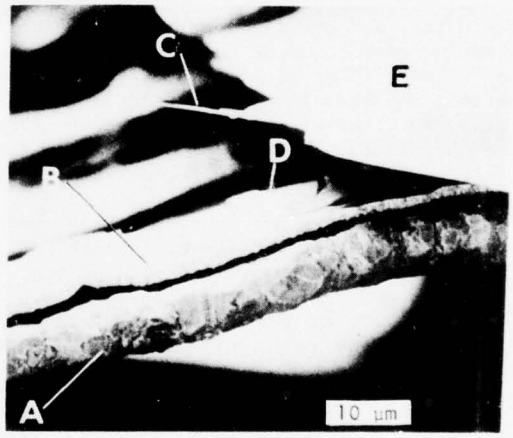

b. Scanning electron micrograph following application of a pulling force of about 25 millinewtons per beam.

A Gold beam
B Separated titanium layer
C Silicon nitride
D Broken piece of silicon
E Portion of silicon chip

Figure 53. Beam-lead device with poor mechanical integrity.

emission probe coated with silicone rubber and mounted in a force gauge as shown in figure 54. Well-bonded devices with good mechanical integrity required forces greater than 4.4 N on a 16-beam chip before producing acoustic emission bursts; well-bonded devices with poor mechanical integrity required 1.9 to 2.4 N. Devices of both types which had one or more weak bonds generally emitted their first bursts at forces of 0.5 to 1.5 N.

Application of Force to Beams Only — Two probes, tipped with silicone rubber and designed to avoid contact with the chip, were used to apply a downward force on the horizontal portion of the beam which extends outward from the chip. Simple resolution-of-forces analysis of a single beam indicates that nearly all the force is applied as a torque which tends to peel the anchor. Thus, probing a single beam or a single row of beams along one side of the chip provides an anchor adherence test; if all beams are probed simultaneously, the torque cancels and the force is applied only to the bond system.

Individual beams were probed with a tungsten carbide probe, which had a 75-μm diameter flat region tipped with silicone rubber and a lead-zirconate-titanate type acoustic emission detector, in order to establish emission patterns for both anchor and beam failures.

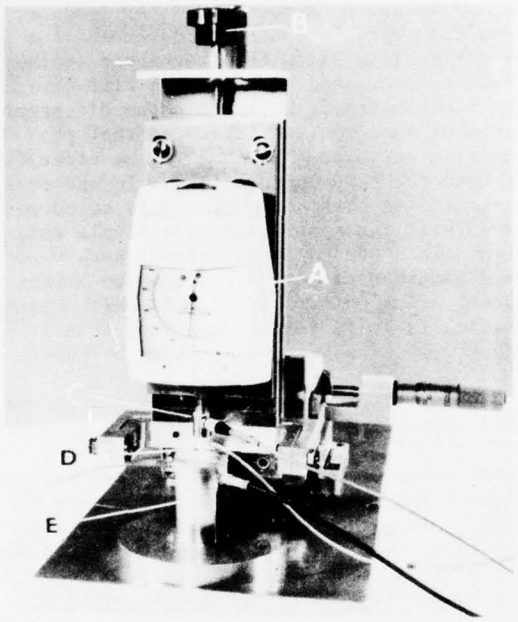

A Force gauge
B Force angle control
C Probe acoustic emission detector
D Acoustic waveguide and force probe
E Substrate holder with vacuum hold down and substrate acoustic emission detector

Figure 54. Apparatus for applying upward or downward force on beam-lead devices and for detecting any resulting acoustic emission.

Acoustic emission traces from the probe and substrate detectors are shown for typical cases in figure 55. The traces resulting from application of a downward force of about 20 mN to a beam with a weak anchor are shown in figure 55a. This anchor ruptured at an applied force of about 34 mN; a well-bonded beam with a strong anchor would typically curve downward until it touches the substrate at an applied force of 60 to 100 mN. For anchor failures, the probe detector usually produces the larger signal as shown in the figure. When a very weak bond is probed with a force of 30 to 40 mN, the signal intensities are usually reversed, as shown in figure 55b. Although these patterns are typical, it should be noted that these failure modes may at times produce entirely different patterns.

Some experiments were performed using the single probe to search for acoustic emission from silicon nitride fractures. In general, signals from fracture of thin (~200 nm) silicon nitride skirts were not detected because the emission is thought to occur at higher frequencies and because the coupling into the chip and substrate is poor. This was verified by coating a single beam probe with viscous acoustic coupling compound and moving it sideways into an extended silicon nitride skirt. A small acoustic emission burst was recorded in the probe detector (operating at 1.1 MHz) but not in the substrate detector (operating at 375 kHz).

Experiments were also carried out using as a probe a modified beam-lead bonding tool. The

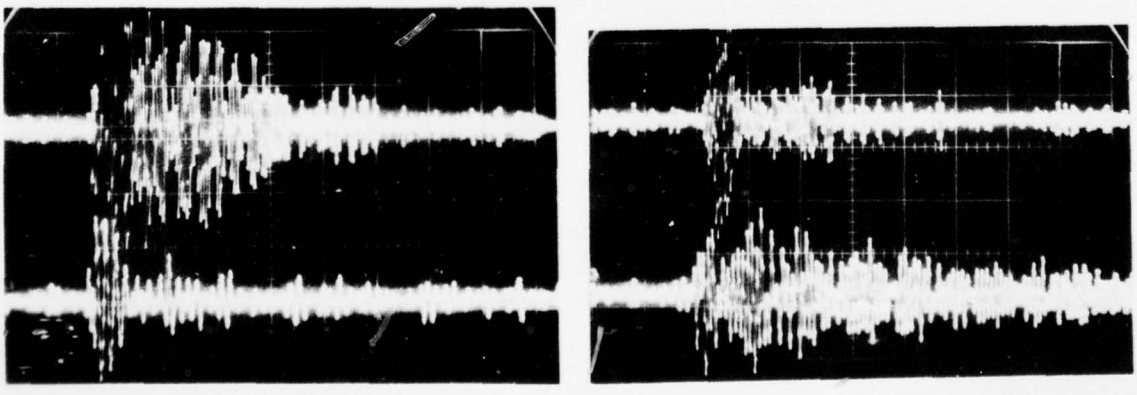

a. Signals from a well-bonded beam with a weak anchor at a force of about 20 mN.

b. Signals from a very weakly-bonded beam at a force of about 40 mN.

Figure 55. Acoustic emission signals from individual beams subjected to downward force on the horizontal portion of the beam. (Upper trace: probe detector; lower trace: substrate detector; horizontal scale: 20 μs/div.)

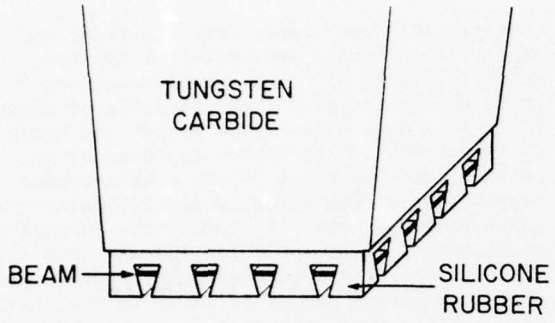

Figure 56. Beam-lead bonding tool modified to apply force to the beams without contacting the chip.

inner walls of the shortened sides of the tool are about 25 μm larger than the silicon chip on all sides. The rim of the probe was coated with silicone rubber and molded with a deep undercut pattern of the beams as shown in figure 56. In use, the probe is pressed down on top of the beams; the lower portion of the silicone rubber is forced against the substrate and bulges underneath the beam in such a manner as to lift the downward curving portion of the beam. A weak beam will be lifted upward resulting in acoustic emission. If the bugging height is uniform and if the probe is properly aligned to the chip and is perpendicular to the substrate, about 1.5 N can be applied before the device collapses. Most of this force is dissipated by compressing the silicone rubber and only a small amount is actually applied as a lift force to the beams. This probe concept appears to offer the best method of stressing weakly-bonded beams. The larger signal appears in the substrate detector, partly because the bond is more closely related to the substrate and partly because the coupling from the beams through the silicone rubber to the probe is relatively poor. However considerably more development is required to increase the operating life of the probe, and to obtain reproducible stressing forces and better coupling to the probe detector. This type of probe is only effective on devices with relatively uniform bugging height and bonds which extend at least 75 to 100 μm from the chip. Unlike the other probes employed in these tests, this probe cleanly strips off the free silicon nitride skirt in all areas away from the beam and anchor. The silicon nitride on top of the beams is not disturbed; the effect of the damage which does occur on device performance and reliability has not been determined [99].

Use of Acoustic Emission in Other Areas — Experiments were conducted to determine the feasibility of applying this technique to the evaluation of bond integrity on film carrier and reel systems. Tests on three different types of such systems indicated that the acoustic emission technique can be effectively used for this purpose [99]. In one case, a signal was obtained which could be correlated with the separation of a single solder bump. In a second case, several weak bonds in a gang-bonded device produced an emission burst. In a third case, a bond which was mechanically solid despite the fact that it had a poor visual appearance emitted no bursts.

Acoustic emission bursts were also observed when a weakly-bonded chip capacitor in a hybrid circuit was subjected to a downward force of about 2 N. Preliminary experiments suggest that acoustic emission can also be used to supplement the nondestructive wire bond pull test, both to assist in determining the maximum force to be applied and to assure the nondestructive nature of the test.

(G. G. Harman)

8.2. In-Process Bond Monitor

A series of experiments was carried out to determine whether there is any correlation between the vibration amplitude of an ultrasonic bonding tool during bonding and the bond quality as measured in terms of failure modes and the mean and standard deviation of the pull test.

The experimental set-up used was similar to that employed previously [101] except that since only the envelope of the nodal pattern was monitored there was no need for the two phase-delay pulse generators used in the previous work. The tool used in these experiments was a long 0.828-in. (21.0-mm) tungsten carbide tool with a 4-mil (100-μm) foot length. Also, the capacitor microphone was fitted with a stainless steel taper tip having a 25-mil (0.64-mm) diameter hole. This larger than usual taper tip was chosen for two reasons, both of which enhance its usability in an industrial environment. First, it is quite rugged and less easily damaged. Second, it gives an acceptable signal at low gain and hence is less susceptible to picking up any extraneous noise.

In all the experiments reported here, the node of the unloaded tool was found as follows: the tool was brought into contact with the wire to be bonded and the power dial set-

Table 17 — Pull Test Results for Monitored Ultrasonic Wire Bonds

Power Setting	Failure Mode	Mean Pull Strength, gf(mN)	Sample Standard Deviation, gf(mN)
2.0	lift-off	3.06 (30.0)	2.54 (24.9)
5.0	heel breakage	9.23 (90.5)	0.97 (9.5)
7.0	heel breakage	8.81 (86.3)	0.75 (7.4)
10.0	heel breakage	6.3 (62.0)	1.0 (9.8)
Control	mostly heel breakage	9.98 (97.8)	0.58 (5.7)

ting was turned down to its lowest position (1.0); the power was then turned on and the microphone was raised and lowered along the length of the tool until a minimum signal was obtained. This point was checked occasionally and was found to be fairly stable.

The first series of experiments employed aluminum pads of good bondability. On a single substrate, two different groups of aluminum bond pairs were fabricated. The first group, the control group, was made using the following machine settings for both the first and second bonds: power setting, 5.0; bonding time, 50 ms; and bonding force, 0.25 N. The control group bonds were pulled to destruction in order to establish that the power-time-force combination used in its fabrication produced acceptable bonds. The predominant failure mode found in the pull test was heel breakage. The overall mean, $\bar{x}$, and sample standard deviation, s, were 9.98 and 0.58 gf (97.8 and 5.7 mN), respectively; these values are indicative of a satisfactory bonding process which is under control.

The second group, the test group, was made with the same settings except that the power setting and bonding time for the second bond were set to zero. The second bond of each bond pair in this group was then made while the envelope of the nodal pattern was monitored. The force and time employed were the same as were used in bonding the control group; groups of eight bonds each were made with power settings of 2.0, 5.0, 7.0, and 10.0.

The results of the pull test are given in table 17. The pull strengths of the bonds made with a power setting of 2.0 are indicative of a bonding process which is out of control.

Typical microphone outputs (signatures) are shown in figure 57. The interesting feature of the signature of bonds made with the lowest power setting is the ringing characteristic at the beginning of the bonding cycle and the gradual tapering off of the tool vibration amplitude. The bonds made with higher power settings showed no evidence of ringing; all these bonds failed at the heel. This suggested that the microphone signal may be more sensitive to weld formation rather than to heel weakening due to excess deformation. It appeared likely that the nodal pattern contains only information concerning the quality of the weld. As the power increases, the interfacial weld strength also increases. However, at the same time the bond heel is further deformed which decreases its strength under the application of the pull test (NBS Spec. Publ. 400-19, p. 51).

Other experiments made with the same tool-transducer-power supply combination yielded similar results. When the experiments were repeated with a tool with a 2-mil (50-μm) footlength similar results were also obtained. When the experiments were repeated with different power supply-transducer combinations, however, no ringing was observed, even for the cases where the bonds failed by lift off.

Since the node rises during the loading of the tool during bonding, the vibrational amplitude at various positions below the node of the unloaded tool was studied at various power settings with the original transducer-power supply combination. If there were any ringing in the unloaded tool below the node it was expected to travel up to the position of the node during bonding where it could be detected by the microphone; in this case the ringing phenomenon would be suspected of being an artifact of the particular equipment being used. If ringing were not there, then there would be some reason to believe that ringing is a true signature of the lift-off failure mode. Ringing was observed 12 and 52 mils (0.30 and 1.32 mm) below the mode for a

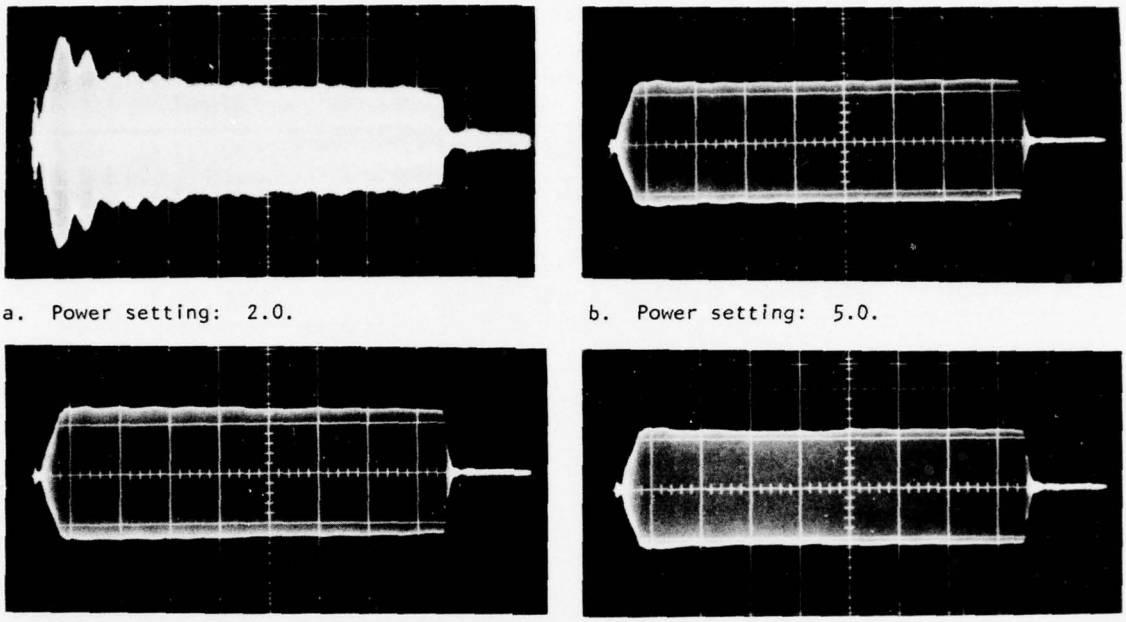

a. Power setting: 2.0.

b. Power setting: 5.0.

c. Power setting: 7.0.

d. Power setting: 10.0.

Figure 57. Typical signatures of ultrasonic aluminum-aluminum wire bonds made with different power settings.

power setting of 2.0 but not for power settings of 5.0 and 10.0.

These investigations indicate that the patterns which seemed to be typical of lift-off failure mode bonds were really artifacts of the particular coupling in the power supply-transducer-tool system when power is first applied to the tool. Consequently, it is doubtful whether ringing is a true signature of the lift-off failure mode, and so further development of this technique has been abandoned. (J. H. Albers)

8.3. Radioisotope Leak Test

The first exploratory round-robin evaluation of the radioisotope method for testing hermeticity of semiconductor devices (NBS Spec. Publ. 400-8, p. 40) [102] has been completed and the results analyzed. In undertaking the test it was resolved that the first priority was to determine the precision (interlaboratory agreement) inherent in the radioisotope method when applied to production devices and that a data base was required upon which a suitable draft standard could be developed. The resultant experiment was principally an accomplishment of the industry itself; NBS supplied measurement guidelines, calibration services, and participation in the direction and refereeing of the tests.

Ten industrial organizations participated in the experiment which was conducted according to strict metrological guidelines. To this end one specific type of equipment was used, one specific test sequence followed, all equipment serviced and calibrated prior to test, specimens neutralized between tests, and all testing refereed. A detailed trial test sequence was formulated and evaluated experimentally with 100 production integrated circuit packages; the final test sequence was modified in accordance with the results of this trial. Since a reference transfer vacuum gauge was essential for the determination of specific activity of the test gas at each site, a gauge was procured by and calibrated at NBS.

Test packages were culled from large lots of the selected type (14-lead ceramic dual in-line) to provide a selection of leaks which ranged from 10^{-8} to $\sim 10^{-4}$ atm·cm^3/s (10^{-9} to $\sim 10^{-5}$ Pa·m^3/s) as indicated by this method. One hundred test packages were circulated to each of the participating test sites; all packages survived the entire experiment. All

tests were refereed. Following resolution of several discrepancies, the ten measurements on each test package yielded leak rates which agree to within a fraction of the decade in which the mean value occurred [102]. This contrasts with prior results where the best agreement was one or more orders of magnitude.

This experiment has demonstrated conclusively that an interlaboratory comparison of hermetic packages can be accomplished under appropriate metrological guidelines. The inherent precision of production line radioisotope hermetic test equipment was determined on a stock integrated circuit item, and simultaneously it was shown that package leakage can remain stable. There is now an understanding of the variations that can occur from installation to installation and of some of the corrections that are necessary to provide a more uniform measurement capability.

(S. Ruthberg)

8.4. Loose Particle Detection*

Particle detection methods in current use fall into three major areas: x-ray (visual) detection, monitored random vibration (MRV) testing, and particle impact noise detection (PIND). Generally speaking, x-ray methods are limited in their ability to resolve very small particles and are time consuming. Vibration testing methods rely on the loose particle causing a detectable electrical malfunction of the energized microcircuit tested. Particle impact noise detection methods rely on the particle being shaken loose by vibration, hitting the circuit enclosure, and generating a signal which can be detected by an attached, sensitive transducer.

It is the last method which is currently used by a number of manufacturers of microcircuits to detect loose particles, primarily in circuits for military end use in high reliability devices. Despite the fact that these organizations have apparently used 100-percent screening, a number of loose-particle-induced circuit failures have occurred, suggesting that the screening methods used are not completely reliable.

A part of the problem appears due to the lack of uniformity among the particular test procedures used by the manufacturers. This was brought out at a recent meeting [103] at which it was concluded that no two contractors use the same set of conditions for the test parameters such as frequency, acceleration, axis of application, duration, oscilloscope sensitivity, and conditioning shocks. Consequently there is disagreement as to the effectiveness of this test method. The desire was expressed for a uniform test method, including calibration standards and optimized parameters. Particular areas in need of standardization cited include: the transducer, seeded packages for calibration purposes, attachment media (tape, couplant), preconditioning, on-the-shaker shock, parameters such as the vibration frequency and amplitude, the package size, and electrical bias effects.

Currently a draft procedure is being considered for inclusion in MIL-STD-883, Test Methods for Microcircuits. This procedure, in brief, requires a small vibrational shaker with low inherent noise, a noise detection system, an attachment medium, and a shock tool to help detach loose particles which may have become temporarily attached to the inside of the microcircuit enclosure. In the use of the procedure, the microcircuit under test is attached to an ultrasonic transducer which is mounted on the shaker. During vibration, particles present in the microcircuit are shaken loose and impact the walls of the circuit enclosure producing an acoustic impact signal. This signal is picked up by the ultrasonic transducer, amplified by a transducer amplifier, and made audible by a speaker. The output can also be displayed on an oscilloscope. If the particle cannot readily be shaken loose to produce the impact signal, a shock tool is applied to the circuit enclosure to facilitate this without, however, damaging the circuit itself.

The proposed particle impact noise test specifies vibration frequencies and amplitudes, suggests a type of vibration shaker and several attachment media, recommends a particular commercial acoustic noise detection system, and a commercial shock tool. It also specifies the test procedure to be used. Discussions with a variety of manufacturers of semiconductor circuits using variations of this test suggested that: test equipment specifications and details of procedure are not sufficiently explicit in some areas to lead to repeatable and replicable results and, where they are explicit, there is little assurance that they describe optimum conditions.

---

*Principally funded by SAMSO with additional funding from the NBS Nondestructive Evaluation Program.

Accordingly, a task was undertaken to investigate the PIND test by examining the equipment and procedure in detail to obtain experimental data leading to an optimized test. An additional objective is to develop standard seeded microcircuits which can serve as reference standards for in-house checking of PIND test equipment and procedures by way of round-robin experiments.

Since seven of the nine major manufacturers as well as some users of these microcircuits use a particular brand of commercial PIND system and a particular shock tool, these were procured for investigation. In addition, a selection of seeded circuits was obtained from one of the manufacturers. Preliminary experimental work was conducted, using the seeded cans, to gain experience with the equipment. Following this, a more structured investigation was started.

An experiment was conducted to determine the effectiveness of the various attachment media specified in the PIND test procedure to transmit vibrational accelerations to a simulated microcircuit, as represented by a subminiature piezoelectric accelerometer mounted on a small flat aluminum base. The total weight of both components was 0.4 g. The test accelerometer was first directly mounted on the table of an electromagnetic vibration exciter and a frequency response was run against the built-in reference accelerometer. The test accelerometer was then attached to the table by means of one of the attachment media and the response was again measured over a frequency range from 30 to 5000 Hz, at acceleration amplitudes of 10 and 20 g_n. The data show response ratios between direct mounted and couplant-attached accelerometer outputs with a maximum spread from 0.94 to 1.03 for the three couplants tested. Over the frequency range from 30 to 1000 Hz, considered most likely to be the PIND operating range, response ratios ranged from 0.97 to 1.03. This suggests that none of the three couplants tested is likely to significantly reduce the acceleration applied to the microcircuits attached to the PIND equipment.

Table 18 – Representative Response Frequencies of Metal Spheres Impacting a Steel Surface

Material	Weight, μg	Frequency, kHz
Gold	10	621
Steel	10	825
Aluminum	1.4	1270

It was felt desirable to attempt to determine the theoretical frequencies generated when loose particles impact the walls of the microcircuit enclosure. This was considered as the case of the impact of a solid sphere on an elastic plate which is a classical problem [104]. If the velocity of impact is small and the diameter of the sphere is small compared with the thickness of the plate, the response frequency is proportional to the ratio of the impact velocity to Poisson's ratio. Assuming vibrational accelerations with an amplitude of 10 g_n (zero to peak) at 60 Hz, values were calculated for representative metal spheres impacting a steel surface; the results are given in table 18. These frequencies are considerably higher than the frequency of maximum response of the PIND system, which is in the range from 130 to 170 kHz. Nevertheless, the former should be able to shock excite the latter, thus producing a measurable output. (P. S. Lederer[+], J. S. Hilten[+], and C. F. Vezzetti[+])

[+]NBS Components and Applications Section, Electronic Technology Division.

9. DEVICE INSPECTION AND TEST

9.1. Dual-Laser, Flying-Spot Scanner

Temperature Measurement — A method has been developed to obtain a quantitative measure of the localized temperatures within operating bipolar silicon devices. The method employs the temperature enhancement of the 1.15-μm photoresponse discussed previously (NBS Spec. Publ. 400-25, p. 58). One of the advantages of the method is that the spatial temperature resolution may be as fine as the size of the spot used for scanning, which is five to ten times finer than the resolution which can normally be achieved with other methods for measuring localized temperatures.

In developing the method, a generalized bipolar transistor element first was analyzed with the temperature-indicating photogeneration allowed to occur simultaneously within the emitter, base, and collector regions while at the same time the device was biased for its normal service as an amplifier of electrical signals. For the usual common-emitter configuration, the collector current, j_c, for the transistor element was found to be

$$j_c = j_b\beta_F + j_{h\upsilon EMIT}\beta_F + j_{h\upsilon BASE}(\beta_F+\tfrac{1}{2}) + j_{h\upsilon COLL}(\beta_F+1) , \qquad (22)$$

where β_F is the forward current gain, j_b is the base current supplied from an external electrical source, and $j_{h\upsilon EMIT}$, $j_{h\upsilon BASE}$, and $j_{h\upsilon COLL}$ are the photocurrents generated in the emitter, base, and collector regions respectively. For most devices of interest, and in particular for the 2N4431 UHF transistors used to test the method, the first two photocurrents may be neglected with respect to the third:

$$j_c \simeq j_b\beta_F + j_{h\upsilon COLL}(\beta_F+1) . \qquad (23)$$

A plot of $j_{h\upsilon COLL}$ as a function of temperature is readily obtained by measuring the base-collector photodiode response with the transistor in thermal contact with a heat source of known and adjustable temperature. The base-collector photoresponses to 1.15- and 0.633-μm radiation, normalized to their values at 30°C are shown for a representative device in figure 58. The temperature enhancement of the 1.15-μm photoresponse is a bulk effect; analysis shows that the photoresponse can be fitted by theory when the effects of both the increase in phonon population and decrease in bandgap are included.

By scanning a device with the 1.15-μm laser, a map of the photoresponse is obtained. If the current gain is spatially uniform, this photoresponse may be interpreted directly with the aid of a calibration curve such as the upper one in figure 58 to yield a map of local temperature. If the gain is not spatially uniform, which occurs when a device is operating in the hot-spot regime, it is necessary to correct the 1.15-μm photoresponse for gain variations. This can be done by scanning the device with the 0.633-μm laser, since the 0.633-μm photoresponse is independent of temperature.

Several 2N4431 transistors operating in the hot-spot regime were used to test this electronic thermal mapping method. Temperature profiles through the center of the hot spot were made with both the laser scanner [105] and a commercial infrared microradiometer on two devices. The resulting temperature profiles are shown in figure 59. The spatial resolution for the microradiometer was 35 μm, compared to 4 μm for the laser scanner. Implicit in the calibration of the microradiometer is the assumption that the object filling the field of view has a uniform tempera-

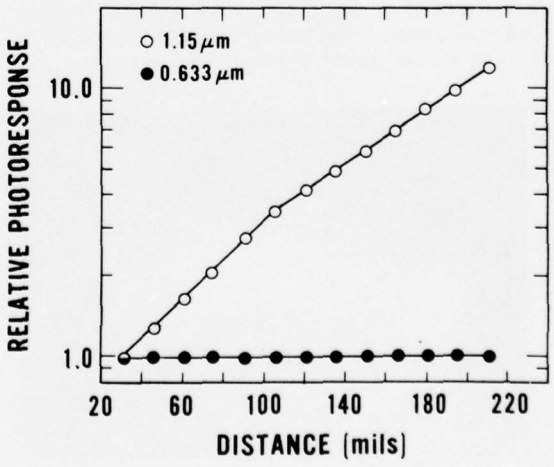

Figure 58. Photoresponse of a typical 2N4431 UHF transistor to 0.633- and 1.15-μm radiation as a function of temperature.

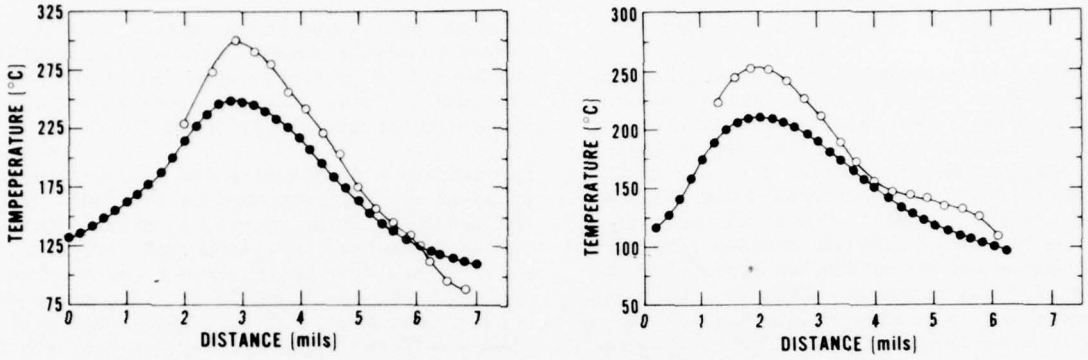

a. Device No. 7.

b. Device No. 9.

Figure 59. Temperature profile of hot spots in typical 2N4431 UHF transistors as measured with a laser scanner (o) and an infrared microradiometer (●).

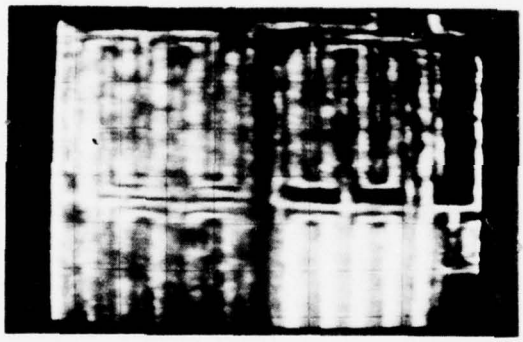

Figure 60. Photograph of the reflected light plus photoresponse image obtained when the 0.633-μm laser beam scans the back side of a silicon-on-sapphire C-MOS 4007 inverter.

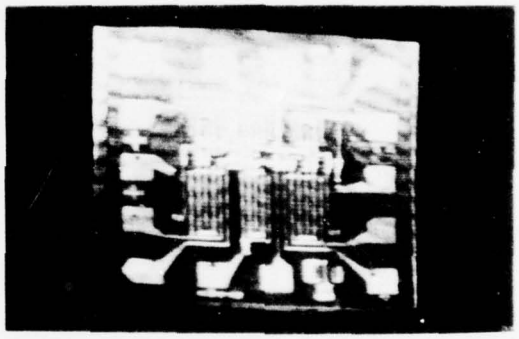

Figure 61. Photograph of the reflected light image obtained when the 1.15-μm laser beam scans the back side of a flip-chip C-MOS 4007 inverter.

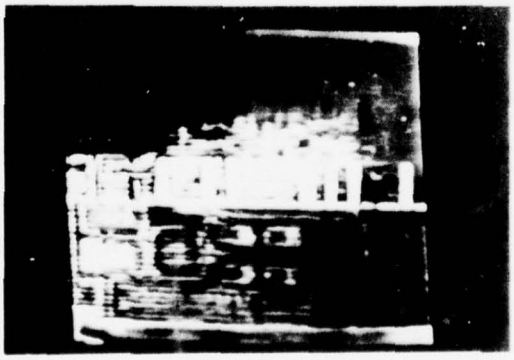

a. Input voltage: 0 V.

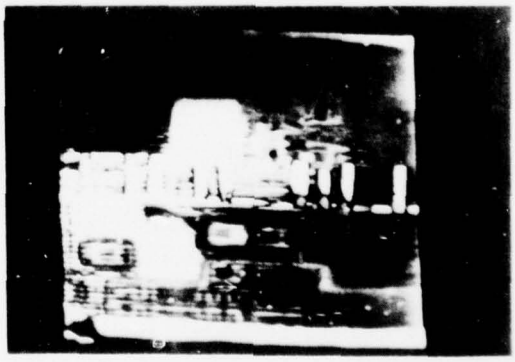

b. Input voltage: -1.5 V.

Figure 62. Photographs of the reflected light plus photoresponse image obtained when the 1.15-μm laser beam scans the back side of a flip-chip 709 operational amplifier.

ture. When the microradiometer is focused on the center of a hot spot in which the peak temperature occurs over a region much smaller than 35 μm across, it interprets the radiant energy it intercepts as coming from a uniform, but lower, temperature. The discrepancy should not be as great when the microradiometer is focused on a temperature slope since it is receiving energy both from hotter and colder portions simultaneously. The results shown are consistent with both of these premises. (D. E. Sawyer and H. P. D. Lanyon*)

Back side Inspection — The possibility of using the laser scanner to look through the back side of devices was briefly explored. Use of this technique permits inspection or failure analysis of flip-chip or beam-lead devices which are mounted circuit side down. Another significant advantage in scanning a device from the back side is that greater accessibility to the active regions is obtained because metal does not block the optical radiation. A disadvantage is that the surface of the back side is generally unpolished, and the roughness degrades the image obtained. This problem can be alleviated somewhat by placing a drop of oil or other substance on the device in an attempt to match indices of refraction at the rough surface. The interface between the air and this substance is a smooth one, and image distortions are generally not caused by it.

Three devices were examined from the back side with the laser scanner [105]. A silicon-on-sapphire C-MOS 4007 inverter was bonded into a special flat-pack-type holder that could be examined from either the circuit side or the back side. The sapphire is transparent to the 0.633-μm laser light which was used to scan the device. A drop of oil was put on the surface to improve the image. The reflected light image mixed with the photoresponse signal is shown in figure 60. Of the four transistors shown in the figure, only the lower right hand one was electrically connected. The five brightly lit stripes are the gate area.

A bulk-silicon, flip-chip C-MOS 4007 was also examined from the back side with the laser scanner. Unlike sapphire, silicon is not transparent to the visible light and the infrared (1.15-μm) laser had to be used. The bulk device was mounted in the same manner as the sapphire device. Figure 61 shows a reflected light image obtained by scanning through the back side which was polished, so that no oil was needed.

A flip-chip type 709 operational amplifier was also studied. This bulk silicon device had its part number scratched into the back surface which was unpolished. The infrared laser was used, and a drop of oil was put on the surface. The operational amplifier was connected for normal circuit operation in an amplifier stage with a gain of 10. The reflected light image superimposed on the photoresponse is shown in figure 62 for two operating conditions. In the display obtained with the input held at 0 V (fig. 62a) different transistors in the circuit yield larger photoresponse than in the display obtained with the input at -1.5 V (fig. 62b), which is sufficiently large to saturate the device.

(D. W. Berning and D. C. Lewis†)

Instrumental Improvements — A conventional color TV set was modified to serve as a three-gun color display for the laser scanner. With this display the various information channels can be displayed at the same time and still maintain their identity. For example, the reflected light signal can be presented in one color and photoresponse in another. If the device under investigation has two power supply connections, a third color can be used for the second supply photoresponse. Another application of the colors involves mixing the colors in proportions relating to specimen photoresponse voltage. The eye can discriminate between various hues very easily. With the monochromatic display, areas on the specimen producing equal photoresponse can only be accurately compared by careful measurement using the vertical deflection technique, but with the color display it is easy to see at a glance the areas producing equal photoresponse. Isothermal contours of transistors in hot-spot operation can also be identified easily.

(D. W. Berning)

9.2. Scanning Acoustic Microscopy

This task was undertaken with the aim of producing, if feasible, a scanning acoustic microscope suited to examination of solid-state devices. Rather than sensing the dielectric properties of surfaces as in optical microscopy, the acoustic microscope responds to the

---

*Worcester Polytechnic Institute, Worcester, Mass. 01609.

†Office of Naval Research, Washington, D.C. 22217.

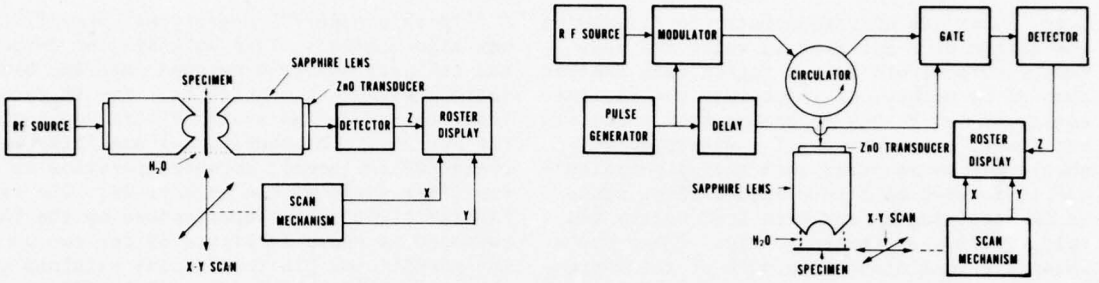

a. Transmission mode, cw only.

b. Reflection mode, cw or pulse.

Figure 63. Comparison of operating modes of the scanning acoustic microscope.

mechanical characteristics of surfaces and near subsurface regions. It is this basic difference in response which, it is hoped, will reveal useful information that is not evident in ordinary light microscopy.

The initial activity of the Stanford portion of this task has been focused on the problem of perfecting an instrument which is capable of operating in a pulsed mode with a frequency near 1000 MHz and with a resolution that is less than 1 μm. Consequently, a major part of the work has been concerned with instrument development.

The Stanford instrument which existed at the start of the contract effort was a transmission mode microscope developed mainly for examination of biological specimens [106]. This design has been modified for reflection mode operation [107]. Figure 63 shows a comparison between the two modes. The transmission mode microscope was designed for cw operation; cw operation is possible in the reflection mode if the pulse generator, modulator, gate and delay blocks are omitted.

If the specimen surface is not precisely parallel to the scan plane, changes in the length of the transmission path during a cw scan produce a distracting moiré pattern as shown in figure 64a. Pulsed operation avoids this difficulty as figure 64b illustrates, since the transmitted and reflected signals do not co-exist and thus cannot interfere. In the reflection mode, one must choose the lens length such that reflections other than those from the specimen (for example, from the outer annulus of the lens face) do not obscure the desired signal.

Pulsed operation has necessitated a redesign of the matching networks between the coaxial line and the zinc-oxide transducer to provide

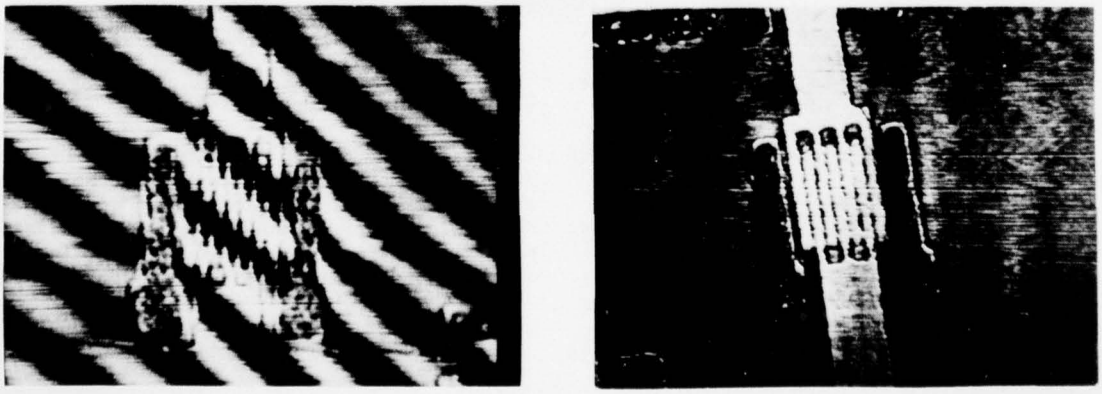

a. Reflection mode, cw operation.

b. Reflection mode, pulsed operation.

Figure 64. Acoustic images showing differences between cw and pulsed operation.

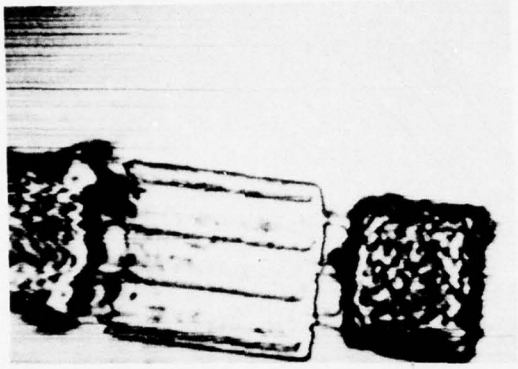

a. Acoustic image, reflection mode, pulsed operation; magnification: ∿1900x.

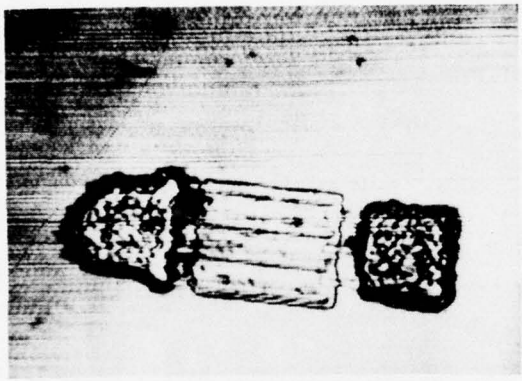

b. Acoustic image, reflection mode, pulsed operation; magnification: ∿1300x,

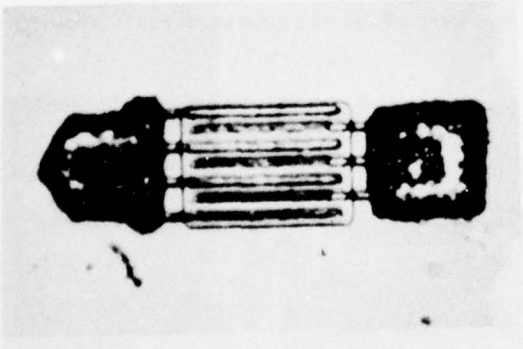

c. Optical image, interference contrast; magnification: ∿1400x.

Figure 65. Comparison between 940-MHz acoustic images of a bipolar microwave transistor with 2-μm wide metal fingers and a photomicrograph taken with interference contrast.

wider bandwidth in order to avoid pulse distortion. The current bandwidth of 200 MHz is adequate for the 75-ns pulse lengths now being used. In addition to removing the moiré pattern, use of these short pulses has apparently increased the image clarity and improved the resolving power. The reasons for this improvement are not understood; much more remains to be done in developing the theory of imaging using focused acoustic waves.

New microscope systems have been built in which the operating frequency has been increased from 350 MHz to 600 MHz and, most recently, to 940 MHz. The wavelength in water decreased from 4.3 μm to 2.5 μm and 1.6 μm, respectively, with correspondingly improved resolution. The resolution achievable with the 940-MHz instrument is illustrated in figure 65. The scale in those images can be realized from the width of the fingers which is 2 μm. These are clearly resolved in the two acoustic images of different magnification. These and related studies suggest that the limit of resolution is now less than 0.5 μm which is approaching one-third of a wavelength. An optical photo taken with a Nomarski type of interference microscope is included in the figure for comparison; this image represents something approaching the state-of-the-art in optical microscopy. This comparison shows that the details available from the optical image are accurately reproduced in the acoustic image. The raggedness at the edge of the rectangular pad in the acoustic images is a result of excessive noise on the mechanical scanning system. This can be eliminated with some improvement in the design of the scanning circuits in this system.

Attenuation in water decreases significantly with increasing temperature, as shown in the curves of figure 66. With this in mind it should, in principle, be possible to monitor point by point the temperature profile of an operating device. With a given circuit under power, those regions which are hot should appear brighter in the image since the liquid absorption in the heated region is diminished as compared to the unheated region. With scanning this temperature profile should show up as variations in the brightness of the image. Although a first demonstration of this principle was successful, the minimum detectable temperature change and the possible spatial resolution have not yet been established.

Initial work was undertaken to study the effectiveness of using reflection-type imaging

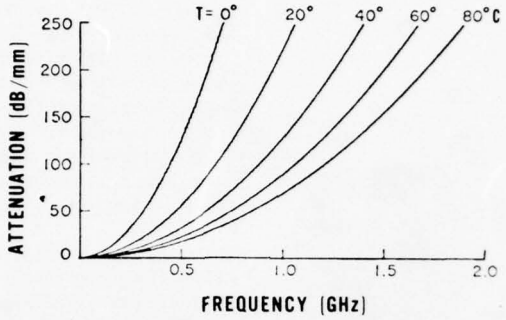

Figure 66. Frequency dependence of attenuation of acoustic waves in water at various temperatures.

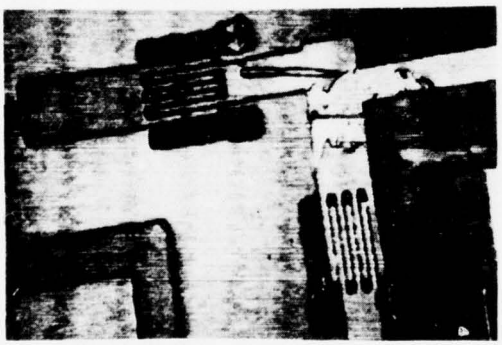

a. Normal incidence.

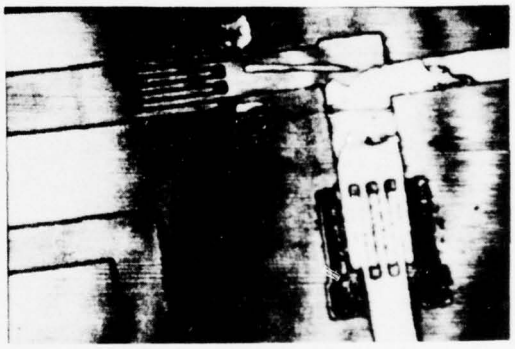

b. Angle of incidence: 20 deg from normal.

Figure 67. Acoustic images, reflection mode at 940 MHz, of an integrated circuit showing the effect of non-normal incidence.

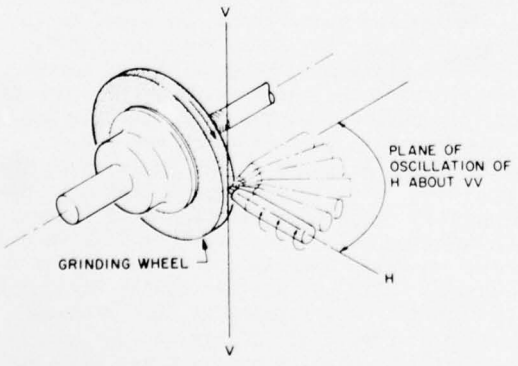

Figure 68. Spherical tool grinder for making acoustic lenses.

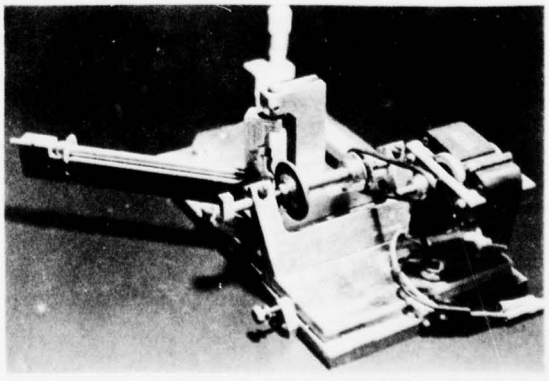

Figure 69. Photograph of the tool grinder.

where the acoustic beam is not at normal incidence to the plane of the specimen. It is a relatively easy matter to tilt the substrate and record the image in this off-axis arrangement. A comparison of images obtained with normal and non-normal incidence is shown in figure 67. It can be seen that the quality of the off-axis image is at least as good as the image at normal incidence, and some of the finer detail stands out with more crispness. This technique appears to be worthy of detailed study. (C. F. Quate[§])

Since the acoustic losses in water, the transmission medium between lens and specimen, increase as the square of the frequency to about 100 dB/mm at 1 GHz, the path length is severely limited at the higher frequencies. For this reason, it has been necessary to devise means for making concave lens surfaces of very small radius. As the lens diameter is reduced the acoustic path length in the liquid cell between the two confocal lens surfaces is reduced. This reduction permits use of the microscope at higher operating frequency with a fixed attenuation.

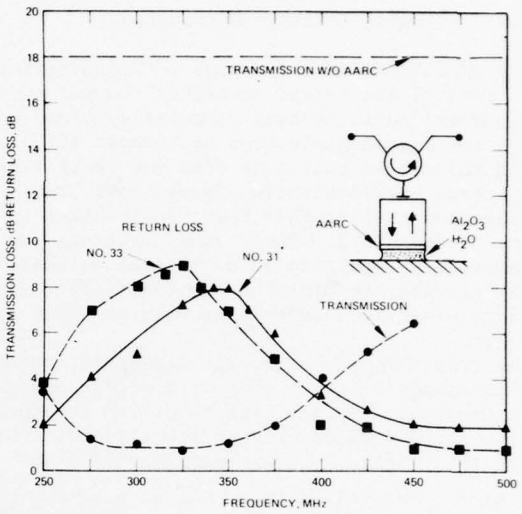

Figure 70. Frequency response of return and transmission loss of two sputtered glass acoustic anti-reflection coatings (AARC). (The experimental arrangement is shown inset.)

A new machine has been designed and built for the purpose of grinding spherical tips on tiny rods. These spherical tips are the tool which is used to grind and polish the lenses. The efficiency of the machine is so good that several tips can be fabricated in an hour. This means that it is feasible to use a separate tip for each lens. A schematic of the principle of operation of the machine is shown in figure 68. A spherical surface is produced by rotation about axis H and oscillation about axis VV if H and VV intersect. A photograph of the completed instrument with a tip mounted in the rotating holder is shown in figure 69. With these improvements, lenses with a radius of 50 μm have been successfully ground and polished. This is a significant decrease since the lenses used to record the images as reported here had a radius of 100 μm. The factor of two in radius should permit the operating frequency to be increased by 40 percent. (W. A. Bond[§])

The inital objective of the Hughes portion of the task was to construct a second-generation laboratory microscope with the most useful features for examining solid-state devices, building on the knowledge and experience available from Stanford. Such an instrument has been constructed. This microscope was designed to operate at 400 MHz in the cw reflection mode. Since being placed in operation around mid-April, the microscope has demonstrated good day-to-day mechanical and electronic stability. The resolution appears to be better than 2.5 μm. Pulsed operation has been achieved in a separate bench-top apparatus to establish the correct behavior of the additional electronic circuitry but has not yet been incorporated in the microscope. Preliminary experiments show that the useful depth of field at 400 MHz is about 20 μm, a figure which does not appear to impose serious limitations on the utility of the instrument.

An anti-reflection coating has been developed to reduce signal losses at the lens-water interface [108]. The performance improvement gained by use of the anti-reflection coating is shown in figure 70. Of the maximum possible 18 dB-signal loss reduction, 17-dB loss reduction is achieved. The geometry of the experiment is shown in the inset of the figure. (R. G. Wilson[¶] and R. D. Weglein[¶])

[§]Work conducted at Microwave Laboratory, Stanford University, under NBS Contract No. 5-35899. NBS contact for additional information: R. I. Scace.

[¶]Work conducted at Hughes Research Laboratories under NBS Contract No. 5-35898. NBS contact for additional information: R. I. Scace.

9.3. Scanning Electron Microscopy

Electron-Beam-Induced Damage — Illustrations of typical electrical parameter changes encountered in integrated circuits examined using the scanning electron microscope (SEM) and the use of radiation dose for describing electron beam ionization damage have been presented earlier (NBS Spec. Publ. 400-17, pp. 43-46) [109]. These considerations are especially important in developing an analysis strategy to minimize the destructive aspects of device examination with an SEM.

The relevance of the energy deposited, rather than simply exposure time or electron energy, in understanding the effects of SEM exposure can be illustrated through the threshold voltage shifts (ΔV_{Th}) of a *p*-channel MOS transistor. For this device, the gate oxide (the critical oxide) was 100 nm of silicon dioxide beneath approximately 1 μm of aluminum (the gate) which in turn was beneath a silicon dioxide overcoat approximately 1 μm thick. SEM exposures were made of four specimens, two at 17.5 keV and two at 30 keV, at an electron flux of 5.2×10^{10} $cm^{-2} \cdot s^{-1}$. The device leads were floating during exposure. The shift in threshold voltage for the two beam energies is shown in figure 71. When the shifts are plotted as a function of exposure time, two curves result (fig. 71a). These data can also be replotted as a function of the radiation dose delivered to the critical oxide; plotted in this manner, the shifts approximately fall along the same curve (fig. 71b) demonstrating that the relevant parameter for understanding oxide effects is the dose.

Even though the calculations of dose are not always convenient or even necessary, the expression for dose,

$$\text{Dose} = \frac{100\ I_B t}{A_s} \cdot E_B \cdot \frac{f_D}{T_{ox}} \quad , \tag{24}$$

yields certain insights which are useful in understanding how to minimize beam damage.

The first factor relates strictly to parameters of the SEM exposure: the beam current, I_B; time, t; and magnification, which is related to the scanned area, A_s. Obviously the energy deposited can be reduced by reducing I_B and *t*. Reducing the area scanned (increasing magnification) locally increases the dose. The second factor, the energy of the electrons in the beam, is the quantity which links the strictly SEM parameters to the device geometrical parameters of the third factor; E_B determines the depth to which the electrons penetrate. In the last factor, f_D is the fraction of the incident electron energy deposited in the critical oxide region of thickness, T_{ox}. This fraction depends on both the device structure and the beam energy. In particular, f_D is zero if the energy in the beam is absorbed in inactive layers, such as the passivation overcoat and metallization, above the critical oxide. For the example

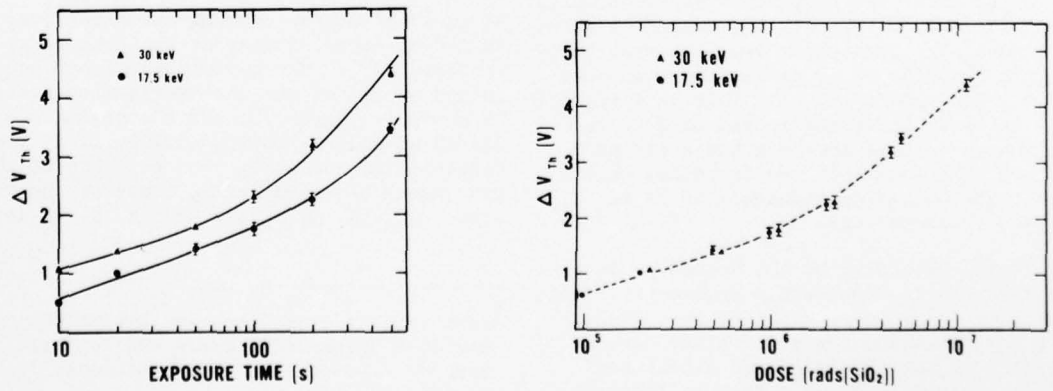

a. Plotted as a function of exposure time.

b. Plotted as a function of absorbed dose.

Figure 71. Change in threshold voltage, ΔV_{Th}, of a p-channel MOS transistor as the result of exposure to an electron flux of 5.2×1010 $cm^{-2} \cdot s^{-1}$ at energies of 17.5 and 30 keV in a scanning electron microscope.

discussed above, no energy is deposited in the critical oxide for beam energies of 15 keV and below. If energy is not deposited in oxide regions critical to the device operation, the electrical parameters of the device will not be altered.

Any possible electrical parameter degradation resulting from the electron beam must be carefully considered when developing a quality assurance program, performing construction analysis, or planning a failure analysis procedure involving device inspection in the SEM. If a device is expected to function electrically after SEM examination, it is essential to develop a careful analysis strategy based on the parameters in eq (24) before the device is placed in the SEM specimen chamber.

(K. F. Galloway, W. J. Keery, and K. O. Leedy)

Electron-Beam-Induced-Current Mode — A simple method of calculation for estimating the magnitude of the electron-beam-induced current (EBIC) in simple device structures has been described previously (NBS Spec. Publ. 400-19, pp. 56-59) [110]. Some of the limitations of this method were illustrated by comparing the EBIC signals from a diode intentionally doped with a metallic impurity and from a simple *npn* transistor with the currents calculated using the simple method.

Consider first a typical EBIC application in the imaging of a subsurface defect. An EBIC image of a diode intentionally doped with copper is shown in figure 72a. There is apparent copper clustering at defect sites in the silicon as expected from the work of Schwuttke [111]. The EBIC signal as a 250 pA, 10 keV electron beam traverses one of these clusters at high magnification is shown in figure 72b. Away from the cluster, the gain is 720 whereas the calculation based on the simple method would predict approximately 2500. In the cluster region, the gain is reduced further by a factor of 3. The gain results given in this example indicate one of the deficiencies of the calculation. With the lifetime reduction caused by the copper impurities, the assumption of 100-percent collection efficiency is no longer valid.

As might be expected, electron-beam-induced currents and the resulting images in transistors and integrated circuits are often complex. The existence of additional leakage paths and interacting junctions are sources of additional complications. An example of the errors which can be introduced by these factors is illustrated in figure 73 for an

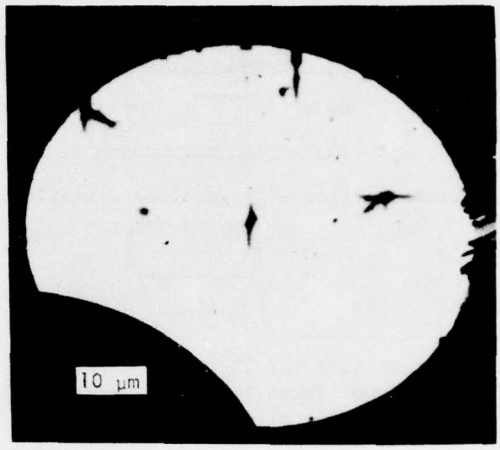

a. EBIC image of diode showing copper clusters.

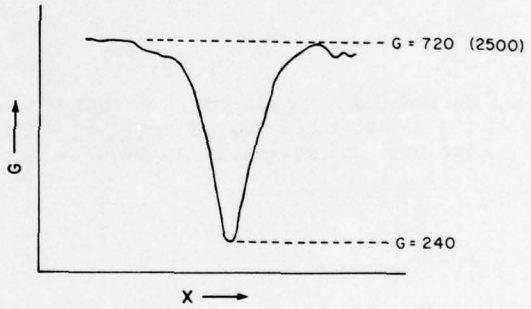

b. EBIC signal as 10-keV electron beam traverses a cluster. Measured gains, G, are indicated; the number in parenthesis is the gain calculated from the simple model.

Figure 72. Electron-beam-induced-current response of a copper-doped silicon *p-n* diode.

npn transistor with oxide and aluminum thicknesses and junction depths as indicated in the figure. EBIC scans across the device, made under various conditions, are also shown. In each scan, the signal was taken from one region of the transistor and the other regions were grounded. The gain scales are not linear; selected values are indicated and compared with values in parentheses calculated using the simple method. The signal is a maximum where the active junction vertically approaches the surface. This geometrical arrangement allows for maximum collection efficiency, and the best agreement with the calculation occurs at these points. The measured signal from the emitter at 10 keV is in

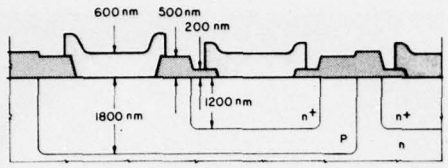

a. Cross section with vertical dimensions.

b. Current gain for 10-keV electrons with the signal taken from the emitter with the base and collector grounded.

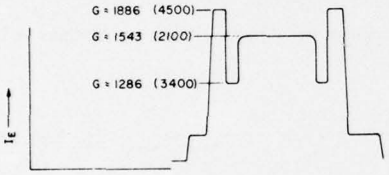

c. Current gain for 20-keV electrons with the signal taken from the emitter with the base and collector grounded.

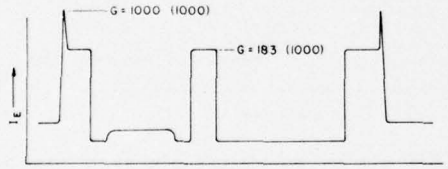

d. Current gain for 10-keV electrons with the signal taken from the collector with the base and emitter grounded.

Figure 73. Electron-beam-induced-current response of a silicon *npn* transistor. (Measured gains, G, are indicated; numbers in parentheses are gains calculated from the simple model.)

better agreement with the calculation than that at 20 keV because of differences in electron penetration. At 10 keV, most of the energy is deposited at depths less than 1000 nm while at 20 keV a significant fraction is deposited at greater depths. At 10 keV, the signal drops off rapidly away from the point where the active junction intersects the surface; at this energy, the beam does not penetrate to the horizontal part of the junction.

(K. F. Galloway, W. J. Keery, and K. O. Leedy)

Accurate models are not available to account for these various complicating factors. Nevertheless, the EBIC mode has been very successfully applied in a comparative mode [112]. In circuits of a repetitive nature such as multiple-gate devices, multiple-bit shift registers, flip-flops, or any circuit where a circuit function is duplicated, operating and nonoperating regions can be compared. Where a duplication of function within a single die is not available, the EBIC display from a good circuit can be compared with that from a defective circuit. In all applications of a comparative nature, the instrument conditions must be held constant from specimen to specimen.

One particularly useful application of this mode of examination is in locating in failed devices the malfunctioning region which can then be the focus of investigation by other means. Two examples of this application are given. The first is a quad 2-input NAND gate which contained four identical gates. An optical photomicrograph of the upper portion of the die showing two of the four gates is reproduced as figure 74a. The gate on the right was not functional in either an ac or dc mode. However, visual inspection failed to detect any pertinent anomalies. Examination of an EBIC image obtained from the ground pin of the device (fig. 74b) reveals that there is a resistor (arrow) visible in the inoperative circuit which is not apparent in the good one. A careful analysis of the circuit indicated that this must be due to an unwanted leakage path from that resistor or its metallization to ground. Subsequently, the metallization was removed and a pin hole was found beneath the metallization stripe outside the resistor tub. This effectively shorted the resistor to ground enabling the electron-beam-induced current in the resistor to be collected and displayed.

The second example is a group of eleven failed low-power four-bit shift registers. EBIC images of the bad circuits were checked against those of a functional one. As in the first example, the EBIC signal was collected from the device ground. Figure 75a shows an EBIC image of a good device; the arrow indicates the presence of a junction which was not visible in the EBIC images of the bad devices, one of which is shown in figure 75b.

In a more thorough inspection of the suspect area, it was found to consist of an input protection diode junction. With greatly increased beam currents an EBIC response of this junction was detectable as is shown in

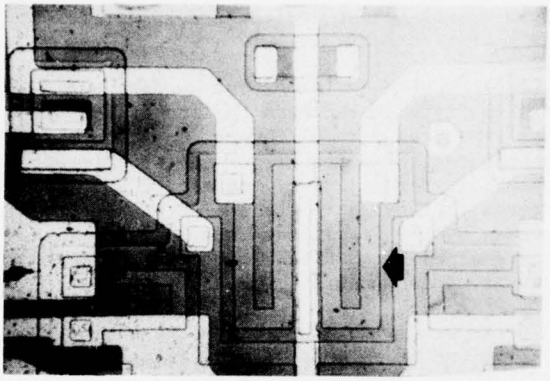

a. Optical photomicrograph; no difference between the gates is visible.

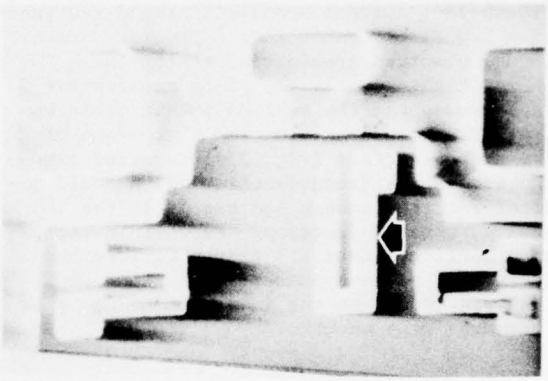

b. EBIC image; the response from the resistor (arrow) identifies the faulty element.

Figure 74. Portion of a quad 2-input NAND gate including a functional gate on the left and a nonfunctional gate on the right.

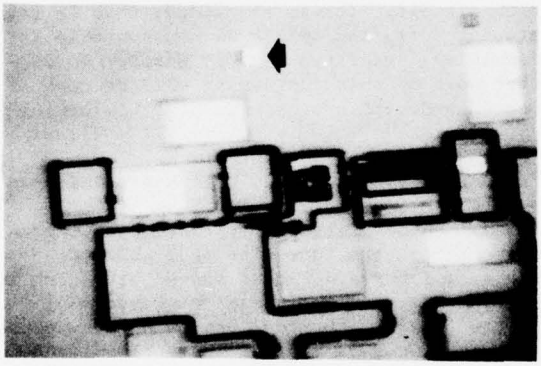

a. EBIC image of a good device; note junction marked by arrow which does not appear in the images of faulty devices.

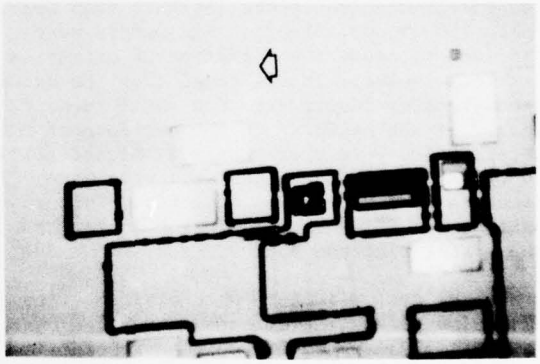

b. EBIC image of a failed device; note absence of junction visible in good devices.

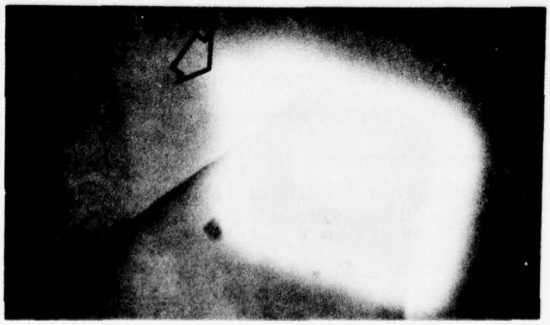

c. Junction made visible in EBIC image by use of larger beam current; note current anomalies (arrow).

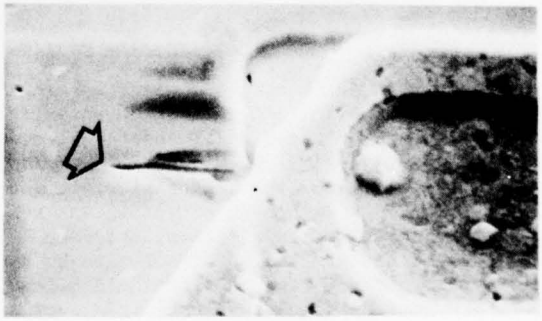

d. Scanning electron micrograph of the junction after preferential etching, showing damage (arrow).

Figure 75. Portions of a low-power, four-bit shift register.

figure 75c; current anomalies around the junction are also visible in the figure. A secondary electron examination of this area showed nothing until the glass passivation was removed and the surface etched preferentially. A scanning electron micrograph of the etched surface (fig. 75d) revealed damage across the diode junction which could account for the leakage and result in the low gain across the junction. Further investigation confirmed that all eleven devices had failed in the same manner at the same pin. This was traced to the improper set up of an automatic test machine.

(J. R. Devaney[#] and K. O. Leedy)

9.4. Automated Scanning Low Energy Electron Probe

Additional investigations of wafer defects were carried out with the automated scanning low energy electron probe (ASLEEP) (NBS Spec. Publ. 400-29, pp. 58-59). Six wafers were oxidized to cause the formation of oxidation stacking faults. It was found that the oxidation stacking faults were too small to be resolved by the ASLEEP. On the portions of the wafers which were preferentially etched [113] to reveal the defects, the etch pits were found to be 1 to 2 μm in diameter. This appears to be below the resolution limit for the ASLEEP electron optics.

A special test structure with minimum exposed oxide (to reduce the effects of surface charging) was constructed for voltage resolution measurements. A gold metallized alumina substrate was divided into two large pads separated by an 80-μm gap. An adjustable voltage was applied between the two pads and its effect on the video signal was studied. A single line was scanned across the pads and the target current was displayed on the oscilloscope. The potential on each pad was adjusted so that the currents on each were equal and less than 1 nA. Then the potential of one pad was adjusted until the target current was displaced by the width of the noise on the scope. Under the best achievable conditions, a 25-mV change in potential was required to do this. In addition, the computer was used to measure voltage resolution by applying the cathode ramp and threshold detector. Comparison of measurements made over a period of less than a minute showed standard deviations of 1 mV but long term drifts degraded the accuracy of the measurement and increased the standard deviation to 10 mV. These drifts are due to the wandering of the beam on the target surface and to variations in heater current.

Efforts were made to observe surface potential differences between regions of a specimen implanted with different densities of phosphorus. The results of the experiments showed that charging of the native oxide obscures the change in surface potential caused by the Fermi level shift due to doping and prevents ASLEEP from making doping density measurements.

Efforts were also made to observe potential variations of an unpassivated integrated circuit chip. The ASLEEP was barely able to resolve portions of the circuit consisting of 5-μm lines with 7-μm spaces. Observations were impaired because of surface charging effects; attempts to steer the beam so that it probed only the metal interconnects were unsuccessful because of drifts in the deflection circuit. It was concluded, that in its present form, the ASLEEP is not suitable for examining integrated circuit chips. No further work on this instrument will be conducted under this program. (W. C. Jenkins[×])

9.5. Thermal Properties of Transistors[+]

A model to describe the initiation of thermal instability, the formation of stable hot spots, and forward biased second breakdown in power transistors has been developed and tested [114]. The model has been used to predict the locus of thermal instability (hot-spot formation) in the $I_C - V_{CE}$ [(collector-current)-(collector-emitter voltage)] plane to within about 5 percent. For the stable hot-spot mode, the model describes the qualitative behavior of the peak junction temperature, the current density distribution, and the area of the stable hot spot. The model also qualitatively describes the $I_C - V_{CE}$ locus at which second breakdown occurs and pre-

---

[#] Work conducted at Hi-Rel Laboratories under NBS Order No. 513840.

[×] Work conducted at the Naval Research Laboratory under NBS Order No. 501718. NBS contact for additional technical information: K. F. Galloway.

[+] Work at NBS funded through the NBS Electronic Technology Program; Westinghouse portion funded by Westinghouse.

dicts a cross-over point of the hot-spot and second-breakdown loci, which was observed experimentally [114], and provides a basis for explaining the experimentally observed thermal hysteresis of the transistor current gain [115].

The model is based upon the concept of a stability factor [116] which accounts for the thermal-electrical feedback mechanisms of transistors. The expression for the stability factor which determines initiation of thermal instability is derived assuming that the current distribution throughout the device is uniform prior to instability and that I_C is related to the emitter-base voltage, V_{BE}, by the Ebers-Moll equation [117]. Once instability has occurred, the model accounts for two phenomena which occur as the current constricts to the hot-spot area. First, the current density becomes large enough that current crowding (to the edges of the emitter fingers) occurs within the hot spot, and second, base widening occurs due to the large current densities involved. The effect of these two phenomena is to modify the expression relating I_C to V_{BE} and thus also to modify the expression for the stability factor. The net result is that the device can restabilize in a stable hot-spot mode of operation and exhibit thermal hysteresis.

The three device parameters required to predict the onset of thermal instability are all easily measured. The thermal resistance, $R_{\theta JC}$, is determined using the recommended standard [118]. The emitter resistance, R_E, is determined using the floating-collector technique [119]. A pre-exponential current, I_1, which relates the collector current to the base emitter voltage, V_{BE}, at low values of collector current:

$$I_C = I_1 \exp [q(V_{BE} - E_g)/kT], \qquad (25)$$

where E_g is the forbidden energy gap (in electron volts), q is the electronic charge, k is the Boltzmann's constant, and T is the absolute temperature, is determined from curve-tracer measurements of the I_C - V_{BE} characteristic at collector currents below 10 mA.

The quantitative predictions of device behavior in the stable hot-spot mode and the onset of second breakdown are not as accurate as those for the initiation of thermal instability primarily because additional simplifying assumptions for current crowding and base widening are contained in the model. However, while this portion of the model may require some refinements to give a more exact description of device parameters and characteristics in the stable hot spot, it does appear to provide a satisfactory picture of the physical behavior of the device for these conditions.

The newly automated infrared microradiometer proved to be extremely valuable in this study. In this automated facility, an interactive data acquisition system controls the stepper-motor-driven X-Y stage upon which the device under test rests, acquires the output of the microradiometer through a digital voltmeter, and sends the results to a printer to be printed out in hard copy and paper tape. The thermal measurements were used to demonstrate the surprising fact that current crowding occurs within the hot spot. This was accomplished by noting that the temperatures along the emitter finger edges were higher than at their centers which can only be accounted for by current densities being higher at the edges than at the centers.

The results of this work are important for understanding device operation and in the design of devices where trade-offs between various device performance characteristics must always be made. However, the primary purpose for undertaking this work was to establish an improved basis for developing safe operating area limits for power transistors. These limits define the operating conditions in which overheating and thermal instabilities do not occur. (D. L. Blackburn, F. F. Oettinger, S. Rubin, G. J. Rogers, and P. L. Hower**)

** Westinghouse Research Laboratories, Pittsburgh, PA 15235.

10. REFERENCES

1. Standard Method for Test for Sheet Resistance of Silicon Epitaxial Layers Using a Collinear Four-Probe Array, ASTM Designation F 374, *Annual Book of ASTM Standards*, Part 43 (November 1976). (Available as a separate reprint from American Society for Testing and Materials, 1916 Race Street, Philadelphia, PA 19103.)

2. Standard Method for Measuring Resistivity of Silicon Slices with a Collinear Four-Probe Array, ASTM Designation F 84, *Annual Book of ASTM Standards*, Part 43 (November 1976). (Available as a separate reprint from American Society for Testing and Materials, 1916 Race Street, Philadelphia, PA 19103.)

3. Ehrstein, J. R., Improved Surface Preparation for Spreading Resistance Measurements on *p*-type Silicon, *Semiconductor Measurement Technology*: Spreading Resistance Symposium, J. R. Ehrstein, Ed., NBS Special Publication 400-10, pp. 249-255 (December 1974).

4. La Chapelle, R., Composition for Polish-Crystalline Silicon and Germanium and Process, U.S. Patent 3,429,080, February 25, 1969.

5. Walsh, R. J., and Herzog, A. H., Process for Polishing Semiconductor Material, U.S. Patent 3,170,273, February 23, 1965.

6. Mazur, R. G., and Dickey, D. H., A Spreading Resistance Technique for Resistivity Measurements of Silicon, *J. Electrochem. Soc.* 113, 255-259 (1966).

7. Ehrstein, J. R., Ed., *Semiconductor Measurement Technology*: Spreading Resistance Symposium, NBS Special Publication 400-10 (December 1974).

8. Donovan, R. P., and Evans, R. A., Incremental Sheet Resistance Technique for Determining Diffusion Profiles, *Silicon Device Processing*, C. P. Marsden, Ed., NBS Special Publication 337, pp. 123-131 (November 1970).

9. Kern, W., and Puotinen, D., Cleaning Solutions Based on Hydrogen Peroxide for Use in Silicon Semiconductor Technology, *RCA Review* 31, 187-205 (1970).

10. McCracken, F. L., Passaglia, E., Stromberg, R. R., and Steinberg, H. L., Measurement of the Thickness and Refractive Index of Very Thin Films and the Optical Properties of Surfaces, *J. Res. Natl. Bur. Stand.* 67A, 363-377 (1963).

11. Atalla, M. M., and Tannenbaum, E., Impurity Redistribution and Junction Formation in Silicon by Thermal Oxidation, *Bell System Tech. J.* 39, 933-946 (1960).

12. Wagner, S., Diffusion of Boron from Shallow Ion Implants in Silicon, *J. Electrochem. Soc.* 119, 1570-1576 (1972).

13. Tauc, J., The Theory of a Bulk Photo-Voltaic Phenomenon in Semiconductors, *Czech. J. Phys.* 5, 178-191 (1955); see also Tauc, J., *Photo and Thermoelectric Effects in Semiconductors*, pp. 98-112 (Pergamon Press, New York, 1962).

14. Blackburn, D. L., Schafft, H. A., and Swartzendruber, L. J., Nondestructive Photovoltaic Technique for the Measurement of Resistivity Gradients in Circular Semiconductor Wafers, *J. Electrochem. Soc.* 119, 1773-1778 (1972).

15. Swartzendruber, L. J., Four-Point Probe Measurement of Non-Uniformities in Semiconductor Sheet Resistivity, *Solid-State Electronics* 7, 413-422 (1964).

16. Vieweg-Gutberlet, F., and Schönhofer, F. X., Grenzen der Anavendbarkirt des 4-Spitzen-Gleichstron-Messverfahrens an Silicium-Proben, Tiel I u.II, *Archiv. techn. Messen*, No. 369, 237-240 (October 1966) and No. 370, 259-262 (November 1966).

17. SEMI Standard Specifications for Silicon Wafers. (Available from Semiconductor Equipment and Materials Institute, 625 Ellis Street, Suite 212, Mountain View, CA 94043.)

18. Standard Digital Interface for Programmable Instruments, IEEE Standard 488-1975.

19. Irvin, J. C., Resistivity of Bulk Silicon and of Diffused Layers in Silicon, *Bell System Tech. J.* 41, 387-410 (1962).

20. Buehler, M. G., *Semiconductor Measurement Technology*: Microelectronic Test Pattern NBS-3 for Evaluating the Resistivity-Dopant Density Relationship of

Silicon, NBS Special Publication 400-22 (June 1976).

21. Buehler, M. G., and Thurber, W. R., A Planar Four-Probe Test Structure for Measuring Bulk Resistivity, *IEEE Trans. Electron Devices* ED-23, 968-974 (1976).

22. Caughey, D. M., and Thomas, R. E., Carrier Mobilities in Silicon Empirically Related to Doping and Field, *Proc. IEEE* 55, 2192-2193 (1967).

23. Li, S. S., and Thurber, W. R., The Dopant Density and Temperature Dependence of Electron Mobility and Resistivity in *n*-Type Silicon (to be published).

24. Li, S. S., The Dopant Density and Temperature Dependence of Electron Mobility and Resistivity in *n*-Type Silicon, NBS Special Publication 400-33 (to appear).

25. Norton, P., Braggins, T., and Levinstein, H., Impurity and Lattice Scattering Parameters as Determined from Hall and Mobility Analysis in *n*-type Silicon, *Phys. Rev.* B8, 5632-5653 (1973).

26. Long, D., Ionized Impurity Scattering Mobility of Electrons in Silicon, *Phys. Rev.* 129, 2464-2468 (1963).

27. Debye, P. P., and Conwell, E. M., Electrical Properties of *n*-Type Germanium, *Phys. Rev.* 93, 693-706 (1954).

28. Sclar, N., Neutral Impurity Scattering in Semiconductors, *Phys. Rev.* 104, 1559-1568 (1956).

29. Mousty, F., Ostoja, P., and Passari, L., Relationship Between Resistivity and Phosphorus Concentration in Silicon, *J. Appl. Phys.* 45, 4576-4580 (1974).

30. Baccarani, G., and Ostoja, P., Electron Mobility Empirically Related to the Phosphorus Concentration in Silicon, *Solid-State Electronics* 18, 579-580 (1975).

31. Luong, M., and Shaw, A. W., Quantum Transport Theory of Impurity-Scattering-Limited Mobility in *N*-Type Semiconductors Including Electron-Electron Scattering, *Phys. Rev.* B4, 2436-2441 (1971).

32. Blatt, F. J., Theory of Mobility of Electrons in Solids, *Solid State Physics*, F. Seitz and D. Turnbull, Eds., Vol. 4., p. 356 (Academic Press, Inc., New York, 1957).

33. See ref. 37, p. 12.

34. Buehler, M. G., Impurity Centers in *p-n* Junctions Determined from Shifts in the Thermally Stimulated Current and Capacitance Response with Heating Rate, *Solid-State Electronics* 15, 69-79 (1972).

35. Sah, C. T., Chan, W. W., Fu, H. S., and Walker, J. W., Thermally Stimulated Capacitance (TSCAP) in *p-n* Junctions, *Appl. Phys. Letters* 20, 193-195 (1972).

36. Buehler, M. G., Thermally Stimulated Measurements: The Characterization of Defects in Silicon *p-n* Junctions, *Semiconductor Silicon/1973*, H. R. Huff and R. R. Burgess, Eds., pp. 549-560 (Electrochemical Society, Princeton, N.J., 1973).

37. Buehler, M. G., *Semiconductor Measurement Technology*: Defects in *PN* Junctions and MOS Capacitors Observed Using Thermally Stimulated Current and Capacitance Measurements - Videotape Script, NBS Special Publication 400-26 (April 1976).

38. Buehler, M. G., and Phillips, W. E., A Study of the Gold Acceptor in a Silicon p^+n Junction and an *n*-Type MOS Capacitor by Thermally Stimulated Current and Capacitance Measurements, *Solid-State Electronics* 19, 777-788 (1976).

39. Grove, A. S., Deal, B. E., Snow, E. H., and Sah, C. T., Investigation of Thermally Oxidized Silicon Surfaces Using Metal-Oxide-Semiconductor Structures, *Solid-State Electronics* 8, 145-163 (1965).

40. Mayo, S., Galloway, K. F., and Leedy, T. F., Radiation Dose Due to Electron-Gun Metallization Systems, *IEEE Trans. Nucl. Sci.* NS-23, 1875-1880 (1976).

41. Yau, L. D., Chan, W. W., and Sah, C. T., Thermal Emission Rates and Activation Energies of Electrons and Holes at Cobalt Centers in Silicon, *Phys. Status Solidi* A14, 655-662 (1972).

42. Sah, C. T., Forbes, L., Rosier, L. L., Tasch, A. F., Jr., and Tole, A. B., Thermal Emission Rates of Carriers at Gold Centers in Silicon, *Appl. Phys. Letters* 15, 145-148 (1969).

43. Lisiak, K. P., and Milnes, A. G., Rhodium and Iridium as Deep Impurities in Silicon, *Solid-State Electronics* 19, 115-119 (1976).

44. Miller, M. D., Schade, H., and Nuese, C. J., Use of Platinum for Lifetime Control in Power Devices, *Technical Digest*, 1975 International Electron Devices Meeting, Washington, D.C., December 1-3, 1975, pp. 180-183.

45. Yau, L. D., Smiley, C. F., and Sah, C. T., Thermal Emission Rates and Activation Energies of Electrons and Holes at Silver Centers in Silicon, *Phys. Status Solidi* A13, 457-464 (1972).

46. Rosier, L. L., and Sah, C. T., Thermal Emission and Capture of Electrons at Sulfur Centers in Silicon, *Solid-State Electronics* 14, 41-54 (1971).

47. Miyata, K., and Sah, C. T., Thermal Emission Rates and Activation Energies of Electrons at Tantalum Centers in Silicon, *Solid-State Electronics* 19, 611-613 (1976).

48. Herman, J. M., III, and Sah, C. T., Thermal Ionization Rates and Energies of Holes at the Double Acceptor Zinc Centers in Silicon, *Phys. Status Solidi* A14, 405-415 (1972).

49. Walker, J. W., and Sah, C. T., Properties of 1.0 MeV-Electron-Irradiated Defect Centers in Silicon, *Phys. Rev.* B7, 4587-4605 (1973).

50. Buehler, M. G., Investigation of Radiation-Induced Defects in Silicon *P-N* Junctions, AFCRL-72-0578 (September 1, 1972).

51. Yau, L. D., and Sah, C. T., Quenched-In Centers in Silicon p^+n Junctions, *Solid-State Electronics* 17, 193-201 (1974).

52. Fowler, R. H., *Statistical Mechanics*, 2nd ed., p. 703 (Cambridge University Press, Cambridge, 1936).

53. Goodman, A. M., *Semiconductor Measurement Technology*: The Safe Operation of Capacitance Meters Using High Applied Bias Voltage, NBS Special Publication 400-34 (December 1976).

54. Duffy, M. T., Zanzucchi, P. J., and Cullen, G. W., Method to Determine the Quality of Sapphire, Report No. 2, NBS-GCR-76-61 (September 1975). (Available from the National Technical Information Service, Springfield, VA 22161).

55. Bennett, H. E., and Porteus, J. O., Relation Between Surface Roughness and Specular Reflection at Normal Incidence, *J. Opt. Soc. Am.* 51, 123-129 (1961).

56. Davies, H., The Reflection of Electromagnetic Waves from a Rough Surface, *Proc. IEEE* 101, 209-214 (1954).

57. Johannessen, J. S., Spicer, W. E., and Strausser, Y. E., An Auger Analysis of the SiO_2-Si Interface, *J. Appl. Phys.* 47, 3028-3037 (1976).

58. Coburn, J. W., and Kay, E., Techniques for Elemental Composition Profiling in Thin Films, *Crit. Rev. Solid State Sci.* 4, 561-590 (1974).

59. Ahn, J., Perleberg, C. R., Wilcox, D. L., Coburn, J. W., and Winters, H. F., Electron-Beam Effects in Depth Profiling Measurements with Auger Electron Spectroscopy, *J. Appl. Phys.* 46, 4581-4583 (1975).

60. Standard Method of Test for Thickness of Epitaxial or Diffused Layers in Silicon by the Angle Lapping and Staining Technique, ASTM Designation F 110, *Annual Book of ASTM Standards*, Part 43 (November 1976). (Available as a separate reprint from American Society for Testing and Materials, 1916 Race Street, Philadelphia, PA 19103.)

61. Taylor, N. J., Johannessen, J. S., and Spicer, W. E., Crater-Edge Profiling in Interface Analysis Employing Ion-Beam Etching and AES, *Appl. Phys. Letters* 29, 497-499 (1976).

62. Mayo, S., Keller, R. A., Travis, J. C., and Green, R. B., Detection of Sodium Trace Contamination in Furnace Atmospheres at 1000°C, *J. Appl. Phys.* 47, 4012-4016 (1976).

63. Hetherington, G., Stephenson, G. W., and Winterburn, J. A., Vitreous Silica in Electronics, *Electrical Engineering* 41, No. 495, 52-56 (May 1969) and 41, No. 496, 44-47 (June 1969).

64. Mayo, S., and Evans, W. H., Development of Sodium Contamination in Semiconductor

Oxidation Atmospheres at 1000°C, (to be published).

65. Hughes, H. L., A Survey of Radiation-Induced Perturbations in Metal-Insulator-Semiconductor Structures, *9th Annual Proceedings, Reliability Physics 1971*, Las Vegas, Nevada, March 31-April 2, 1971, pp. 33-39.

66. Lindmayer, J., Radiation and Oxide-Metal Interactions in MOS, *IEEE Trans. Nucl. Sci.* NS-18, No. 6, 91-98 (1971).

67. Phillips, D. H., Radiation Hardening of MOS Integrated Circuits on <111> Silicon, *IEEE Trans. Nucl. Sci.* NS-22, 2190-2192 (1975).

68. Kjar, R. A., and Nichols, D. K., Radiation Induced Surface States in MOS Devices, *IEEE Trans. Nucl. Sci.* NS-22, 2193-2196 (1975).

69. Aubuchon, K. G., Harari, E., and Chang, P., CMOS Radiation Hardening, Annual Report, Contract No. N00014-72-C-0424 (Hughes Research Laboratories, Malibu, California, October, 1974).

70. Kern, W., and Comizzoli, R. B., *Semiconductor Measurement Technology*: Development of Techniques for Measuring the Integrity of Passivation Overcoats on Integrated Circuits, NBS Special Publication 400-31 (to appear).

71. Data Sheet, "Industrial Carbon Blacks," Columbian Division, Cities Service Co., 3200 W. Market Street, Akron, OH 44313, October 1975.

72. Data Sheet, "Lubrizol 894," Lubrizol Corp., Cleveland, OH 44117, November 1974.

73. Data Sheet, "A-C Polyethylene," Allied Chemical Co., Specialty Chemicals Div., P.O. Box 1087R, Morristown, NJ 07960, January 1975.

74. Kern, W., Detection and Characterization of Localized Defects in Dielectric Films, *RCA Review* 34, 655-690 (1973); see also *Solid State Technology* 17, No. 3, 35-42 (1974) and No. 4, 78-84 (1974).

75. Yager, T. A., Tressler, R. E., and Stach, J., Impurity Transfer Considerations for the Use of BN Sources for Doping Silicon, *Extended Abstracts* for the Fall Meeting of the Electrochemical Society, Las Vegas, Nevada, October 17-22, 1976, pp. 853-855.

76. Eriksson, G., Thermodynamic Studies of High Temperature Equilibria. III. SOLGAS, a Computer Program for Calculating the Composition and Heat Condition of an Equilibrium Mixture, *Acta Chem. Scan.* 25, 2651-2658 (1971).

77. Grubbs, W. H., Das, M. B., Stach, J., and Tressler, R. E., A Comparison of HCl and Trichloroethylene (TCE) Grown Oxides on Silicon, *Extended Abstracts* for the Fall Meeting of the Electrochemical Society, Las Vegas, Nevada, October 17-22, 1976, pp. 836-838.

78. Sywt, D. A., NBS Program in Photomask Linewidth Measurements, *Solid State Technology* 19, No. 4, 51-57 (April 1976).

79. Swing, R. E., The Theoretical Basis of a New Optical Method for the Accurate Measurement of Small Line-Widths, *Proc. Soc. Photo-Optical Instrum. Engrs.* 80, *Developments in Semiconductor Microlithography*, 65-77 (1976).

80. Born, M., and Wolf, E., *Principles of Optics*, 5th edition, p. 522 (Pergamon Press, New York, 1965).

81. Swing, R. E., Conditions for Microdensitometer Linearity, *J. Opt. Soc. Am.* 62, 199-207 (1972).

82. Cook, H. D., and Marzetta, L. A., An Automatic Fringe Counting Interferometer for use in the Calculation of Line Scales, *J. Res. Natl. Bur. Stand.* 65C, 129-139 (1961).

83. Mandel, John, Repeatability and Reproducibility, *Materials Research and Standards* 11, No. 8, 8-15, 52 (August 1971).

84. Kasdan, H. L., Electro-Optical Method for Measuring Gaps and Lines, U.S. Patent 3,937,580, February 10, 1976.

85. Kasdan, H. L., and George, N., Linewidth Measurement by Diffraction Pattern Analysis, *Proc. Soc. Photo-Optical Instrum. Engrs.* 80, *Developments in Semiconductor Microlithography*, 54-63 (1976).

86. Melen, R., The tradeoffs in monolithic image sensors: MOS vs. CCD, *Electronics* 46, No. 11, 106-111 (May 24, 1973).

87. Tull, R. G., Choisser, J. P., and Snow, E. H., Self-Scanned Digicon: A Digital Image Tube for Astronomical Spectroscopy, *Applied Optics* 14, 1182-1189 (1975).

88. Rodgers, R. L., III, 512×320 Element Silicon Imaging Device, *Proc. Internat. Solid State Circuits Conference*, Philadelphia, Pennsylvania, February 13-14, 1975, pp. 188-189.

89. Bruning, J. H., Feldman, M., Kinsel, T. S., Sittig, E. K., and Townsend, R. L., An Automated IC Photomask Inspection System - AMIS, *IEEE Trans. Electron Devices* ED-22, 487-495 (1975).

90. Keywell, F., and Dorosheski, G., Measurement of the Sheet Resistivity of a Square Wafer with a Square Four-Point Probe, *Rev. Sci. Instr.* 31, 833-837 (1960).

91. van der Pauw, L. J., A Method of Measuring the Resistivity and Hall Coefficient on Lamella of Arbitrary Shape, *Phillips Research Reports* 13, 1-9 (1958).

92. Mircea, A., Semiconductor Sheet Resistivity Measurements on Square Samples, *J. Sci. Instr.* 41, 679-681 (1964).

93. Green, M. A., and Gunn, M. W., The Evaluation of Geometrical Effects in Four Point Probe Measurements, *Solid-State Electronics* 14, 1167-1177 (1971).

94. Green, M. A., and Gunn, M. W., Four Point Probe Hall Effect and Resistivity Measurements Upon Semiconductors, *Solid-State Electronics* 15, 577-585 (1972).

95. Uhlir, A., Jr., The Potentials of Infinite Systems of Sources and Numerical Solutions of Problems in Semiconductor Engineering, *Bell System Tech. J.* 34, 105-128 (1955).

96. David, J. M., and Buehler, M. G., A Numerical Analysis of Various Cross Sheet Resistor Test Structures, *Solid-State Electronics* (to appear).

97. Wick, R. F., Solution of the Field Problem for a Germanium Gyrator, *J. Appl. Phys.* 25, 741-755 (1954); see problem 3.

98. Reynolds, F. N., Lawson, R. W., and Mellor, P. J. T., Specifications for Integrated Circuits in Telecommunications Equipment, *Proc. IEEE* 62, 223-230 (1974).

99. Harman, G. G., The Use of Acoustic Emission in a Test for Beam Lead Bond Integrity, *14th Annual Proceedings, Reliability Physics 1976*, Las Vegas, Nevada, April 20-22, 1976, pp. 86-97.

100. Adams, J. R., and Bonham, H. B., Analysis and Development of a Thermocompression Bond Schedule for Beam Lead Devices, *IEEE Trans. Parts, Hybrids, and Packaging* PHP-8, No. 3, 22-26 (1972).

101. Harman, G. G., Ed., *Semiconductor Measurement Technology*: Microelectronic Ultrasonic Bonding, NBS Special Publication 400-2, p. 6 (January 1974).

102. Neff, G. R., Martin, B. D., and Ruthberg, S., The Precision of the Radioisotope Method for Leak Testing Integrated Circuits (to be published).

103. Screening for Particulate Contamination in Cavity Devices, a meeting at Aerospace Corporation, Los Angeles, California, August, 1975 (unpublished).

104. Raman, C. V., On Some Applications of Hertz's Theory of Impact, *Phys. Rev.* 15, 277-284 (1920).

105. Sawyer, D. E., and Berning, D. W., *Semiconductor Measurement Technology*: A Laser Scanner for Semiconductor Devices, NBS Special Publication 400-24 (to appear).

106. Lemons, R. A., and Quate, C. F., Acoustic Microscope - Scanning Version, *Appl. Phys. Letters* 24, 163-165 (1974).

107. Lemons, R. A., and Quate, C. F., Integrated Circuits as Viewed with an Acoustic Microscope, *Appl. Phys. Letters* 25, 251-253 (1974).

108. Weglein, R. D., Acoustic Properties of Sputtered Glass at Microwave Frequencies, *Appl. Phys. Letters* 29, 277-279 (1976).

109. Keery, W. J., Leedy, K. O., and Galloway, K. F., Electron Beam Effects on Microelectronic Devices, *Scanning Electron Microscopy/1976*, O. Johari and I. Corvin, Eds., pp. 507-514 (IIT Research Institute, Chicago, Illinois, 1976).

110. Galloway, K. F., Leedy, K. O., and Keery, W. J., Electron-Beam-Induced Currents in Simple Device Structures, *IEEE Trans. Parts, Hybrids, and Packaging* PHP-12, 231-236 (1976).

111. Schwuttke, G. H., Study of Copper Precipitation Behavior in Silicon Crystals, *J. Electrochem. Soc.* 108, 163-167 (1961).

112. Thornton, P. R., Hughes, K. A., Kyaw, H., Millward, C., and Sulway, D. V., Failure Analysis of Microcircuitry by Scanning Electron Microscope, *Microelectronics and Reliability* 6, 9-16 (1967).

113. Sirtl, E., and Adler, A., Chromic Acid-Hydrofluoric Acid as Specific Reagents for the Development of Etch Pits in Silicon, *Z Metallkunde* 52, 529-531 (1961).

114. Hower, P. L., Blackburn, D. L., Oettinger, F. F., and Rubin, S., Stable Hot Spots and Second Breakdown in Power Transistors, *PESC '76 Record*, IEEE Power Electronics Specialists Conference 1976, Cleveland, Ohio, June 8-10, 1976, pp. 234-246.

115. Oettinger, F. F., and Rubin, S., The Use of Current Gain as an Indicator for the Formation of Hot Spots Due to Current Crowding in Power Transistors, *Tenth Annual Proceedings, Reliability Physics, 1972*, Las Vegas, Nevada, pp. 12-18.

116. Hower, P. L., and Govil, P. K., Comparison of One- and Two-Dimensional Models of Transistor Thermal Instability, *IEEE Trans. Electron Devices* ED-21, 617-623 (1974).

117. Gray, P. E., DeWitt, D., Boothroyd, A. R., and Gibbon, J. F., *Physical Electronics and Circuit Models of Transistors*, p. 181 (John Wiley and Sons, New York, 1964).

118. Thermal Resistance Measurements of Conduction Cooled Power Transistors, EIA Recommended Standard RS-313-B (Revision of RS-313-A), October 1975. (Available from Electronics Industries Association, 2001 Eye Street, N.W., Washington, DC 20006.)

119. Giacoletto, L. J., Measurement of Emitter and Collector Series Resistance, *IEEE Trans. Electron Devices* ED-19, 692-693; 1224 (1972).

APPENDIX A

SEMICONDUCTOR TECHNOLOGY PROGRAM STAFF

Electronic Technology Division

(301) 921-3357

J. C. French, Chief
Miss B. S. Hope*
J. F. Mayo-Wells#

Dr. W. M. Bullis, Asst. Chief for Semiconductor Technology×
Mrs. M. L. Stream*×
Mrs. E. J. Walters*†×

F. F. Oettinger, Acting Asst. Chief for Operations¶
R. L. Raybold
Mrs. T. J. Talbott
Mrs. E. Y. Trager*×

Semiconductor Characterization Section

(301) 921-3625

F. H. Brewer
Dr. W. M. Bullis, Chief×
Miss F. C. Butler*
Mrs. C. A. Cannon
Mrs. E. C. Cohen†
Dr. J. R. Ehrstein
Dr. K. F. Galloway
Mrs. A. D. Glover*
W. J. Keery
Mrs. K. O. Leedy
Dr. A. G. Lieberman
Dr. S. Mayo
Miss D. R. Ricks
R. I. Scace
H. A. Schafft
E. C. Watts†
L. R. Williams

Semiconductor Processing Section

(301) 921-3541

Dr. M. G. Buehler, Chief
J. M. David
M. R. Doggett
S. D. Grant§
Miss D. L. Hines*
Dr. R. Y. Koyama
J. Krawczyk
T. F. Leedy
Dr. S. S. Li
Y. M. Liu
R. L. Mattis
D. A. Maxwell
Dr. W. E. Phillips
L. A. Robinson
Dr. D. E. Sawyer
L. M. Smith
W. R. Thurber

Electron Devices Section

(301) 921-3621

Dr. J. H. Albers
D. W. Berning
D. L. Blackburn
G. W. Burdette†
W. A. Cullins
Mrs. K. E. Dodson*
H. E. Dyson
G. G. Harman
H. K. Kessler
Dr. D. B. Novotny
F. F. Oettinger, Chief
Mrs. B. A. Oravec*†
G. J. Rogers
S. Rubin
S. Ruthberg

---

* Secretary
† Part Time
§ Summer
¶ Telephone: (301) 921-3621
# Telephone: (301) 921-3821
× Telephone: (301) 921-3786

APPENDIX B

SEMICONDUCTOR TECHNOLOGY PROGRAM PUBLICATIONS

B.1. Prior Reports

A review of the early work leading to this Program is given in Bullis, W. M., Measurement Methods for the Semiconductor Device Industry — A Review of NBS Activity, NBS Tech. Note 511 (December 1969).

Progress reports covering the period July 1, 1968, through June 30, 1973, were published as NBS Technical Notes with the title, Methods of Measurement for Semiconductor Materials, Process Control, and Devices:

Quarter Ending	NBS Tech. Note	Date Issued	NTIS Accession No.
September 30, 1968	472	December 1968	AD 681330
December 31, 1968	475	February 1969	AD 683808
March 31, 1969	488	July 1969	AD 692232
June 30, 1969	495	September 1969	AD 695820
September 30, 1969	520	March 1970	AD 702833
December 31, 1969	527	May 1970	AD 710906
March 31, 1970	555	September 1970	AD 718534
June 30, 1970	560	November 1970	AD 719976
September 30, 1970	571	April 1971	AD 723671
December 31, 1970	592	August 1971	AD 728611
March 31, 1971	598	October 1971	AD 732553
June 30, 1971	702	November 1971	AD 734427
September 30, 1971	717	April 1972	AD 740674
December 31, 1971	727	June 1972	AD 744946
March 31, 1972	733	September 1972	AD 748640
June 30, 1972	743	December 1972	AD 753642
September 30, 1972	754	March 1973	AD 757244
December 31, 1972	773	May 1973	COM 73-50534
March 31, 1973	788	August 1973	AD 766918
June 30, 1973	806	November 1973	AD 771018

After July 1, 1973, progress reports were issued in the NBS Special Publication 400 subseries with the title, Semiconductor Measurement Technology:

Quarter Ending	NBS Spec. Publ.	Date Issued	NTIS Accession No.
September 30, 1973	400-1	March 1974	AD 775919
December 31, 1973 March 31, 1974	400-4	November 1974	COM 74-51222
June 30, 1974	400-8	February 1975	AD/A 005669
September 30, 1974	400-12	May 1975	AD/A 011121
December 31, 1974	400-17	November 1975	AD/A 017523
March 31, 1975 June 30, 1975	400-19	April 1976	PB 251844
September 30, 1975 December 31, 1975	400-25	October 1976	PB 258555

B.2. Current Publications

As various phases of the work are completed, publications are prepared to summarize the results or to describe the work in greater detail. Publications of this kind which have been issued recently are listed below:

Schafft, H. A., Ed., *Semiconductor Measurement Technology*: ARPA/NBS Workshop III. Test Patterns for Integrated Circuits, NBS Spec. Publ. 400-15 (January 1976).

Albers, J. H., Ed., *Semiconductor Measurement Technology*: The Destructive Bond Pull Test, NBS Spec. Publ. 400-18 (February 1976).

Sawyer, D. E., and Berning, D. W., *Semiconductor Measurement Technology*: Laser Scanning of Active Semiconductor Devices - Videotape Script, NBS Spec. Publ. 400-27 (February 1976).

Sawyer, D. E., and Berning, D. W., Laser Scanning of MOS IC's Reveals Internal Logic States Non-Destructively, *Proc. IEEE* 64, 393-394 (March 1976).

Lieberman, A. G., Introductory Concepts for Silicon Surface Analysis, *Semiconductor Measurement Technology*: ARPA/NBS Workshop IV. Surface Analysis for Silicon Devices, NBS Spec. Publ. 400-23 (March 1976) pp. 3-6.

Lieberman, A. G., *Semiconductor Measurement Technology*: ARPA/NBS Workshop IV, Surface Analysis for Silicon Devices, NBS Spec. Publ. 400-23 (March 1976).

Buehler, M. G., *Semiconductor Measurement Technology*: Defects in *PN* Junctions and MOS Capacitors Observed Using Thermally Stimulated Current and Capacitance Measurements - Videotape Script, NBS Spec. Publ. 400-26 (April 1976).

Kenney, J. M., *Semiconductor Measurement Technology*: Permanent Damage Effects of Nuclear Radiation on the X-Band Performance of Silicon Schottky-Barrier Microwave Mixer Diodes, NBS Spec. Publ. 400-7 (April 1976).

Keery, W. J., Leedy, K. O., and Galloway, K. F., Electron Beam Effects on Microelectronic Devices, *Scanning Electron Microscopy/1976*, Toronto, April 5-9, 1976, pp. 507-514.

Harman, G. G., The Use of Acoustic Emission in a Test for Beam Lead Bond Integrity, *14th Annual Proceedings, Reliability Physics 1976*, Las Vegas, Nevada, April 20-22, 1976, pp. 86-97.

Galloway, K. F., Leedy, K. O., and Keery, W. J., Electron-Beam-Induced Currents in Simple Device Structures, *Proceedings of the 26th Electronic Components Conference*, San Francisco, California, April 26-28, 1976, pp. 257-262.

Swyt, D. A., NBS Program in Photomask Linewidth Measurements, *Solid State Technology* 19, No. 4, 51-57 (April 1976).

Buehler, M. G., *Semiconductor Measurement Technology*: Microelectronic Test Pattern NBS-3 for Evaluating the Resistivity-Dopant Density Relationship of Silicon, NBS Spec. Publ. 400-22 (May 1976).

Ruthberg, S., Hermetic Test Procedures and Standards for Semiconductor Electronics, *Proc. Symposium on Nondestructive Testing Standards*, Gaithersburg, Maryland, May 19-21, 1976 (to appear).

Novotny, D. B., Photoresist Exposure — Measurement and Control, *Proc. Soc. Photo-Optical Instrum. Engrs.* 80, *Developments in Semiconductor Microlithography*, 9-13 (1976).

Swing, R. E., The Theoretical Basis of a New Optical Method for the Accurate Measurement of Small Line-Widths, *Proc. Soc. Photo-Optical Instrum. Engrs.* 80, *Developments in Semiconductor Microlithography*, 65-77 (1976).

APPENDIX B

Hower, P. L., Blackburn, D. L., Oettinger, F. F., and Rubin, S., Stable Hot Spots and Second Breakdown in Power Transistors, *PESC '76 Record, IEEE Power Electronics Conference 1976*, Cleveland, Ohio, June 8-10, 1976, pp. 234-246 (IEEE Cat. No. 76 CH 1084-3 AES).

Schafft, H. A., Ed., *Semiconductor Measurement Technology*: NBS/FDA Workshop, Reliability Technology for Cardiac Pacemakers, NBS Spec. Publ. 400-28 (June 1976).

Galloway, K. F., and Buehler, M. G., The Application of Test Structures and Test Patterns to the Development of Radiation Hardened Integrated Circuits: A Review, NBSIR 76-1093 (August 1976).

Oettinger, F. F., Blackburn, D. L., and Rubin, S., Thermal Characterization of Power Transistors, *IEEE Trans. Electron Devices* ED-23, 831-838 (1976).

Buehler, M. G., and Thurber, W. R., A Planar Four-Probe Test Structure for Measuring Bulk Resistivity, *IEEE Trans. Electron Devices* ED-23, 968-974 (1976).

Buehler, M. G., and Phillips, W. E., A Study of the Gold Acceptor in a Silicon p^+n Junction and an n-type MOS Capacitor by Thermally Stimulated Current and Capacitance Measurements, *Solid-State Electronics* 19, 777-788 (1976).

Mayo, W., Keller, R. A., Travis, J. C., and Green, R. B., Detection of Sodium Trace Contamination in Furnace Atmospheres at 1000°C, *J. Appl. Phys.* 47, 4012-4016 (1976).

Galloway, K. F., Leedy, K. O., and Keery, W. J., Electron-Beam-Induced Currents in Simple Device Structures, *IEEE Trans. Parts, Hybrids, and Packaging* PHP-12, 231-236 (1976).

Novotny, D. B., Sensitometry of Photoresists for Microelectronics, *Proc. SPSE Symposium on Sensitometry — Modern Aspects and Future Trends*, Binghampton, N. Y., September 16-17, 1976 (to appear).

Jerke, J. M., Hartman, A. W., Nyyssonen, D., Rosberry, F. W., Swing, R. E., Swyt, D. A., and Young, R. D., Accurate Linewidth Measurements at the National Bureau of Standards, *Proc. Microelectronics Seminar — Interface '76*, Monterey, California, October 4-5, 1976 (to appear).

Buehler, M. G., and Sawyer, D. E., Microelectronic Test Patterns for Use in Procuring Reliable, Custom Integrated Circuit Chips, *1976 Government Microcircuit Applications Conference Digest of Papers*, Orlando, Florida, November 9-11, 1976, pp. 62-65.

Sawyer, D. E., and Berning, D. W., Thermal Mapping of Transistors With a Laser Scanner, *Proc. IEEE* 64, 1634-1635 (1976).

Sawyer, D. E., and Berning, D. W., Mapping Nonlinearities Over the Active Regions of Semiconductor Devices, *Proc. IEEE* 64, 1635-1637 (1976).

Harman, G. G., and Albers, J. H., The Ultrasonic Welding Mechanism as Applied to Aluminum and Gold Wire-Bonding in Microelectronics, *Proc. Löten und Schweissen in der Electronik*, München, p. 113, November 25-26, 1976.

Mayo, S., Galloway, K. F., and Leedy, T. F., Radiation Dose Due to Electron-Gun Metallization Systems, *IEEE Trans. Nucl. Sci.* NS-23, 1875-1880 (1976).

Blackburn, D. L., Rubin, S., and Rogers, G. J., Measurements of Power Transistor Thermal Instabilities, Stable Hot Spots and Second Breakdown, *Technical Digest, 1976 International Electron Devices Meeting*, Washington, D.C., December 6-8, 1976, pp. 151-154.

Bullis, W. M., and Galloway, K. F., Semiconductor Electronics at the National Bureau of Standards: Programs and Opportunities, *Proc. 2nd IEEE (G-PHP)/ISHM University/Industry/Government Microelectronics Symposium*, Albuquerque, N. M., January 3-5, 1977, Paper IX-1.

APPENDIX B

B.3. Videotapes

Color videotape cassette presentations on improvements in semiconductor measurement technology are being prepared for the purpose of more effectively disseminating the results of the work to the semiconductor industry. These videotapes are available for distribution on loan without charge on request to Mrs. E. C. Cohen, Room A327, Technology Building, National Bureau of Standards, Washington, D. C. 20234. Copies of these videotapes may be made and retained by requestors. As an added feature, arrangements can be made for the authors to be available for a telephone conference call to answer questions and provide more detailed information, following a prearranged showing of either of the videotapes.

The following videotapes are available for distribution:

1.	Defects in PN Junctions and MOS Capacitors Observed Using Thermally Stimulated Current and Capacitance Measurements	M. G. Buehler	August 1974
2.	Laser Scanning of Active Semiconductor Devices	D. E. Sawyer and D. W. Berning	October 1975

B.4. Contractor Reports and Publications

Work carried on under contract to NBS is reported in both NBS publications and in the open literature as various phases are completed. Publications and reports of this kind which have appeared since the beginning of the contract efforts are listed below:

Steigerwalt, S. T., and Lagnado, I., The CCD as a Test Structure for Semiconductor Process Control, *Microelectronics J.* 7, 23-29 (1975).

Rudenberg, H. G., Automated Integrated Circuit Processing and Assembly, NBS-GCR-76-64 (April 1975).

Duffy, M. T., Zanzucchi, P. J., and Cullen, G. W., Method to Determine Quality of Sapphire, NBS-GCR-76-61 (September 1975).

Johannessen, J. S., Spicer, W. E., and Strausser, Y. E., Phase Separation in Silicon Oxides as Seen by Auger Electron Spectroscopy, *Appl. Phys. Letters* 27, 452-454 (1975).

Johannessen, J. S., Spicer, W. E., and Strausser, Y. E., Use of Auger Electron Spectroscopy to Determine the Structure of Silicon Oxide Films, *Semiconductor Measurement Technology*: ARPA/NBS Workshop IV. Surface Analysis for Silicon Devices, NBS Special Publication 400-23, pp. 119-123 (March 1976).

Strausser, Y. E., and Johannessen, J. S., An Auger Electron Spectroscopy Study of Silicon Spectra from Silicon Monoxide, Silicon Dioxide, and Silicon Nitride, *Semiconductor Measurement Technology*: ARPA/NBS Workshop IV. Surface Analysis for Silicon Devices, NBS Special Publication 400-23, pp. 125-138 (March 1976).

Kasdan, H. L., and George, N., Linewidth Measurement by Diffraction Pattern Analysis, *Proc. Soc. Photo-Optical Instrum. Engrs.* 80, *Developments in Semiconductor Microlithography*, 54-63 (1976).

Johannessen, J. S., Spicer, W. E., and Strausser, Y. E., An Auger Analysis of the SiO_2-Si Interface, *J. Appl. Phys.* 47, 3028-3037 (1976).

Weglein, R. D., Acoustic Properties of Sputtered Glass at Microwave Frequencies, *Appl. Phys. Letters* 29, 277-279 (1976).

Taylor, N. J., Johannessen, J. S., and Spicer, W. E., Crater-Edge Profiling in Interface Analysis Employing Ion-Beam Etching and AES, *Appl. Phys. Letters* 29, 497-499 (1976).

Goodman, A. M., *Semiconductor Measurement Technology*: The Safe Operation of Capacitance Meters Using High Applied Bias Voltage, NBS Special Publication 400-34 (December 1976).

Wilson, R. G., Planar and Axial Channeling of 800-keV As in <110> Si, *Appl. Phys. Letters* 29, 770-772 (1976).

B.5. Availability of Publications

In most cases reprints of articles in technical journals may be obtained on request to the author. NBS Technical Notes and Special Publications are available from the Superindendent of Documents, U.S. Government Printing Office, Washington, D. C. 20402, or the National Technical Information Service, Springfield, Virginia 22161, or both.

Current information regarding availability of all publications issued by the Program is provided in the latest edition of NBS List of Publications No. 72 which can be obtained on request to Mrs. E. C. Cohen, Room A327, Technology Building, National Bureau of Standards, Washington, D. C. 20234.

APPENDIX C

WORKSHOP AND SYMPOSIUM SCHEDULE

C.1. Proceedings or Reports of Past Events:

Symposium on Silicon Device Processing, Gaithersburg, Maryland, June 2-3, 1970. (Cosponsored by ASTM Committee F-1 and NBS). Proceedings: NBS Spec. Publ. 337 (November 1970).

ARPA/NBS Workshop I. Measurement Problems in Integrated Circuit Processing and Assembly, Palo Alto, California, September 7, 1973. Report: NBS Spec. Publ. 4C0-3 (January 1974).

ARPA/NBS Workshop II. Hermeticity Testing for Integrated Circuits, Gaithersburg, Maryland, March 29, 1974. Report: NBS Spec. Publ. 400-9 (December 1974).

Spreading Resistance Symposium, Gaithersburg, Maryland, June 13-14, 1974. (Co-sponsored by ASTM Committee F-1 and NBS). Proceedings: NBS Spec. Publ. 400-10 (December 1974).

ARPA/NBS Workshop III. Test Patterns, Scottsdale, Arizona, September 6, 1974. Report: NBS Spec. Publ. 400-15 (January 1976).

ARPA/NBS Workshop IV. Surface Analysis for Silicon Devices, Gaithersburg, Maryland, April 23-24, 1975. Proceedings: NBS Spec. Publ. 400-23 (March 1976).

NBS/FDA Workshop. Reliability Technology for Cardiac Pacemakers, Gaithersburg, Maryland, July 28-29, 1975. Report: NBS Spec. Publ. 400-28 (June 1976).

Reliability Technology for Cardiac Pacemakers, II, Gaithersburg, Maryland, July 19-20, 1976. Report: in preparation.

APPENDIX D

STANDARDS COMMITTEE ACTIVITIES

ASTM Committee F-1 on Electronics

J. H. Albers, Microelectronic Materials and Packaging Subcommittee

M. G. Buehler, Semiconductor Physical Properties, Semiconductor Process Materials, Electrical and Optical Measurements, Microelectronic Materials and Packaging, Microelectronics Imaging, and Quality and Hardness Assurance Subcommittees

*W. M. Bullis, Secretary; Editor, Semiconductor Physical Properties Subcommittee

J. R. Ehrstein, Semiconductor Physical Properties, Electrical and Optical Measurements, and Quality and Hardness Assurance Subcommittees

*J. C. French, Chairman, Editorial Subcommittee

G. G. Harman, Microelectronic Materials and Packaging Subcommittee

K. O. Leedy, Semiconductor Physical Properties, Electrical and Optical Measurements, Microelectronic Materials and Packaging, and Quality and Hardness Assurance Subcommittees

*C. P. Marsden, Honorary Chairman

R. L. Mattis, Editor, Semiconductor Measurements Subcommittee; Semiconductor Physical Properties Subcommittee

*J. F. Mayo-Wells, Secretary, Editorial Subcommittee

D. B. Novotny, Editor, Microelectronics Imaging Subcommittee; Semiconductor Physical Properties and Microelectronic Materials and Packaging Subcommittees

W. E. Phillips, Semiconductor Physical Properties and Electrical and Optical Measurements Subcommittees

G. J. Rogers, Lasers and Quality and Hardness Assurance Subcommittees

S. Ruthberg, Microelectronic Materials and Packaging Subcommittee

*R. I. Scace, Second Vice-Chairman

*H. A. Schafft, Publicity Officer

A. H. Sher, Semiconductor Physical Properties, Semiconductor Process Materials, Electrical and Optical Measurements, Microelectronic Materials and Packaging, Microelectronics Imaging, and Quality and Hardness Assurance Subcommittees

W. R. Thurber, Semiconductor Physical Properties and Electrical and Optical Measurements Subcommittees

ASTM Committee E-10 on Radioisotopes and Radiation Effects

W. M. Bullis, Subcommittee on Radiation Effects on Electronic Materials and Devices and Pulsed Radiation Effects

J. C. French, Subcommittee on Radiation Effects on Electronic Materials and Devices and Pulsed Radiation Effects

R. I. Scace, Subcommittee on Radiation Effects on Electronic Materials and Devices and Pulsed Radiation Effects

---

*All subcommittees.

APPENDIX D

Electronic Industries Association: Solid State Products Division, Joint Electron Device Engineering Council (JEDEC)

D. L. Blackburn, Task Group JC-25-5 on Thermal Characterization on Power Transistors, and Committee JC-25 on Power Transistors

F. F. Oettinger, Chairman, Task Group JC-25-5 on Thermal Characterization on Power Transistors, Committee JC-25 on Power Transistors; Technical Advisor, Thermal Properties of Devices, Committees JC-13.1 on Government Liaison for Discrete Semiconductor Devices, and JC-22 on Rectifier Diodes and Thyristors

S. Rubin, Chairman, Council Task Group on Galvanomagnetic Devices

D. E. Sawyer, Task Group JC-24-5 on Transistor Scattering Parameter Measurement Standard, Committee JC-24 on Low Power Transistors

H. A. Schafft, Technical Advisor, Second Breakdown and Related Specifications Committee JC-25 on Power Transistors

IEC TC47, Semiconductor Devices and Integrated Circuits

S. Rubin, Technical Expert, Galvanomagnetic Devices; U.S. Specialist for Working Group 5 on Hall Devices and Magnetoresistive Devices

IEEE Electron Devices Society

J. C. French, Standards Committee

F. F. Oettinger, Standards Committee Task Force on Second Breakdown Measurement Standards

H. A. Schafft, Standards Committee Task Force on Second Breakdown Measurement Standards

IEEE Industry Applications Society

F. F. Oettinger, Vice-Chairman, Standards Subcommittee, Power Semiconductor Committee

IEEE Magnetics Group

S. Rubin, Chairman, Galvanomagnetic Standards Subcommittee

Semiconductor Equipment and Materials Institute

R. I. Scace, Standards Committee

Society of Automotive Engineers

W. M. Bullis, Planning Subcommittee of Committee H on Electronic Materials and Processes

J. C. French, Subcommittee A-2N on Radiation Hardness and Nuclear Survivability

F. F. Oettinger, Steering Committee, Electronic Systems Committee

APPENDIX E

SOLID-STATE TECHNOLOGY & FABRICATION SERVICES

Technical services in areas of competence are provided to other NBS activities and other government agencies as they are requested. Usually these are short-term, specialized services that cannot be obtained through normal commercial channels. Such services provided during this and the previous reporting period, which are listed below, indicate the kinds of technology available to the program.

E.1. Scanning Electron Microscopy (W. J. Keery)

Tips of surface profile instruments were examined for the NBS Optics and Micrometrology Section for use in an ANSI Round Robin.

Samples of fire retardant gypsum wall board, both new and fire damaged, were examined for the NBS Fire Safety Engineering Division.

E.2. Semiconductor Device Fabrication (T. F. Leedy and J. Krawczyk)

MOS capacitors were prepared for the Harry Diamond Laboratories for use in radiation hardness and charge transport studies.

Several special silicon samples for use in a metal-vacuum-metal tunneling experiment were prepared for the NBS Mechanics Division. The fabrication of these samples included thermal and chemical vapor preparation of silicon oxide layers, chemical vapor deposition of polycrystalline silicon layers, evaporation of chromium pattern using photomask techniques, evaporation of aluminum and copper films, and use of preferential plasma etching, scribing, and mounting chips onto headers.

E.3. Metal Evaporation (J. Krawczyk)

Several special emulsion reticles were prepared for the NBS Physical Chemistry Division.

E.4. Test Pattern Applications (M. G. Buehler)

Work was initiated on development of process validation wafers to assist the Navy Special Projects Office* in identification and solution of yield problems in obtaining complex beam-lead, dielectrically-isolated, Schottky-clamped TTL circuits.

Assistance was provided to the National Security Agency† in designing a test pattern to evaluate C-MOS on sapphire processes at various prospective vendors. Eighteen test structures were designed for measuring process and device parameters.

---

*SP-27 MIPR No. N00164-76-MP-04590 and N00164-6-04590. (NBS Cost Center 4251547).

†NSA MIPR No. H 98230-R3-76-8132. (NBS Cost Center 4259562).

INDEX*

acoustic emission 69-72
acoustic microscopy 79-83
ASTM Method F 374 7-9
Auger electron spectroscopy 31-35

beam-lead bonding 69-72
bond monitor, in-process 72-74
boron nitride diffusion sources 47

capacitance-voltage method 26,28
corona discharge method 42-47
cross-type sheet resistor 64-65

depletion approximation *3*
dopant profiles 11-13; 31-35

electron beam evaporator 26,28; 36,38-40
electron mobility 17-19
electron-beam-induced-current mode 85-88
electron-beam-induced damage 84-85

filar eyepiece 53-58
film carrier bonding 72
flame emission spectrometry 19-20
flying-spot scanner 60; 77-79
four-probe array, square 39-40
four-probe method 7-9

gross leak tests 55-56

hermeticity 74-75
hot spots 88-89
hydrogen chloride oxidation 47

image-shearing eyepiece 53-58
incremental sheet resistance 11-13
infrared microradiometer 77-79
infrared reflectance method 29-30
in-process bond monitor 72-74
ion implantation 40-42
ion microprobe mass analysis *3*
Irvin's curves 15-17

junction temperature 77-79

line-width measurement 48-50; 50-52; 53; 53-56; 57-58
line-width standards 53
loose particle detection 75-76

microdensitometer 60
microscopy, optical (theory) 48-50; 50-52
modular test patterns 65-66

NBS-3 test pattern 15-17; 17-19
neutron activation analysis 30-31

optical overlay method 59
oxidation furnace atmosphere 36-37
oxide films 18-19; 26,28

particle impact noise detection (PIND) test 75-76
passivation overcoats 42-47
photomask inspection 58-61
photomask metrology 48-58
photovoltaic method 13-15
power-device silicon 13-15; 19-24
process validation wafer 65-66

radioisotope leak test 74-75
resistivity variations 13-15

safe operating area, transistor 80-89
sapphire, silicon on 26,28; 29-30; 30-31; 65, 67-68
scanning acoustic microscopy 79-83
scanning electron microscopy 84-88
scanning low energy electron probe 88
Schottky barrier diodes 40
second breakdown 88-89
sheet resistor test structures 64-65
sodium contamination 36-37
spatial filtering techniques 48-50; 57-58; 59-60
spreading resistance 9-11, 11-13
square array collector resistor 62-64
surface preparation 9-11; 29-30
surface roughness 29-30

test patterns 61; 65-66; 65,67-68
thermally stimulated current 19-27
transistor, power 88-89
transistor-transistor logic circuit 65-66
TV-microscope method 53-58; 60-61

ultrasonic wire bonding 72-74
ultraviolet reflectance 29-30

van der Pauw sheet resistor 64-65

water vapor contamination 47
wire bonds 72-74

x-ray damage 26,28; 36,38-40

*Page numbers in italics refer to entries in the Highlights section for those topics for which detailed discussions do not appear in the main body of the report.

☆ U.S. GOVERNMENT PRINTING OFFICE : 1977--240-848/69

NBS-114A (REV. 7-73)

(14) NBS-Special Pub-400-29

U.S. DEPT. OF COMM. BIBLIOGRAPHIC DATA SHEET	1. PUBLICATION OR REPORT NO. NBS Spec. Publ. 400-29	2. Gov't Accession No.	3. Recipient's Accession No.

4. TITLE AND SUBTITLE

(6) Semiconductor Measurement Technology: (9) Progress Report, 1 Jan-31 Jun 76, January 1 to June 30, 1976

5. Publication Date

(11) April 1977

6. Performing Organization Code

(12) 122.01

7. AUTHOR(S)

(10) W. Murray Bullis

8. Performing Organ. Report No.

9. PERFORMING ORGANIZATION NAME AND ADDRESS

NATIONAL BUREAU OF STANDARDS
DEPARTMENT OF COMMERCE
WASHINGTON, D.C. 20234

10. Project/Task/Work Unit No.

11. Contract/Grant No.

see item 15

12. Sponsoring Organization Name and Complete Address (Street, City, State, ZIP)

NBS - Washington, D.C. 20234; SSPO - Washington, D.C. 20376; DNA - Washington, D.C. 20305; ARPA - 1400 Wilson Boulevard, Arlington, VA 22209; SAMSO - P.O. Box 92960, Worldway Postal Center, Los Angeles, CA 90009; ERDA - Washington, D.C. 20545

13. Type of Report & Period Covered

Interim: Jan. 1 to June 30, 1976

14. Sponsoring Agency Code

15. SUPPLEMENTARY NOTES

(15) ARPA Order-2397, Program Code 6D10; DNA IACRO 76-806, SSPO Order N0016475P070030, MIPR FY76 107600366, ERDA Contract E(49-1)-3300, Mod. 3.

16. ABSTRACT *(A 200-word or less factual summary of most significant information. If document includes a significant bibliography or literature survey, mention it here.)*

This progress report describes NBS activities directed toward the development of methods of measurement for semiconductor materials, process control, and devices. Both in-house and contract efforts are included. The emphasis is on silicon device technologies. Principal accomplishments during this reporting period included (1) development of theoretical expressions for electron mobility in silicon based on combinations of scattering mechanisms; (2) successful low-temperature processing of MOS capacitors to permit measurement of thermally stimulated current and capacitance without subjecting the specimens to potentially degrading heat treatments; (3) completion of a study of the thermodynamics of reactions in an oxidation furnace tube which provides a basis for models of the effect of water vapor, chlorine, and tube wall conditions on sodium contamination levels; (4) development of a rapid, nondestructive method for reverse decoration of defects in passivation overcoats; (5) development of the theoretical basis for accurate measurement of small line widths by analysis of a spatially filtered image of the line; (6) extension of the acoustic emission technique to the nondestructive testing of tape-bonded chips and hybrid components; and (7) analysis of the results of a first exploratory interlaboratory evaluation of the radioisotope method for testing hermeticity of semiconductor devices. New tasks were undertaken to develop techniques for measuring resistivity uniformity of and non-dopant impurities and defects in power-device grade silicon and to investigate the particle impact noise detection method for screening (over)

17. KEY WORDS *(six to twelve entries; alphabetical order; capitalize only the first letter of the first key word unless a proper name; separated by semicolons)*

Acoustic emission; Auger electron spectroscopy; beam-lead bonds; capacitance-voltage methods; carrier mobility; C-MOS circuits; dopant profiles; electrical properties; electronics; four-probe method; hermeticity; ion implantation; Irvin's curves; (over)

18. AVAILABILITY	19. SECURITY CLASS (THIS REPORT)	21. NO. OF PAGES
[xx] Unlimited [ ] For Official Distribution. Do Not Release to NTIS [x] Order From Sup. of Doc., U.S. Government Printing Office Washington, D.C. 20402, SD Cat. No. C13.10:400-29 [x] Order From National Technical Information Service (NTIS) Springfield, Virginia 22151 (Microfiche only)	UNCLASSIFIED	119
	20. SECURITY CLASS (THIS PAGE) UNCLASSIFIED	22. Price $1.85

USCOMM-DC 29042-P74

COF 246 800

U.S. DEPT. OF COMM.
BIBLIOGRAPHIC DATA SHEET

16. ABSTRACT *(continued)*

devices for the presence of loose particles in the package; initial results were obtained in the study of scanning acoustic microscopy which was begun during the previous reporting period. Because of technical limitations in the methods, efforts to develop both the automated scanning low energy electron probe and in-process ultrasonic bond monitor were terminated. Also reported is other on-going work on materials characterization by electrical and physical analysis methods, materials and procedures for wafer processing, photolithography, test patterns, and device inspection and test procedures. Supplementary data concerning staff, publications, workshops and symposia, standards committee activities, and technical services are also included as appendices.

17. KEY WORDS *(continued)*

leak tests; line-width measurement; measurement methods; microelectronics; optical flying-spot scanner; oxidation particle impact noise detection test; passivation overcoats; photovoltaic method; power-device grade silicon; radioisotope method; resistivity; resistivity variations; safe operating area, transistor; scanning acoustic microscope; scanning electron microscope; scanning low energy electron probe; semiconductor devices; semiconductor materials; semiconductor process control; silicon; silicon dioxide; silicon on sapphire; sodium contamination; spreading resistance; surface roughness; test patterns; thermally stimulated current; transistors, power; TTL circuits; ultrasonic wire bonding; ultraviolet reflectance; x-ray damage.

Announcement of New Publications on Semiconductor Measurement Technology

Superintendent of Documents,
Government Printing Office,
Washington, D.C. 20402

Dear Sir:

Please add my name to the announcement list of new publications to be issued in the series: National Bureau of Standards Special Publication 400–.

Name _____

Company _____

Address _____

City _____ State _____ Zip Code _____

(Notification Key N-413)

NBS TECHNICAL PUBLICATIONS

PERIODICALS

JOURNAL OF RESEARCH reports National Bureau of Standards research and development in physics, mathematics, and chemistry. It is published in two sections, available separately:

- **Physics and Chemistry (Section A)**

Papers of interest primarily to scientists working in these fields. This section covers a broad range of physical and chemical research, with major emphasis on standards of physical measurement, fundamental constants, and properties of matter. Issued six times a year. Annual subscription: Domestic, $17.00; Foreign, $21.25.

- **Mathematical Sciences (Section B)**

Studies and compilations designed mainly for the mathematician and theoretical physicist. Topics in mathematical statistics, theory of experiment design, numerical analysis, theoretical physics and chemistry, logical design and programming of computers and computer systems. Short numerical tables. Issued quarterly. Annual subscription: Domestic, $9.00; Foreign, $11.25.

DIMENSIONS/NBS (formerly Technical News Bulletin)—This monthly magazine is published to inform scientists, engineers, businessmen, industry, teachers, students, and consumers of the latest advances in science and technology, with primary emphasis on the work at NBS. The magazine highlights and reviews such issues as energy research, fire protection, building technology, metric conversion, pollution abatement, health and safety, and consumer product performance. In addition, it reports the results of Bureau programs in measurement standards and techniques, properties of matter and materials, engineering standards and services, instrumentation, and automatic data processing.

Annual subscription: Domestic, $12.50; Foreign, $15.65.

NONPERIODICALS

Monographs—Major contributions to the technical literature on various subjects related to the Bureau's scientific and technical activities.

Handbooks—Recommended codes of engineering and industrial practice (including safety codes) developed in cooperation with interested industries, professional organizations, and regulatory bodies.

Special Publications—Include proceedings of conferences sponsored by NBS, NBS annual reports, and other special publications appropriate to this grouping such as wall charts, pocket cards, and bibliographies.

Applied Mathematics Series—Mathematical tables, manuals, and studies of special interest to physicists, engineers, chemists, biologists, mathematicians, computer programmers, and others engaged in scientific and technical work.

National Standard Reference Data Series—Provides quantitative data on the physical and chemical properties of materials, compiled from the world's literature and critically evaluated. Developed under a world-wide program coordinated by NBS. Program under authority of National Standard Data Act (Public Law 90-396).

NOTE: At present the principal publication outlet for these data is the Journal of Physical and Chemical Reference Data (JPCRD) published quarterly for NBS by the American Chemical Society (ACS) and the American Institute of Physics (AIP). Subscriptions, reprints, and supplements available from ACS, 1155 Sixteenth St. N.W., Wash. D. C. 20056.

Building Science Series—Disseminates technical information developed at the Bureau on building materials, components, systems, and whole structures. The series presents research results, test methods, and performance criteria related to the structural and environmental functions and the durability and safety characteristics of building elements and systems.

Technical Notes—Studies or reports which are complete in themselves but restrictive in their treatment of a subject. Analogous to monographs but not so comprehensive in scope or definitive in treatment of the subject area. Often serve as a vehicle for final reports of work performed at NBS under the sponsorship of other government agencies.

Voluntary Product Standards—Developed under procedures published by the Department of Commerce in Part 10, Title 15, of the Code of Federal Regulations. The purpose of the standards is to establish nationally recognized requirements for products, and to provide all concerned interests with a basis for common understanding of the characteristics of the products. NBS administers this program as a supplement to the activities of the private sector standardizing organizations.

Consumer Information Series—Practical information, based on NBS research and experience, covering areas of interest to the consumer. Easily understandable language and illustrations provide useful background knowledge for shopping in today's technological marketplace.

Order **above** *NBS publications from: Superintendent of Documents, Government Printing Office, Washington, D.C. 20402.*

Order **following** *NBS publications—NBSIR's and FIPS from the National Technical Information Services, Springfield, Va. 22161.*

Federal Information Processing Standards Publications (FIPS PUBS)—Publications in this series collectively constitute the Federal Information Processing Standards Register. Register serves as the official source of information in the Federal Government regarding standards issued by NBS pursuant to the Federal Property and Administrative Services Act of 1949 as amended, Public Law 89-306 (79 Stat. 1127), and as implemented by Executive Order 11717 (38 FR 12315, dated May 11, 1973) and Part 6 of Title 15 CFR (Code of Federal Regulations).

NBS Interagency Reports (NBSIR)—A special series of interim or final reports on work performed by NBS for outside sponsors (both government and non-government). In general, initial distribution is handled by the sponsor; public distribution is by the National Technical Information Services (Springfield, Va. 22161) in paper copy or microfiche form.

BIBLIOGRAPHIC SUBSCRIPTION SERVICES

The following current-awareness and literature-survey bibliographies are issued periodically by the Bureau:

Cryogenic Data Center Current Awareness Service. A literature survey issued biweekly. Annual subscription: Domestic, $20.00; Foreign, $25.00.

Liquified Natural Gas. A literature survey issued quarterly. Annual subscription: $20.00.

Superconducting Devices and Materials. A literature survey issued quarterly. Annual subscription: $20.00. Send subscription orders and remittances for the preceding bibliographic services to National Bureau of Standards, Cryogenic Data Center (275.02) Boulder, Colorado 80302.